



# Beating the Shot-Noise Limit: Collective Interaction Optical Noise Suppression in Charged Particle Beam

A dissertation submitted for the degree  
Doctor of Philosophy

by

**Ariel Nause**

Submitted to the Senate of Tel Aviv University

**Prof. Avraham Gover**

2014

This work was carried out under the supervision of

Prof. Avraham Gover

2014

ABSTRACT OF THE DISSERTATION

**Beating the Shot-Noise Limit:  
Collective Interaction Optical Noise Suppression  
in Charged Particle Beam**

by

**Ariel Nause**

The main subject of this dissertation is the control over fundamental processes of micro-dynamics and radiative emission in charged particle beams under the effect of longitudinal space-charge forces. These subjects are of basic scientific interest on their own, but also have significant relevance to the field of Free Electron Lasers (FELs). The possibility to control optical frequency current noise by longitudinal collective interaction in particle beams can be analytically understood and proved based on an extended 1D (single Langmuir mode) model. This model predicts the possibility to reduce the beam current-noise below the classical shot-noise level. To verify that this effect can be realised under realistic conditions of a laboratory beam, numerical 3D simulations in GPT (General Particles Tracer) codes were executed. These simulations include particle-to-particle Coulomb interactions, and therefore fully describes collective micro-dynamics in a 3D configuration. It was verified numerically that minimal current noise is attainable within a drift length of quarter wavelength longitudinal plasma oscillation with a finite beam width plasma reduction factor, as predicted in the analytical model.

Based on these theoretical predictions I performed experiments in accelerator labs in attempt to demonstrate experimentally for the first time current noise

suppression at optical frequency. The experimental method for measuring the current noise was based on optical radiation measurements of Optical Transition Radiation (OTR) from the electron beam. For the interpretation of the measured OTR data, a novel method OTR field calculation from an electron beam using dyadic Green function solution was developed and used. This model is accurate in all diffraction zones (near and far).

Two Experiments were carried out in the LCLS (in Stanford) and in ATF (Brookhaven national laboratory) which demonstrated for the first time a suppression of current noise below the classical shot-noise limit in the optical frequency regime. This process may be applicable for controlling micro-bunching instabilities, and for FEL coherence enhancement.

*To my Family ...*

# TABLE OF CONTENTS

<b>Abstract</b>		<b>ii</b>
<b>Table of Contents</b>		<b>v</b>
<b>List of Figures</b>		<b>vii</b>
<b>1 Introduction</b>		<b>1</b>
<b>2 1D Model of Noise Dynamics in Charged Electron Beams</b>		<b>6</b>
2.1 Cold-Beam Noise Dynamics Coupled Equations		7
2.2 Small Signal Wave Propagation on a Finite Cross Section Beam		9
2.3 Normalising the Coupled Equations		11
2.4 1-D Model Validity Conditions		12
2.4.1 Space-charge dominated beam expansion theorem		13
2.5 Noise Dynamics in Free Drift Transport		14
2.6 Dispersive Transport		17
2.6.1 $R_{56}$ estimation for the case of a symmetric chicane		20
2.6.2 Exemplary case of $R_{56}$ estimation - SPARC FEL		23
2.7 Collective-Interaction Regime		25
2.8 Drift and Subsequent Transport Through a Dispersive Section		28
2.8.1 Beam noise micro-dynamics in a dispersive section following a drift section		30
2.9 The Short Wavelength Limits of Noise Suppression		34

2.9.1	Ballistic electron phase spread condition in beam drift transport . . . . .	34
2.9.2	The short wavelength condition for noise suppression in the dispersive beam transport scheme . . . . .	35
2.9.3	Optical phase-spread neglect condition for the drift/dispersion scheme . . . . .	37
<b>3</b>	<b>3-D Numerical Simulations of Collective Microdynamics in an Electron Beam . . . . .</b>	<b>39</b>
3.1	introduction . . . . .	39
3.2	General Particle Tracer (GPT) Simulations . . . . .	40
3.2.1	Beam parameters and simulation method . . . . .	42
3.2.2	Creating a pulse: Choosing a random generator . . . . .	43
3.3	Noise Suppression Results . . . . .	45
3.4	3-D Effects and the Plasma Reduction Factor . . . . .	47
3.5	Charge Homogenisation Effect . . . . .	50
3.5.1	Parseval theorem verification . . . . .	54
3.6	Noise Suppression for the ATF Injector Parameters . . . . .	55
3.7	Noise Dynamics of Beam Drift - LCLS Simulations . . . . .	58
<b>4</b>	<b>Experimental Methods for Measuring Electron Beam Noise Based on Optical Transition Radiation (OTR) . . . . .</b>	<b>62</b>
4.1	Optical Transition Radiation: A General Solution . . . . .	63
4.1.1	Relativistic OTR emission from a metallic foil . . . . .	64
4.1.2	Integrated emitted OTR power from a metallic foil . . . . .	66

4.2	Spatial Coherence of OTR from an Electron Beam . . . . .	66
4.2.1	Far field OTR pattern from a phase correlated electron beam	66
4.2.2	Coherent external modulation and the spatial pattern of the micro-bunching coefficient . . . . .	69
4.2.3	The spatial pattern of the micro-bunching coefficient for a correlated e-beam after a collective interaction section . . .	72
4.3	Optical Transition Radiation - Exact Solution in the Near and Far Field Employing a Dyadic Green Function . . . . .	74
4.3.1	Radiative emission from a general line source . . . . .	77
4.3.2	The diffraction zones of a line source . . . . .	79
4.3.3	Longitudinal quadratic-phase "Fresnel" near zone limit . .	80
4.3.4	Longitudinal "Fraunhofer" far zone limit . . . . .	81
4.3.5	Ginzburg's formation zone . . . . .	82
4.3.6	Transition radiation model . . . . .	83
4.3.7	Exact Solution . . . . .	86
4.3.8	Far field approximation . . . . .	88
4.3.9	Fresnel Approximation . . . . .	89
4.3.10	Reactive near field regime . . . . .	90
4.4	OTR and COTR from an Electron Beam Using the Exact (Dyadic Green Function) Diffraction Formulation . . . . .	91
4.4.1	Coherently modulated beams . . . . .	94
4.4.2	GPT simulated beam . . . . .	96

## 5 Preliminary Experimental Study of Collective Noise Dynamics

<b>Control in LCLS</b> . . . . .	<b>103</b>
5.1 Constructing the Simulation Model of the LCLS Injector . . . . .	105
5.1.1 Simulation Considerations . . . . .	107
5.2 Simulation Results . . . . .	108
5.3 Experimental Measurements . . . . .	111
5.3.1 Measuring OTR in LCLS . . . . .	111
5.3.2 Indication of OTR Sub-Radiance? . . . . .	112
<b>6 First Observation of Current Noise Suppression Below the Shot-Noise Limit in Relativistic Charged Electron-Beam</b> . . . . .	<b>114</b>
6.1 The Experimental Concept . . . . .	114
6.2 Experimental Method . . . . .	115
6.3 Experiment Results . . . . .	117
6.3.1 Interpretation of the Experimental Results . . . . .	119
6.4 Computational Model Analysis for Experimental Observation of Optical Current Noise Suppression Below the Shot-Noise Limit . .	120
6.4.1 Conclusions . . . . .	123
<b>7 Appendix</b> . . . . .	<b>125</b>
7.1 Current and Velocity Noise Parameters of a Particle Beam in General and in the Case of a Random Uncorrelated Beam . . . . .	125
7.2 The Bunching Factor of an Electron Beam . . . . .	130
7.3 Numerical Computation Tools . . . . .	133
7.3.1 GPT simulations . . . . .	133

7.3.2	Matlab scripts . . . . .	138
7.3.3	1D model suppression tool . . . . .	138
	<b>References . . . . .</b>	<b>144</b>

## LIST OF FIGURES

2.1	Schematic drawing of the chicane drift and magnetic field sections.	20
2.2	The magnetic field $B_{\perp}(z)$ , the normalized transverse momentum parameter $a_{\perp}(z)$ and the transverse deflection $x_{\perp}$ for a specific example of a symmetric chicane with parameters $L = 2m$ , $L_m = 0.1m$ , $L_s = 0.8m$ and magnetic field amplitude of $B_0 = 0.1T$ . . . .	21
2.3	SPARC's small chicane. M1 is the bending dipole and the 3 other magnets are M 2,3,4 (marked in yellow arrows) . . . . .	24
2.4	The normalized transverse momentum parameter $a_{\perp}$ and the transverse deflection within the chicane, as a function of $z$ in SPARC's chicane . . . . .	24
2.5	The noise intensities (current noise - blue curve, kinetic voltage noise - red curve) in a free drift section with constant impedance in a case of a current noise dominated beam ( $N^2 = 0.1$ ). . . . .	26
2.6	Schematics of beam transport through a drift section, followed by an ideal dispersive section (chicane). . . . .	28
2.7	Normalized current-noise as a function of the dispersive section parameter $K_d$ for different plasma phase values $\phi_{pd}$ accumulated in the preceding free drift section of length $L_d$ . . . . .	32
2.8	Current noise gain, for a dispersive section, following a drift section, as a function of $K_d = R_{56}\gamma^2/L_d$ for three drift plasma phase $\phi_{pd}$ values: $\pi/2$ , $\pi/7$ , $\pi/10$ . (a) for $N^2 = 0.01$ and (b) for $N^2 = 0.1$ .	36

3.1	Comparison between two random generators - Rosenblu's and Matlab's. 200K numbers used and both compared to Poisson distribution curve (3.5) . . . . .	44
3.2	Spectral current noise from a 60K m.p. pulse created by Rosenblu's et al true random generator (a) and Matlab pseudo-random generator (b). Blue line represents the analytical Shot-noise amplitude $eI_b$ . . . . .	46
3.3	Current shot noise of $5\mu m$ . Curves obtained from 30k macro-particles GPT simulations for 5 different initial random particle distribution sets. The vertical line represents the theoretical quarter plasma oscillation length (in lab frame) $z = \pi c/2\omega_{pl}$ . . . . .	48
3.4	Spectral Current noise (blue) and kinetic voltage noise (red) of $5\mu m$ normalized by the beam impedance. The curves were obtained from a 30k macro-particles GPT simulation. The vertical line represents the theoretical quarter plasma oscillation length (in lab frame) $z = \pi c/2\omega_{pl}$ . . . . .	49
3.5	Current shot noise at different wavelengths (from 5 to $70\mu m$ ). Results obtained from a particular 30K macro-particles GPT simulation	50
3.6	Plasma reduction factor dependence on wavelength: following (3.7) (solid curve) and from the minima of the current noise curves (red dots)). Results obtained from a particular 30k macro-particles GPT simulation . . . . .	51
3.7	Three beam snap shots of the filtered beam $x - z$ plane sections at different transport distances (top to bottom): $z = 0$ , $z = \pi c/4\omega_{pl}$ , $z = \pi c/2\omega_{pl}$ . . . . .	53

3.8	Results of noise dynamics in frequency and time domains for 60K macro-particles. Results are for 5-10 $\mu m$ modulations and show similar suppression for equal distance . . . . .	56
3.9	ATF simulation results - Current noise reduction at 1-2 $\mu m$ for a Gaussian beam . . . . .	57
3.10	Spectral noise as a function of wavelength in a logarithmic scale according to the ATF beam parameters. The black line represents the classical shot-noise for comparison . . . . .	58
3.11	ATF beam envelope expansion . . . . .	59
3.12	Transverse beam sizes ( $\sigma_x, \sigma_y$ ) of the simulated beam (table 3.3) along the drift length. Three quad triplets were positioned in the arrow marked locations for keeping the beam envelope nearly uniform. . . . .	60
3.13	1-D model analytical results. Results predict maximal noise suppression at $z = 12.5[m]$ . . . . .	61
3.14	Spectral current noise for the LCLS parameters (table 3.3). Results obtained from a 250K macro-particles 3-D point-to-point space-charge interactions using GPT simulation. Noise was evaluated for the spectral range of 1 – 2 $\mu m$ . . . . .	61
4.1	Simulated image of a single electron OTR pattern . . . . .	65
4.2	Partially modulated electron beam current distribution. . . . .	70
4.3	Micro-bunching coefficient for different beams of different modulation levels: 100%, 75%, 50%, 25%, 1% and un-modulated beams using 100K macro particles. Plots show significant difference in the maximal amplitude for the different modulation rates. . . . .	71

4.4	Pattern of the absolute value squared of the bunching factor as a function of $\theta_x$ and $\theta_y$ , demonstrate reduction in the micro-bunching coefficient. . . . .	73
4.5	The schemes of backward transition radiation (BTR) and forward transition radiation (FTR) for a perfect conductor foil screen and their equivalent image charge representation . . . . .	74
4.6	Geometry of radiation diffraction from a current line source . . . . .	77
4.7	Transverse electric field amplitude of TR ( $\lambda = 1\mu m$ , $\gamma = 75$ ) at a distance of $10m$ . Different curves are for increasing integration lengths in formation length units . . . . .	87
4.8	Transverse electric field amplitude in the near field zone of TR ( $\lambda = 1\mu m$ , $\gamma = 75$ , $z = 10cm$ ). The exact solution and the Fresnel approximation, computation results overlap. The numerical integration was performed over 1 formation length. We show for comparison the field radiation pattern that would be predicted from the far zone formula (4.51). . . . .	90
4.9	Transverse electric field amplitude calculated using the exact solution, at various observation distances in the reactive near-field compared to the Coulomb field of a relativistic particle (4.1) (dots). The demonstrates the transition of the Coulomb field to radiation field. X-axis values are presented in normalised units $\rho k/\gamma$ . . . . .	91
4.10	Density modulation function in the time-domain for a perfectly modulated beam. . . . .	94

4.11	OTR emission ( $1\mu m$ wavelength), at $z=10m$ from a randomly distributed beam (a), partially modulated beam (b) and a coherently modulated beam (c). The same colour-bar scale is used in all images. A significant increase in radiation power takes place for higher coherence levels. . . . .	95
4.12	OTR emission ( $1\mu m$ wavelength), at $z=10m$ from a randomly distributed beam (red), partially modulated beam (black) and a coherently modulated beam (blue). The same colour-bar scale is used in all images. A significant increase in radiation power takes place for higher coherence levels. . . . .	95
4.13	OTR emission at $1\mu m$ wavelength, at $z=1mm$ from a randomly distributed beam (a), partially modulated beam (b) and a coherently modulated beam (c). The same colour-bar scale is used in all images. A significant increase in radiation power takes place for higher coherence levels. . . . .	96
4.14	A cross-cut of the OTR emission at $1\mu m$ wavelength, at $z=1mm$ using a randomly distributed beam (green), partially modulated beam (red) and a coherently modulated beam (blue). A significant increase in radiation power takes place for higher coherence levels. . . . .	97
4.15	Near-field OTR emission ( $z = 1mm$ ) at $1\mu m$ wavelength, from a GPT simulated beam at $L = 0$ (shot-noise) and at $L = L_{\pi/2} = 12m$ (quarter plasma wavelength oscillation). . . . .	98
4.16	A cross-cut of the near field OTR emission at $1\mu m$ wavelength, at $z = 1mm$ at two locations: $L = 0$ (shot noised beam) and at $L = L_{\pi/2} = 12m$ (quarter plasma wavelength oscillation) . . . . .	99

4.17	Far-field OTR emission ( $z = 1m$ ) at $1\mu m$ wavelength, from a GPT simulated beam at $L = 0$ (shot-noise) and at $L = L_{\pi/2} = 12m$ (quarter plasma wavelength oscillation). . . . .	101
4.18	A cross-cut of the far field OTR emission at $1\mu m$ wavelength, at $z = 10m$ at two locations: $L = 0$ (shot noised beam) and at $L = L_{\pi/2} = 12m$ (quarter plasma wavelength oscillation) . . . . .	101
4.19	Far-field OTR emission ( $z = 10m$ ) at $1\mu m$ wavelength, from a GPT simulated beam at $L = 0$ (shot-noise) and at $L = L_{\pi/2} = 12m$ (quarter plasma wavelength oscillation). . . . .	102
4.20	A cross-cut of the far field OTR emission at $1\mu m$ wavelength, at $z = 10m$ at two locations: $L = 0$ (shot noised beam) and at $L = L_{\pi/2} = 12m$ (quarter plasma wavelength oscillation) . . . . .	102
5.1	LCLS injector section. OTR screens are marked in yellow . . . . .	104
5.2	LCLS injector section . . . . .	106
5.3	LCLS beam axial current profile measurements (black), a Gaussian model (blue) and a step function (red). In our simulations we used a step function model of the axial current distribution. . . . .	107
5.4	Noise dynamics for more than a quarter plasma oscillation. Noise was estimated in bandwidth of $1-2\mu m$ . Quarter plasma oscillation distance is $12m$ . Vertical dashed black line represent the location of the dog-leg bend in LCLS machine. This simulation is a reference simulation for the real-life bend-included simulation. . . . .	109

5.5	Noise dynamics from GPT simulation of LCLS for two pulse charges - 0.25 and 0.5nC. Noise was estimated in bandwidth of 1-2μm. Vertical dashed black line represent the location of the dog-leg bend in LCLS machine. Current noise gain takes place after the bend. . . . .	110
5.6	OTR intensity calculated from GPT simulation of LCLS beam, at OTR2 - z = 3 - (red) and at location of OTR3 -z = 6m-(blue). .	111
5.7	OTR Images of screens OTR2 (a) OTR3 (b) and OTR11 (c), located between the accelerator exit, the dog-leg bend and after the bend and L1s acceleration section respectively. Results show integrated intensity reduction from 0.7 Mcts to 0.53 Mcts within the drift section, and a significant enhancement of the OTR intensity to 2 Mcts at OTR11. Beam charge was 500pC. . . . .	113

6.1	The experimental set-up. The ATF e-beam transport set-up is shown from the injector RF-LINAC exit to the OTR viewer site (CTR-1). The accelerated beam energy was varied from $50MeV$ to $70MeV$ and the beam charge was varied from $200pC$ to $500pC$ . The beam spot dimensions were measured at four locations using fluorescent screens (YAG-1 to YAG-4). The beam envelope was kept nearly uniform, except in the main section between quadrupole lenses TRIPLET-1 and TRIPLET 2 where it was focused to a narrow waist in the center of the free drift section between the triplets (the chicane in the drawing was turned off). An electronic signal proportional to the photon number of integrated OTR emission from CTR-1 was measured using a CCD camera. Independently, similar reference measurement was carried out at CTR-0 prior to the collective interaction drift region. . . . .	115
-----	---	-----

6.2	Integrated OTR intensity measurement signals divided by the electron pulse charge. The CTR-1 data corresponds to OTR measurement from a screen, intercepting the e-beam 6.5 m away from the LINAC exit. The curves negative slope indicates relative current shot-noise suppression of 20%-30% as the beam charge varies from 0.2-0.5 nC at different beam energies (50-70 MeV). The CTR-0 data corresponds to OTR measurement right after the LINAC exit. Used for reference, its horizontal slope (linear scaling of $S_{OTR}$ with beam charge) indicates that there was no charge suppression prior to the collective micro-dynamic process in the subsequent drift section. The error of the camera integrated signal measurement - 3%, was determined from the variance in the value of the signal due to pulse-to-pulse variation, measured repeatedly while keeping all beam control parameters fixed. The charge measurement error is 1%. . . . .	118
6.3	Noise suppression along the collective interaction region as calculated from solution of the coupled differential equations with $\sigma_x(z)$ , $\sigma_y(z)$ of 70 MeV. . . . .	122
6.4	Noise suppression along the collective interaction region as calculated from solution of the coupled differential equations with $\sigma_x(z)$ , $\sigma_y(z)$ of 50 MeV. . . . .	123
6.5	Relative noise suppression rate computed from Eq. 2.31 and 2.32 for E=50 MeV, 70 MeV compared to the experimental suppression results. . . . .	124

## ACKNOWLEDGMENTS

I would like to start by thanking my advisor, Professor Avraham Gover, who walked me through this Ph.D research and had a great part in my development as a physicist. Thanks for the permanent willingness, support and encouragement. I am indebted to all members of the FEL group in Tel Aviv University, and especially to Dr. Egor Dyunin who assisted and guided me throughout a substantial part of this research work. I want to thank the staff of the Accelerator test facility in BNL for their part in the experimental research work I conducted there during several visits. It was impossible to succeed without their contribution. I would like to thank my parents, Reuven and Yaffa, who encouraged (most of the time...) my decision to pursue a degree in Physics during all these years, and last, but by all means not least, I want to express my deep gratitude to my dear wife Yam for her incredible and infinite support, which allowed me to complete this work, and for giving me my first son Adam during this period.

## VITA

Oct. 2008            Ph.D Studies *Physics and Astronomy Department, Tel Aviv*  
to March 2014      *University, Tel Aviv*

Oct. 2005            M.Sc Studies *Physics and Astronomy Department, Tel Aviv*  
to Oct. 2008        *University, Tel Aviv*

Oct. 2002            B.Sc Studies *Physics Department, Ben Gurion University, Beer*  
to Oct. 2005        *Sheva*

## PUBLICATIONS

**A. Nause, E. Dyunin, A. Gover** (2014) Exact Theory of Optical Transition Radiation in the Far and Near Zones, *J. Opt. Soc. Am. B*, Vol. 31, Issue 10, pp. 2438-2445.

<http://dx.doi.org/10.1364/JOSAB.31.002438>

**A. Nause, E. Dyunin, A. Gover** (2014) "Suppressing Shot Noise In Charged Electron Beams At Short Wavelength", *Physics of Plasmas*, 21, 083114.

<http://dx.doi.org/10.1063/1.4894110>

**A. Gover, A. Nause, E. Dyunin, M. Fedurin** (2012) Beating the shot-noise limit, *Nature Physics* 1745-2481.

<http://dx.doi.org/10.1038/nphys2443>;

**A. Gover, E. Dyunin, T. Duchovni, A. Nause** (2011) Collective microdynamics and noise suppression in dispersive electron beam transport, *Phys. of Plasmas* , 18, 123102.

<http://link.aip.org/link/doi/10.1063/1.3662065>;

**E. Dyunin, A. Nause, A. Gover** (2011) Suppression of Current Shot Noise and of Spontaneous Radiation Emission in Electron Beams by Collective Coulomb Interaction, *IEEE transactions on Plasma Sciences*, 39, 10.

**I. Shafir, A. Nause, L. Nagli, A. Katzir** (2011) Mid-infrared luminescence properties of Dy-doped silver halide crystals, *Journal of Applied Optics* Vol. 50 Issue 11, pp.1625-1630.

**A. Nause, E. Dyunin, A. Gover** (2010) Optical Frequency Shot-Noise Suppression in Electron Beams - 3D Analysis, *Journal of Applied Physics* 107, 10, 103101.

<http://link.aip.org/link/?JAP/107/103101/1>;

# CHAPTER 1

## Introduction

Shot-noise is a noise resulting from the granular nature of density distribution in random flow of discrete particles. In the case of an electron beam, the discreteness of the particles and the randomness of electrons emission from the cathode causes time dependent fluctuations of the charge and current at any cross section along the beam transport line. This noise was first reported in 1918 by Schottky [1] who made experiments in vacuum tubes. Current noise is best characterised in terms of its spectral density, which is the statistical average of the windowed Fourier transform of the electric current time-varying fluctuations absolute value squared. We call the beam current noise "Shot Noise" when the beam particles flow is completely random (uncorrelated), satisfying Poisson statistics.

The current noise parameter is important mostly in connection to spontaneous emission generation of electromagnetic radiation by an electron beam in Free Electron Lasers (FELs) and any other free electron radiation scheme. This is, because the spectral density of the emitted radiation, and therefore also the optical coherence parameters of the radiation source are proportional to the spectral density and the spectral parameters of the source electron beam. If the collective interaction noise suppression process can be controlled and employed efficiently to laboratory available electron beam, it may be of significant importance for improving the coherence of several free electron radiation sources like FEL. The question is whether technological limitations of beam acceleration and transport

limit the process from taking place, and in what frequency range.

The scientific hypothesis underlying this research is that it is possible to observe and control optical frequency spectrum of current fluctuations as well as the velocity (energy) fluctuations in a dense relativistic charged particles beam. Moreover, at certain conditions, when the dominant noise in the beam is initially current shot-noise, it is possible to reduce significantly the beam current noise. This can be accomplished by virtue of a collective interaction process along an interaction length corresponding to a quarter period longitudinal plasma oscillation in the beam, or by using a combined drift and dispersion beam transport scheme where the dispersive section can be a bending magnet or a Chicane. The reduction of current noise means suppression of particle density fluctuations or homogenisation of the charge distribution in the beam. This remarkable optical scale "self ordering" process in a commonplace relativistic charged particles beam is quite unexpected, although similar effects were observed in the microwave frequency regime 60 years ago [2]. It should be stressed that this hypothesis does not violate any thermodynamics principles. When the beam density homogenises, the current shot noise transforms into energy (or velocity) noise.

In recent years, there has been great advance in the technological improvement of the quality parameters (energy spread, emittance) of accelerated high current density electron beams [3]. This progress, came about primarily with the invention and development of photo-cathode RF electron-gun injectors. Another development, significant for this research, is the technique of Optical Transition Radiation (OTR) diagnostics, which is used to record the e-beam current distribution, but indeed measures the current shot-noise density distribution that normally is assumed to be proportional to the current density distribution.

Coherent interference effects that were observed in 2008 during OTR mea-

measurements [4] on the LINAC injector of LCLS (SLAC's new X-ray FEL that started working in the beginning of 2009 [3]) drew attention to a longitudinal collective (LC) interaction micro-dynamics process of current and energy noise (micro-bunching) that takes place spontaneously in an intense electron beam [5]. Independently of this experiment, such a micro-dynamic LC interaction process was analysed by A. Gover and E. Dyunin in the frame work of a 1-D model analysis of noise suppression and gain [6],[7]. The LCLS experiments resulted observation of enhanced and partially coherent (COTR) radiation after beam transport through a dispersive magnetic element (bend). Their COTR and noise gain findings, initially reported as "unexplained physics" [4], were consistent with the theoretical collective micro-dynamics model of Gover and Dyunin for the particular parameter regime of this experiment and of similar COTR effect observations in other laboratories [8]. However, the main focus of this work is another operating regime, in which instead of noise gain (micro-bunching instability) one can obtain noise suppression. This has never been observed in any laboratory at optical frequencies, because it requires setting the beam transport in a specific way, that is determined by the LC micro-dynamics process, and was predicted by our theoretical model and simulations [7] [9]. The effect was observed by us for the first time by us in 2011 in an experiment conducted in ATF (Accelerator Test Facility) [10], and confirmed the prediction of our theoretical model.

Soon after our drift transport collective interaction suppression experiment, Ratner *et al* demonstrated in 2012 in LCLS current noise suppression in another scheme of beam transport through a drift and subsequent dispersive section [11]. This experiment confirmed their theoretical model for the effect [12] and ours [13]. This work contains analysis of both noise suppression schemes in a single unified model, including comparative analysis of their advantages and disadvantages.

Whether these collective micro-dynamic interaction processes can be employed in theory and in practical laboratory beam transport systems, and exhibit substantial current shot-noise suppression, is a question of paramount importance in the field of Free Electron Lasers (FEL). Current shot-noise is the incoherent input power signal of FEL. Control of the current noise power in the e-beam, which is injected into the FEL, would provide means to control the amplified spontaneous emission (SASE) radiation power [14]. In seed injected FEL, It would enable to diminish the noisy SASE power and attain high, temporally coherent, output. Such a coherent and bright radiation source, which is not in existence at present, is expected to have very significant importance as a spectroscopic and coherent imaging tool in many sciences, including molecular biology, chemistry and atomic and condensed matter physics [15].

Chapter 2 presents the theoretical 1D model of a single Langmuir plasma wave transverse mode in a stochastic formulation for the electron beam current and velocity noise. The analysis results in the effect of noise suppression in the two different schemes: (a) a free drift and (b) drift and dispersive section. It includes estimates for the validity conditions of this model and analytical expressions for noise suppression in the simple case of a uniform transverse size beam.

Chapter 3 shows numerical results from simulations using the General Particle Tracer (GPT) code, demonstrating current noise suppression below the classical shot-noise limit in a relativistic electron beam. These simulations demonstrate the noise suppression effect in various realistic beam parameters, with and without electron-optics (such as quadrupole magnets). Simulated beam parameters are based on parameters of real injectors of RF LINACs, which were later used for our experiments.

Chapter 4 describes the OTR (Optical Transition Radiation) effect, which

was used to measure the current noise amplitude. We show in this chapter the known method of calculating OTR from a single particle in the far-field zone, and the micro bunching coefficient method commonly used to calculate OTR from a beam. We then present a novel method for exact solution of the OTR in all diffraction zones, based on solving the dyadic Maxwell equations Green's function. This is used to calculate the complex electric field of the radiation emitted from a single electron, which allows calculations of the OTR in any desired range - far zone, near zone and reactive near zone. I use this formulation to demonstrate coherence effects in electron beam, such as coherent and partially coherent super-radiance and sub radiance from corresponding super/sub Poissonian electron beam distributions.

Chapter 5 describes a preliminary noise suppression experiment that I conducted in LCLS (Linac Coherent Light Source) in 2009 [16]. The results of this experiment indicates possible observation of noise suppression in agreement with our theoretical model prediction. The measured noise suppression factor and OTR pattern modification were not significant enough to claim observation of noise suppression effect with full confidence. However, it was encouraging enough to lead us to repeat the experiment in another accelerator facility (ATF) as described in the next chapter.

Chapter 6 describes the experiment that I conducted in the ATF. This experiment provided the first unambiguous experimental verification of current noise suppression by the LC micro-dynamics process at optical frequencies.

## CHAPTER 2

### 1D Model of Noise Dynamics in Charged Electron Beams

The 1-D model for optical frequency collective noise dynamics is based on a relativistic extension of formulation developed in the fifties in the microwave frequency regime. These were employed for study and development of low noise microwave tubes [2]. The conventional theory of charged particle beam transport is based on linear transformation of the kinetic parameters of the individual particles in electron-optical systems. The particle parameters are described in a 6 dimensions phase space [17]  $(\delta x_j, \delta x'_j, \delta y_j, \delta y'_j, c\delta\tau_j, \delta p_j/p_0)$  and the transformation of each particle  $j$ , independently of others, is characterised by a matrix  $R_{mn} : x_m^{(j)} = \sum_{n=1}^6 R_{mn} x_n^{(j)}$ . However, this formulation cannot describe collective interaction. To describe such effects, one needs to solve the 6-D kinetic plasma equations, including Poisson equation [18] or, if the beam quality parameters (emittance -  $\epsilon$ , energy spread -  $\delta\gamma_j/\gamma$ ) are small, the 3-D moment (fluid) plasma equations suffice [19]. The main idea is to employ the linear (small signal) analysis on the fluid plasma equations of a relativistic electron beam, assuming a predominantly longitudinal interaction model for the space-charge density fluctuations (micro-bunching) in the beam.

## 2.1 Cold-Beam Noise Dynamics Coupled Equations

The longitudinal current density and axial velocity are expanded to first order in terms of the small signal time dependent modulations:

$$\mathbf{J}(\mathbf{r}, t) = \mathbf{J}_0(\mathbf{r})\hat{e}_z + j_z(\mathbf{r}_\perp, z, t)\hat{e}_z \quad (2.1)$$

$$\mathbf{v}(\mathbf{r}, t) = \mathbf{v}_0(\mathbf{r})\hat{e}_z + c\beta_z(\mathbf{r}_\perp, z, t)\hat{e}_z \quad (2.2)$$

Also other parameters of the e-beam plasma ( $\rho, \gamma, E_{sc}$ ) are expanded in terms of a DC and a small-signal time dependent term and all are plugged into the linearized fluid plasma equations (relativistic force equation (2.3), continuity equation (2.4) and Poisson equation (2.5)):

$$\frac{d\mathbf{p}(\mathbf{r}, t)}{dt} = -e(\mathbf{E}_{tot}(\mathbf{r}, t) + [\mathbf{u}(\mathbf{r}, t) \times \mathbf{B}_{tot}(\mathbf{r}, t)]) \quad (2.3)$$

$$e\frac{\partial n(\mathbf{r}, t)}{\partial t} + \nabla \cdot en(\mathbf{r}, t)\mathbf{u}(\mathbf{r}, t) = 0 \quad (2.4)$$

$$\nabla \cdot \mathbf{E}_{tot}(\mathbf{r}, t) = -\frac{en(\mathbf{r}, t)}{\epsilon_0} \quad (2.5)$$

where  $\mathbf{p}$  is the momentum of an electron,  $(-e)$  is the charge,  $\mathbf{E}_{tot}$  and  $\mathbf{B}_{tot}$  are the total electric and magnetic fields respectively,  $n$  is the density of electrons in the beam,  $\mathbf{u}$  is the beam velocity,  $\epsilon_0$  is the dielectric permittivity of vacuum.

After Fourier transformation, it is found [7] that the dynamic axial interaction evolution (longitudinal plasma oscillation) process can be described in terms of only two parameters: the spectral axial current:

$$\check{I}(z, \omega) = \iint \check{J}_z(\mathbf{r}_\perp, z, \omega) d^2r_\perp \quad (2.6)$$

and the spectral beam kinetic voltage  $\check{V}(\omega)$  [20]:

$$\check{V}(z, \omega) = -\frac{mc^2}{e}\check{\gamma}(z, \omega) = -\frac{mc^2}{e}\frac{\partial\gamma_0}{\partial\beta_0}\check{\beta}(z, \omega) = -\frac{mc^2}{e}\gamma_0^3\beta_0\check{\beta}(z, \omega) \quad (2.7)$$

which can be viewed also as the beam energy modulation parameter normalized to electron-Volt units. where  $c\check{\beta}$ ,  $\check{\gamma}(\omega)$  are the spectral Fourier transformed velocity and energy modulation parameters:

$$\check{\beta}(\mathbf{r}_\perp, z, \omega) = \int_{-\infty}^{\infty} e^{i\omega t} \beta_z(\mathbf{r}_\perp, z, t) dt \quad (2.8)$$

$$\check{\gamma}(\mathbf{r}_\perp, z, \omega) = \int_{-\infty}^{\infty} e^{i\omega t} \gamma(\mathbf{r}_\perp, z, t) dt \quad (2.9)$$

Using this technique, the cold-beam plasma moment equations can be reduced into coupled equations for the spectral current and kinetic voltage modulation describing the e-beam plasma wave (Langmuir modes) evolution (as derived by Dyunin [21]):

$$\frac{d\check{J}(z, \omega)}{dz} - \frac{i\omega}{c\beta_0(z)}\check{J}(z, \omega) = -i\omega\epsilon_0\theta_{pr}^2(z)\check{V}(z, \omega) \quad (2.10)$$

$$\frac{d\check{V}(z, \omega)}{dz} - \frac{i\omega}{c\beta_0(z)}\check{V}(z, \omega) = -\frac{i}{\omega\epsilon_0}\check{J}(z, \omega) \quad (2.11)$$

Allowing slow variation of these beam transport parameters along the propagation axis  $z$ , we define slow varying small signal amplitudes of the spectral current and kinetic voltage:

$$\check{j}(z, \omega) = \check{J}(z, \omega) \exp[-i\phi_b(z)] \quad (2.12)$$

$$\check{v}(z, \omega) = \check{V}(z, \omega) \exp[-i\phi_b(z)] \quad (2.13)$$

where

$$\phi_b(z) = \omega \int_{-\infty}^z \frac{1}{c\beta_{z0}(z')} dz' \quad (2.14)$$

therefore one obtains:

$$\frac{d\check{j}(z, \omega)}{dz} = -i\omega\epsilon_0\theta_p^2(z)\check{v}(z, \omega) \quad (2.15)$$

$$\frac{d\check{v}(z, \omega)}{dz} = -\frac{i}{\omega\epsilon_0}\check{j}(z, \omega) \quad (2.16)$$

where  $\theta_p$  is the longitudinal 1-D plasma wavenumber:

$$\theta_p(z) = \frac{\omega_{p0}}{c\beta_0(z)} = \sqrt{\frac{e^2 n_0(z)}{m_e c^2 \gamma_0^3(z) \beta_0^2(z)}} \quad (2.17)$$

## 2.2 Small Signal Wave Propagation on a Finite Cross Section Beam

In order to extend this model to the case of a finite cross-section beam, we assume a constant density and velocity distributions across the beam cross section. To account for the modification of the field lines due to the fringing of the field we use the plasma correction factor notation  $r_p$  [22]:

$$\omega_{pr} = r_p \omega_p \quad (2.18)$$

For the case of a transverse uniform distribution beam propagating in free space, for the fundamental Langmuir wave plasma mode [23]:

$$r_p^2 = 1 - (kr_b/\gamma)K_1(kr_b/\gamma_0\beta_0) \quad (2.19)$$

where  $K_1(x)$  is the modified Bessel function of the second kind and  $k$  is the optical wave number ( $k = 2\pi/\lambda$ ). For the case of a Gaussian beam distribution (transverse size variance  $\sigma_x$ ) Marinelli et al derived an alternative expression [24]:

$$r_p = \frac{2k\sigma_x}{\beta_0\gamma_0 + 2k\sigma_x} \quad (2.20)$$

Note that in the limit of a wide beam:

$$2r_b \gg \beta_0\gamma_0\lambda = \lambda' \quad (2.21)$$

both formulas reduce to the 1-D plasma wave limit:  $r_p = 1$  and  $\omega_{pr} = \omega_p$ . The RHS of equation (2.21) is exactly the bunching wave length as seen in the beam frame. Considering that  $r'_b = r_b$  under Lorentz transformation, this expression is consistent with the fringing field effect being negligible in the 1D limit.

We can generalise the 1-D equation (2.15), (2.16) for the case of a finite transverse size beam by integrating the equations over the transverse coordinates, which corresponds to multiplying them by the beam cross section  $A_e = \pi r_b^2$ .

We define a small signal current modulation parameter as:

$$\check{I}(z) = \int \check{J}(x, y, z) dx dy = A_e \check{J}(0, 0, z) \quad (2.22)$$

and using Gauss law for the finite cross-section beam case with reduced axial fields due to fringing:

$$\check{E}(z) = -\frac{i r_p^2}{\omega \epsilon_0 A_e} \check{I} \quad (2.23)$$

we can write equations (2.15) and (2.16) for the finite cross-section beam case [21]:

$$\frac{d\check{i}(z, \omega)}{dz} = -i\omega\epsilon_0 A_e \theta_{pr}^2(z) \check{v}(z, \omega) \quad (2.24)$$

$$\frac{d\check{v}(z, \omega)}{dz} = -\frac{ir_p^2}{\omega\epsilon_0 A_e} \check{i}(z, \omega) \quad (2.25)$$

where  $\theta_{pr} = r_p \theta_p$ .

Defining

$$W(z) = \sqrt{\mu_0/\epsilon_0} r_p^2 / (k A_e \theta_{pr}(z)) \quad (2.26)$$

as the plasma-wave beam-impedance, equations (2.24) and (2.25) can be put in a compact form:

$$\frac{d}{dz} \check{i} = -i \frac{\theta_{pr}(z)}{W(z)} \check{v} \quad (2.27)$$

$$\frac{d}{dz} \check{v} = -i \theta_{pr}(z) W(z) \check{i} \quad (2.28)$$

Our definition of the plasma beam wave impedance  $W(z)$  relates to the parameter of beam impedance per unit length  $Z_{LSC}$  used in [25][26] and others, by the relation  $W = -iZ_{LSC}/\theta_{pr}$ . This is an essential parameter transformation needed to describe collective interaction where  $W = W(z)$ .

### 2.3 Normalising the Coupled Equations

When performing an analysis of experimental results or determining effects in a size-varying beam envelopes (when using electron-optics such as a quadrupole), one must use a numerical approach in order to solve the differential equations set (2.27) (2.28) with initial conditions. In this approach (which will be demonstrated in later chapters) beam diameter is changing with every step due to the quadrupoles effects, and the accumulated phase is calculated for each step and then summed. These calculations are easier done with a normalised set of equa-

tions. We define the normalised variables:

$$i_N = \frac{\check{i}}{\check{i}(0)} \quad (2.29)$$

$$v_N = \frac{\check{v}}{W_d(0)\check{i}(0)} \quad (2.30)$$

where  $W_d(0) = Z_0 r_p^2 / k A_e(0) \theta_{pr}(0)$ .

Differentiation of these equations in  $z$  will result with the normalised coupled equations describing the noise dynamics for a short path:

$$\frac{d}{dz} i_N = -i\omega\epsilon_0 A_e(z) \theta_{pr}^2(z) W_d(0) v_N(z) \quad (2.31)$$

$$\frac{d}{dz} v_N = -\frac{i r_p^2}{\omega\epsilon_0 A_e(z)} \frac{1}{W_d(0)} i_N(z) \quad (2.32)$$

For a constant beam diameter these equations results with the  $\cos \phi_p$  solution.

## 2.4 1-D Model Validity Conditions

In this section we analyse limitations to the validity of the single plasma-wave Langmuir mode fluid plasma model used in this work in the optical frequency range. These validity conditions present physical conditions which need to be satisfied in order to observe the noise suppression effect. To justify the longitudinal charge bunching model, a multitude of particles must be present per bunching wavelength  $\lambda\beta_0$ :

$$n_0 A_e \lambda \beta_0 \gg 1 \quad (2.33)$$

Another restriction to a cold beam model is, that the optical-phase spread  $\phi_b$  of the electrons along the interaction length  $L_d$  due to the beam velocity spread

should satisfy  $\Delta\phi_b = kL_d\Delta(1/\beta_z) \ll \pi$ . This corresponds to restrictions on the beam-energy spread:

$$\Delta\gamma/\gamma_0 \ll \beta_0^3\gamma_0^2\lambda/2L_d \quad (2.34)$$

and on the emittance:

$$\epsilon_n \ll \beta_0^2\gamma_0\sigma_{x0}(\lambda/L_d)^{1/2} \quad (2.35)$$

#### 2.4.1 Space-charge dominated beam expansion theorem

Noise reduction analysis requires a beam drift length  $L_d$  of  $\phi_p = \theta_{pr}L_d$  with a uniform cross section. Can such uniform drift be maintained without continuous guiding by means of focusing elements? A. Gover and E. Dyunin proved a useful theorem [7]: If the beam expansion away from the waist is space-charge dominated, quarter plasma wavelength oscillation takes place within the waist of a free-space drifting beam. The proof was based on the well known Kapchinsky-Vladimirsky (KV) beam envelope equation [27]:

$$r_b''(z) + k_0^2r_b(z) - K/r_b(z) - \bar{\epsilon}^2/r_b^3(z) = 0 \quad (2.36)$$

which is valid for a flat-top current-density distribution of a beam of radius  $r_b(z)$ ,  $k_0$  is the beam focusing parameter. The equation is approximately valid for a Gaussian distribution with  $r_b = \sqrt{2}\sigma_x$ ,  $\bar{\epsilon} = 2\epsilon$  where  $\epsilon = \epsilon_n/\beta_0\gamma_0$  is the conventional emittance definition,  $k_0$  is the external focusing betatron wavenumber and  $K = (2/\gamma_0^3\beta_0^3)I_0/I_A = \theta_p^2r_b^2/2$  is the relativistic Perviance definition, where  $I_A = 17kA$  is Alfvén's current. The solution of (2.36) for  $k_0 = \bar{\epsilon} = 0$  (space-charge dominated transport beam expansion in free space) is given in [27]. It yields that within the section  $-L_d/2 < z < L_d/2$ , where  $L_d = \pi/2\theta_{pr}$ , the envelope expansion is only  $r(\pm L_d/2) = 1.15r_{b0}$ . From the definition of space-charge

dominated beam expansion regime, the fourth term in (2.36) must be negligible relative to the third. To satisfy this condition the emittance must also satisfy:

$$\epsilon_n \ll (2I_0/I_A\gamma_0\beta_0)^{1/2}r_{b0} = (2^{5/2}/\pi)(I_0/I_A\beta_0^2\gamma_0^2)L_d \quad (2.37)$$

This condition needs to be satisfied only for a beam propagating in free space. It is not necessary if the beam is guided without expansion by means of focusing elements ( $k_0 \neq 0$ ) or possibly by partial beam charge neutralisation.

## 2.5 Noise Dynamics in Free Drift Transport

In a free drift beam transport section with uniform beam parameters ( $\theta_p(z) = \theta_p$  and  $W(z) = W_d$  are  $z$ -independent), equations (2.27) and (2.28) result in the following dynamic equations for the spectral current and kinetic voltage parameters:

$$\check{i}(z, \omega) = [\cos \phi_p \check{i}(0, \omega) - i(\sin \phi_p/W_d)\check{V}(0, \omega)]e^{i\phi_b(z)} \quad (2.38)$$

$$\check{V}(z, \omega) = [-iW_d \sin \phi_p \check{i}(0, \omega) + \cos \phi_p \check{V}(0, \omega)]e^{i\phi_b(z)} \quad (2.39)$$

where  $\phi_b = \frac{\omega}{v_z}z$ ,  $\phi_p = \theta_{pr}z$ ,  $\theta_{pr} = r_p \frac{\omega_p}{v_0}$ ,  $\omega_p = (e^2 n_0 / m \epsilon_0 \gamma^3)^{1/2}$ ,  $W_d = \sqrt{\mu_0 / \epsilon_0} / k \theta_{pr} A_e$ .

A more convenient way to write and use these equation (and for transformations of different sections) are the transformation matrices [6]. Transformation matrix for a drift section will be then written as:

$$M_d = \begin{pmatrix} \cos \phi_{pr} & -i \frac{i}{W_d} \sin \phi_{pr} \\ -i W_d \sin \phi_{pr} & \cos \phi_{pr} \end{pmatrix} \quad (2.40)$$

Equations (2.38) and (2.39) are the well known plasma oscillation equations

of a space charge column, as viewed in the laboratory frame when the plasma is drifting. The initial current and kinetic-voltage modulation amplitudes are not known when they are generated by a random process of electrons injection into the drift section at random energies (within a given range of small energy spread  $\delta E_c$  around the center energy  $\gamma_0 mc^2$ ). From the classical one dimensional shot-noise theory (see Appendix) [13][21]:

$$\overline{|\check{i}(0, \omega)|^2} = eI_b \quad (2.41)$$

$$\overline{|\check{V}(0, \omega)|^2} = \frac{(\delta E_c)^2}{eI_b} \quad (2.42)$$

here  $\delta E_c$  is the longitudinal energy spread in the beam. In low noise vacuum tube guns it is ideally limited by the cathode temperature ( $\delta E_c \cong k_B T_c$  where  $T_c$  is the cathode temperature), but it is significantly increased during the acceleration processes in an RF-gun injector and accelerator. The statistical averaging symbol corresponds to averaging over the initial entrance times of the electrons  $t_0$  and their velocity distribution.

Taking the average of the absolute value squares of equations (2.38) and (2.39), and assuming that the current noise and velocity noise are initially uncorrelated ( $\overline{\check{i}(\omega)\check{v}(\omega)} = 0$ ) we get expression for the spectral current and kinetic voltage evolution in free drift:

$$\overline{|\check{i}(L_d, \omega)|^2} = \overline{|\check{i}(0, \omega)|^2} \cos^2 \phi_p + \frac{1}{W_d^2} \overline{|\check{V}(0, \omega)|^2} \sin^2 \phi_p \quad (2.43)$$

$$\overline{|\check{V}(L_d, \omega)|^2} = \overline{|\check{V}(0, \omega)|^2} \cos^2 \phi_p + W_d^2 \overline{|\check{i}(0, \omega)|^2} \sin^2 \phi_p \quad (2.44)$$

It is instructive to examine equations (2.38), (2.39) (absolute value squared

and averaged) in the limits:

$$\overline{|\check{i}(0, \omega)|^2} \gg \overline{|\check{V}(0, \omega)|^2} / W_d^2 \quad (2.45)$$

and

$$\phi_p \ll 1 \quad (2.46)$$

These are conditions for dominant current shot-noise and small space-charge collective interaction effect along the beam transport line. In this case, first order expansion results in:

$$\overline{|\check{i}(L_d, \omega)|^2} = \overline{|\check{i}(0, \omega)|^2} \cos^2 \phi_p \cong \overline{|\check{i}(0, \omega)|^2} \quad (2.47)$$

$$\overline{|\check{V}(L_d, \omega)|^2} = \overline{|\check{i}(0, \omega)|^2} W_d^2 \sin^2 \phi_p \cong \overline{|\check{i}(0, \omega)|^2} W_d^2 \theta_{pd}^2 L_d^2 \quad (2.48)$$

where  $z = L_d$  is the length of the interaction (drift) section. In high energy accelerators used for FELs both inequalities (2.45), (2.46) are usually satisfied in the beam transport line preceding the FEL.

Nevertheless, though the space-charge interaction effect on the current shot-noise level is usually negligible (2.47) in the normal beam transport line of RF-Linacs, there may be a focused beam waist transport section of a high current beam, in which plasma oscillation phase  $\phi_p (< 1)$  is still large enough to make the generated velocity noise (2.48) exceed the initial velocity noise level of the beam  $\overline{|\check{V}(0, \omega)|^2}$ . This random energy "micro-bunching" turns into enhanced partially coherent current (density) noise when passed through a dispersive element like a chicane. It is responsible for effects like micro bunching instability [28], coherent OTR [8] and current noise amplifiers [29].

## 2.6 Dispersive Transport

The analysis can be generalized to transport through a dispersive section [13], [21]. Particularly, for transport through a transverse magnetic field that may vary in the axial dimension  $B_{\perp}(z)$ , one defines a normalized transverse momentum parameter:

$$a_{\perp}(z) = \frac{e}{mc} \int_0^z B_{\perp}(z') dz' \quad (2.49)$$

and an axial relativistic Lorentz factor:

$$\gamma_{z0}^2 = (1 - \beta_{z0}^2)^{-1} = \frac{\gamma_0^2}{1 + a_{\perp}^2(z)} \quad (2.50)$$

For this case, we redefine the small signal kinetic voltage parameter (2.7) and plasma wavenumber parameter (2.17) as:

$$\check{V}(z, \omega) = -\frac{m_0 c^2}{e} \gamma_{z0}^2 \gamma_0 \beta_{z0} \check{\beta}_z(z, \omega) \quad (2.51)$$

$$\begin{aligned} \theta_{pr}^{disp}(z) &= r_p \frac{\omega_{p0}(z)}{c \beta_z(z)} = r_p \sqrt{\frac{e^2 n_0(z)}{\epsilon_0 m_0 \beta_z(z)^3 \gamma_0 \gamma_z^2(z)}} = \\ &= \frac{r_p}{\beta_z(z) \gamma_z(z)} \sqrt{\frac{I_0 Z_0}{\frac{m_0 c^2}{e} \gamma_0 \beta_0 A_e(z)}} \quad (2.52) \end{aligned}$$

With these definitions Eqs. (2.10), (2.11) for the fast varying variable  $\check{I}(z, \omega)$  and  $\check{V}(z, \omega)$ , and Eqs. (2.24), (2.25) for the slow varying variables  $\check{i}(z, \omega)$ ,  $\check{v}(z, \omega)$  stay intact.

Eqs. (2.24), (2.25) can be casted into a formally compact form, valid for

general  $z$  dependent transport parameters:

$$\frac{d}{d\phi_p} \check{i} = -\frac{i}{W(z)} \check{v} \quad (2.53)$$

$$\frac{d}{d\phi_p} \check{v} = -iW(z)\check{i} \quad (2.54)$$

where

$$\phi_p(z) = \int_0^z \theta_{pr}(z') dz' \quad (2.55)$$

$$W(z) = Z_0 r_p^2 / (k A_e \theta_{pr}(z)) \quad (2.56)$$

where  $Z_0 = \sqrt{\mu_0/\epsilon_0}$ , and  $\theta_{pr}(z)$  is given by Eq. (2.52).

In the general case when  $\phi_{pr}(z)$  and  $W(z)$  are  $z$  dependent and known, the coupled differential equations (2.24) (2.25) can be generally solved numerically in terms of the initial conditions [10]. However, it is useful to derive out of this general linear formulation approximate analytic expressions by employing an iterative integration procedure on (2.53) (2.54) in the dispersive section in which  $W = W(z)$ . This is valid if the collective interaction effect is small in this section. The result of the first order iteration is:

$$\begin{pmatrix} \check{i}(L, \omega) \\ \check{v}(L, \omega) \end{pmatrix} = \begin{pmatrix} 1 - \int_0^{\phi_p(L)} \frac{1}{W(\phi_p)} \int_0^{\phi_p} W(\phi'_p) d\phi'_p d\phi_p & -i \int_0^{\phi_p(L)} \frac{d\phi_p}{W(\phi_p)} \\ -i \int_0^{\phi_p(L)} W(\phi_p) d\phi_p & 1 - \int_0^{\phi_p(L)} W(\phi_p) \int_0^{\phi_p} \frac{d\phi'_p}{W(\phi'_p)} d\phi_p \end{pmatrix} \times \begin{pmatrix} \check{i}(0, \omega) \\ \check{v}(0, \omega) \end{pmatrix} \quad (2.57)$$

We now specify to the case where the  $z$  dependence of  $W$  and  $\theta_{pr}$  is due to

the variation of  $\gamma_{z0}(z)$  as the beam propagates in a transverse magnetic field (e.g. Chicane).

The compact and general presentation of the transfer matrix (2.57) in terms of the beam plasma phase  $\phi_p$  becomes explicit when expressed in terms of  $z$  by substitution of  $d\phi_p = \theta_{pr}(z)dz$ . For an ultra-relativistic beam, and assuming that  $r_p^2/A_e$  does not vary significantly with  $z$ , such that the axial variation of the beam parameters is only due to the transverse magnetic field:  $\theta_{pr}^2(z) = \theta_{prd}^2(1 + a_\perp^2(z))$  and  $W(z) = W_d\theta_{prd}/\theta_{pr}(z) = W_d(1 + a_\perp^2(z))^{-1/2}$ . Here  $\theta_{prd}$  and  $W_d$  are respectively the constant reduced plasma wave-number and the beam impedance in the absence of magnetic field ( $\gamma_{z0} = \gamma_0$ ).

For a magnetic structure of length  $L_m$  [13]:

$$\underline{\underline{M}}_m = \begin{pmatrix} 1 - \theta_{prd}^2 \int_0^{L_m} z(1 + a_\perp^2(z))dz & -i\frac{\theta_{prd}}{W_d} \int_0^{L_m} (1 + a_\perp^2(z))dz \\ -iW_d\theta_{prd}L_m & 1 - \theta_{prd}^2 \int_0^{L_m} \int_0^z (1 + a_\perp^2(z'))dz'dz \end{pmatrix} \quad (2.58)$$

The matrix element  $M_{m12}$  describes the dispersion effect of beam current modulation due to energy modulation at the entrance. It is related to the momentum compaction parameter (2.83) by [18]:

$$R_{56} = -\frac{1}{\gamma_0^2} \int_0^{L_m} (1 + a_\perp^2(z))dz \quad (2.59)$$

The process of collective plasma oscillation continues to take place in the dispersive section just as in the drift section, and its effect is still kept in the matrix element to second order in  $\theta_{pr}$ . If the dispersive section length  $L_m$  is short, the space charge effects can be neglected in the dispersion section. This

results in a simple expression for the transfer matrix of the dispersive section [13], [30]:

$$\underline{\underline{M}}_m = \begin{pmatrix} 1 & i\frac{\gamma_0^2\theta_{prd}}{W_d}R_{56} \\ -iW_d\theta_{prd}L_m & 1 \end{pmatrix} \quad (2.60)$$

If the dispersive section is long, the collective effect in it should not be neglected. For a symmetric chicane it is possible to express all terms in (2.58) in terms of  $R_{56}$ . The explicit form of the transfer matrix (2.58) in this case can be derived by direct integration and use of definition (2.59):

$$\underline{\underline{M}}_m = \begin{pmatrix} 1 + \gamma_0^2\theta_{prd}^2L_mR_{56}/2 & i\frac{\gamma_0^2\theta_{prd}}{W_d}R_{56} \\ -iW_d\theta_{prd}L_m & 1 + \gamma_0^2\theta_{prd}\int_0^{L_m}R_{56}(z)dz \end{pmatrix} \quad (2.61)$$

### 2.6.1 $R_{56}$ estimation for the case of a symmetric chicane

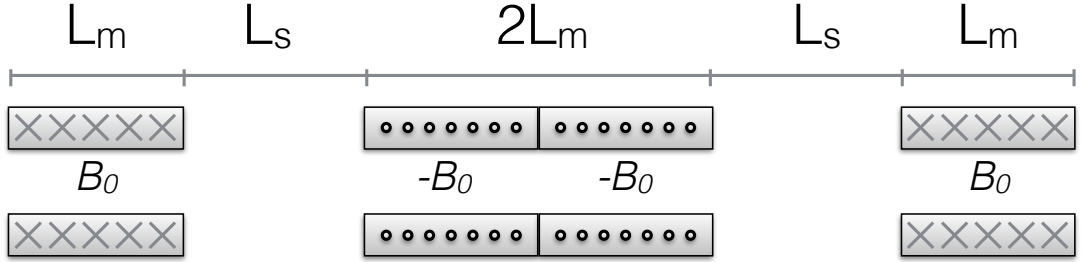


Figure 2.1: Schematic drawing of the chicane drift and magnetic field sections.

The common (symmetric) chicane is divided into magnetic field sections and drift sections as described in figure 2.1. The magnetic field amplitude ( $B_0$ ) and the lengths of the magnetic field sections ( $L_m$ ) and drifts ( $L_s$ ) in a symmetric chicane are similar, as drawn in figure 2.1. We defined in section 2.6 the  $R_{56}$  parameter (2.59) (integrated from 0 to  $L$ ) and the normalized transverse momentum

parameter (2.49). Here we also define the transverse normalised velocity:

$$\beta_{\perp} = \frac{1}{\gamma} a_{\perp} \quad (2.62)$$

and the transverse deflection:

$$x_{\perp} = \frac{1}{\beta} \int_0^z \beta_{\perp}(z') dz' \quad (2.63)$$

for convenience, we also define  $b(z) = \frac{e}{mc} B_{\perp}(z)$ . and write the equation (2.49) as  $a_{\perp}(z) = \int_0^z b(z') dz'$ .

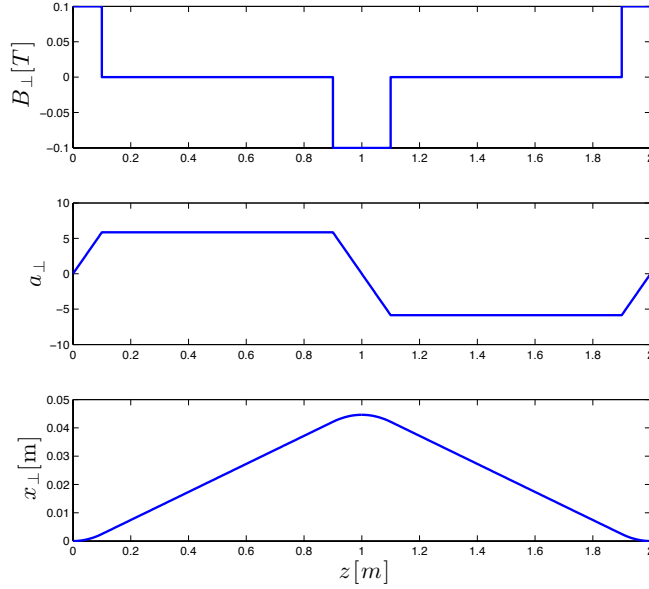


Figure 2.2: The magnetic field  $B_{\perp}(z)$ , the normalized transverse momentum parameter  $a_{\perp}(z)$  and the transverse deflection  $x_{\perp}$  for a specific example of a symmetric chicane with parameters  $L = 2m$ ,  $L_m = 0.1m$ ,  $L_s = 0.8m$  and magnetic field amplitude of  $B_0 = 0.1T$ .

Figure 2.2 presents the magnetic field, the normalized transverse momentum parameter and the transverse deflection for a specific example of a symmetric chicane with parameters  $L = 2m$ ,  $L_m = 0.1m$ ,  $L_s = 0.8m$  and magnetic field

amplitude of  $B_0 = 0.1T$ . For a general case we will write the magnetic field along the chicane:

$$B(z) = \begin{cases} B_0 & 0 < z < L_m \\ 0 & L_m < z < L_m + L_s \\ -B_0 & L_m + L_s < z < L_m + L_s + 2L_m \\ 0 & 3L_m + L_s < z < 3L_m + 2L_s \\ B_0 & 3L_m + 2L_s < z < 4L_m + 2L_s \end{cases} \quad (2.64)$$

and the the normalized transverse momentum parameter:

$$a_{\perp}(z) = \begin{cases} b_0 z & 0 < z < L_m \\ b_0 L_m & L_m < z < L_m + L_s \\ b_0 L_m - b_0(z - L_m - L_s) & L_m + L_s < z < L_m + L_s + 2L_m \\ -b_0 L_m & 3L_m + L_s < z < 3L_m + 2L_s \\ -b_0 L_m + b_0(z - 3L_m - 2L_s) & 3L_m + 2L_s < z < 4L_m + 2L_s \end{cases} \quad (2.65)$$

using the symmetry of  $a_{\perp}^2(z)$  around  $2L_m + L_s$  we can calculate  $R_{56}$  by integration to  $2L_m + L_s$  and multiply the result by 2. The result is an exact estimation of  $R_{56}$  for the case of a symmetric chicane:

$$R_{56} = \frac{1}{\gamma^2} \left[ L + 2b_0^2 L_m^2 \left( \frac{2}{3} L_m + L_s \right) \right] \quad (2.66)$$

We can write an approximate expression for the case of  $L_m \ll L_s$ :

$$R_{56} = \frac{1}{\gamma^2} [L + 2b_0^2 L_m^2 L_s] \quad (2.67)$$

This solution can be compared to the more common approach for  $R_{56}$  estimation - using the deflection angle:

$$\sin \theta = \frac{\beta_{0\perp}}{\beta} = \frac{1}{\gamma\beta} a_{\perp}(L_m < z < L_m + L_s) = \frac{1}{\gamma\beta} b_0 L_m \quad (2.68)$$

using  $\beta \approx 1$  and  $\sin \theta \approx \theta$  one obtains:

$$R_{56} = \frac{1}{\gamma^2} L + 2\theta^2 L_s \simeq \left( \frac{1}{\gamma^2} + \theta^2 \right) L \quad (2.69)$$

or in terms of the maximal displacement  $x_{\perp} = \theta L/2$ :

$$R_{56} = \frac{1}{\gamma^2} L + 4 \frac{x_{\perp}^2}{L} \quad (2.70)$$

Considering the exemplary case described in figure 2.2, and using the calculated transverse deflection (2.63) (4.5cm), the  $R_{56}$  resulting from the exact calculation (2.66) is 4.4mm, while using the geometrical expression (2.70) the result is 4.2mm. We can see that the geometrical expression is relatively accurate when dealing with a symmetric chicane in the limit of  $L_m \ll L_s$ . However, for a case of a non-symmetric chicane with different magnetic field amplitudes as presented in the exemplary case of the chicane in SPARC (2.6.2), one must use the exact approach in order to obtain a good estimation of the  $R_{56}$  parameter.

### 2.6.2 Exemplary case of $R_{56}$ estimation - SPARC FEL

The SPARC FEL is a seeded FEL located in Frascati, Rome. It has a seeding laser which is tuned to the resonance of the FEL. In the beam-laser intersection point, a small chicane, which includes a dipole magnet and three beam correctors (small deflecting magnets). The correctors deflect the beam off-axis and than

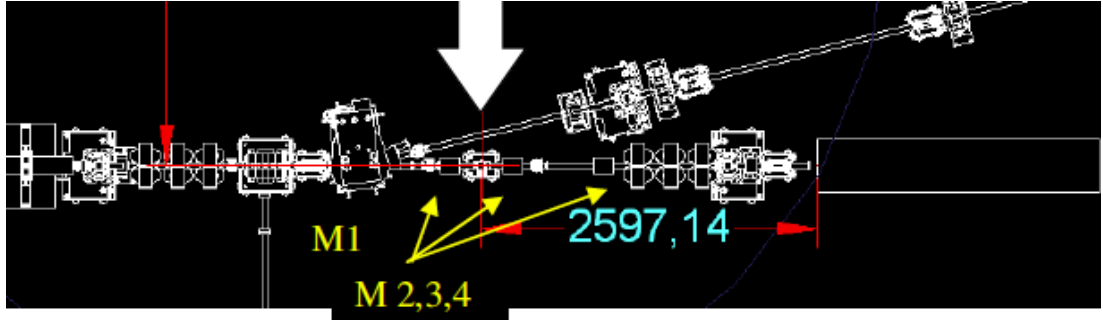


Figure 2.3: SPARC's small chicane. M1 is the bending dipole and the 3 other magnets are M 2,3,4 (marked in yellow arrows)

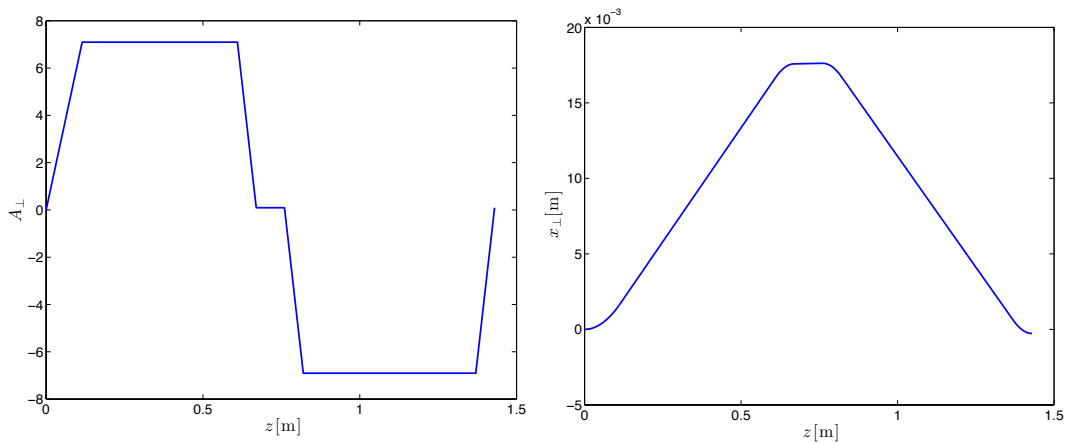


Figure 2.4: The normalized transverse momentum parameter  $a_{\perp}$  and the transverse deflection within the chicane, as a function of  $z$  in SPARC's chicane

back on-axis, in order to allow the laser mirror in. This chicane is schematically drawn in figure 2.3. We calculate the maximal  $R_{56}$  coefficient obtainable in this scheme using the amplitude of the magnetic field in the chicane correctors, as well as the length of the magnetic field and the use equations (2.59) and (2.49).

In this chicane, the magnetic field amplitude is  $0.1875T$ , the dipole magnet length is  $0.12m$  and the correctors length is  $0.06m$ . Figure 2.4 plots the calculated normalized transverse momentum parameter  $a_{\perp}$  and the transverse deflection within the chicane, as a function of  $z$ . Integrating these results using (2.59) allows us to estimate the maximal  $R_{56}$  value for this set-up to be  $\approx 1mm$ .

## 2.7 Collective-Interaction Regime

The observation of the energy fluctuations collective interaction enhancement effect in LCLS was manifested by observation of enhanced Optical Transition Radiation (OTR) from a foil screen placed in the way of the electron beam after it was transported through a focused waist and a magnet dipole bend. In the first publications of the LCLS team few years ago [4] this enhanced OTR radiation measurements effect were titled "unexplained physics" observation. At present, these observations are understood indeed as manifestation of the longitudinal Coulomb energy modulation (2.48) due to the axial Coulomb electric field of the electron beam current shot noise in the beam waist section. The enhanced energy fluctuation noise transformed into enhanced current (density) fluctuations (noise) due to the momentum compaction coefficient ( $R_{56}$ ) of the energy dispersive bend. This produced the observed enhanced coherent OTR (COTR) emission from the screen.

The study of beam micro-bunching effect has become of substantial interest in FEL physics [24] [5]. However all of the research done so far is only in the limit of small collective interaction effect. In this research, we study the collective interaction noise dynamics beyond the limit  $\phi_p < 1$ . Specifically, of great interest is the case:

$$\phi_p = \theta_p L_d = \pi/2 \quad (2.71)$$

in this case, it turns out of Eqs. (2.38), (2.39) that there is full transformation of the velocity noise into density noise and vice versa:

$$\overline{|\check{i}(L_d, \omega)|^2} = \overline{|\check{V}(0, \omega)|^2} / W_d^2 \quad (2.72)$$

$$\overline{|\check{V}(L_d, \omega)|^2} = \overline{|\check{i}(0, \omega)|^2} W_d^2 \quad (2.73)$$

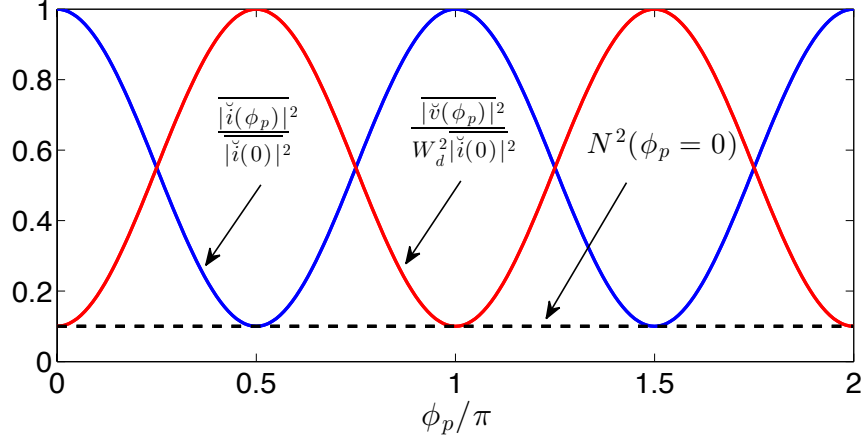


Figure 2.5: The noise intensities (current noise - blue curve, kinetic voltage noise - red curve) in a free drift section with constant impedance in a case of a current noise dominated beam ( $N^2 = 0.1$ ).

Here we introduce a useful parameter of "noise-dominance factor" -  $N$ , expressed in terms of the initial conditions of the noise parameters. It is defined as the impedance-weighted ratio between the averaged squares of the amplitudes of the kinetic voltage noise and current noise at  $z = 0$ . Namely:

$$N^2 \equiv \frac{\overline{|\check{v}(0, \omega)|^2}}{\overline{|\check{i}(0, \omega)|^2} W_d^2} \quad (2.74)$$

Using the noise dominance parameter, we can rewrite the equation for the noise intensities as:

$$\overline{|\check{i}(L_d)|^2} = \overline{|\check{i}(0)|^2} (\cos^2 \phi_p + N^2 \sin^2 \phi_p) \quad (2.75)$$

$$\overline{|\check{v}(L_d)|^2} = W_d^2 \overline{|\check{i}(0)|^2} N^2 \left( \cos^2 \phi_p + \frac{1}{N^2} \sin^2 \phi_p \right) \quad (2.76)$$

The noise intensities in a free drift section with constant parameters vary periodically with the  $\phi_p$  period  $\pi$  (See Fig. 2.5). When the current-noise at

$z = 0$ , is dominant, namely:  $N^2 < 1$ , then the current noise spectral density decreases and the kinetic voltage noise spectral density increases up to the point of quarter plasma oscillation length where:

$$\phi_p = \pi/2 \quad (2.77)$$

and

$$\frac{\overline{|\check{i}(\phi_p = \pi/2, \omega)|^2}}{\overline{|\check{i}(0, \omega)|^2}} = N^2 < 1 \quad (2.78)$$

$$\frac{\overline{|\check{v}(\phi_p = \pi/2, \omega)|^2}}{\overline{|\check{v}(0, \omega)|^2}} = \frac{1}{N^2} > 1 \quad (2.79)$$

At this point the current-noise is minimal (noise gain is  $N^2 \ll 1$ ), but the velocity noise is maximal.

The noise dominance parameter  $N$  can be evaluated directly from the beam parameters if one assumes that there is no correlation between the e-beam electron velocity and their positions (or initial position crossing time). This is the situation at the cathode or when all collective excitations are damped. In this case the spectral power of the beam current noise is given by the classical current shot-noise expression (2.41) and the velocity noise is given by (Appendix 7.1):

$$\overline{|c\check{\beta}_z(\omega)|^2} = \frac{\langle |c\check{\beta}_z(\omega)|^2 \rangle_T}{T} = \frac{e}{I_0} c\check{\beta}_{th}^2 \quad (2.80)$$

where  $\beta_{th}$  is the beam axial velocity spread. The corresponding spectral power of the kinetic voltage is:

$$\overline{|\check{V}(\omega)|^2} = \left(\frac{mc}{e}\gamma^3\beta\right)^2 \frac{e}{I_0} c\check{\beta}_{th}^2 \quad (2.81)$$

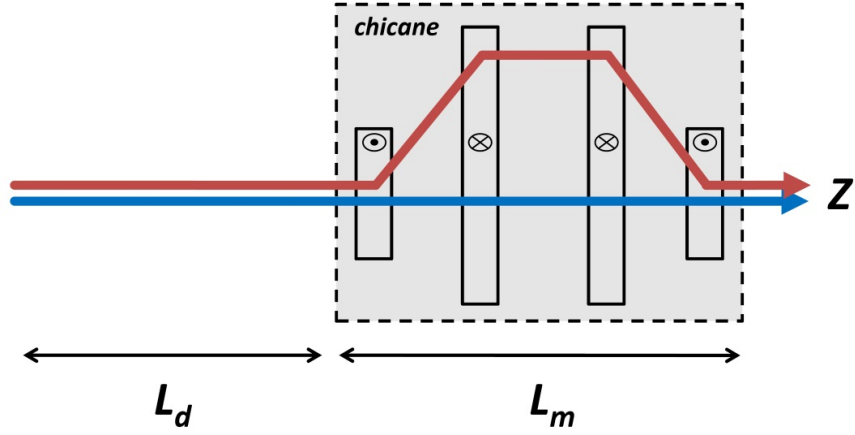


Figure 2.6: Schematics of beam transport through a drift section, followed by an ideal dispersive section (chicane).

Using definition (2.26) for the beam impedance, the normalised noise dominance parameter (2.74) of beam with uncorrelated electron distribution is:

$$N^2 = \frac{k^2}{\theta_p^2 \beta_0^4} \check{\beta}_{th}^2 \quad (2.82)$$

## 2.8 Drift and Subsequent Transport Through a Dispersive Section

In this scheme a short e-beam drift length is used and followed by a dispersive section (chicane), as shown in Figure 2.6. The LSC interaction in the drift section is used only in order to generate sufficient axial velocity modulation (energy micro-bunching), as it happens in the first stage of plasma oscillation, described in the previous section.

In a balanced dispersive section, electrons of lower velocity (energy) traverse a longer way than faster electrons, and all get back to propagation on line after the section. Thus, the slower electrons lag behind the fast ones. This is the

case even in free drift transport, which means that also free space is dispersive for particle propagation. However, in a magnetic structure like a chicane, this process is significantly enhanced.

The electrons in the front part of a density bunch that acquire in the drift section higher velocity than the center bunch electrons are situated then further ahead of the bunch after passing through the dispersive section. Similarly, the electrons in the back part of the drifting bunch, that were slowed down in the drift section, are pushed further back of the bunch after passing the dispersive section. The result is an enhanced spreading of all density bunches. This process of velocity modulation in the drift section and subsequent bunch spreading in the dispersive section can produce local beam homogenisation and suppressed current modulation in a total beam-transport length shorter than in the first method. There is no need in this case to go through a quarter plasma oscillation length, where velocity bunching is maximal and current bunching is minimal. A shorter drift section can produce sufficient velocity modulation, that turns in the dispersive section into current (density) modulation. This modulation is out-of-phase relative to the initial current modulation and, thus, may cancel the original current modulation that started the process.

The time delay  $\delta\tau$  of electrons with excess velocity or momentum  $\delta p$  in a dispersive section is characterised by the parameter  $R_{56}$ , defined by [18]:

$$R_{56} = -c\beta_0 \frac{\partial\tau}{\partial\left(\frac{\delta p}{P_0}\right)} \quad (2.83)$$

It is usually a negative quantity. In most common chicanes, that are used for pulse compression, the  $R_{56}$  parameter value is rather large. A small value of  $R_{56}$  is needed in order to suppress the current shot-noise (typically  $R_{56} \sim mm$ ).

Commonly the large value of  $R_{56}$  causes excessive effect of out-of-phase density bunching after the dispersive section. This over-bunching effect can produce current shot-noise gain (micro-bunching instability), which is usually an undesirable effect. It can be, however, taken advantage of and used in a controlled way in a cascade of drift and dispersion sections as a noise amplifier for wide band frequency generation of SASE radiation [29]. The drift-dispersion noise suppression scheme was proposed by Ratner et al for a cold beam [30], and was demonstrated experimentally in [11]. Gover et al presented in [13] a more comprehensive theoretical model that includes the effects of velocity noise in the beam and possible variation of parameters along the transport line. The formulation is useful for analysis of both noise suppression and gain.

### **2.8.1 Beam noise micro-dynamics in a dispersive section following a drift section**

We now draw attention to the case shown schematically in Figure 2.6, where some energy modulation takes place in a drift section because of the random current modulation associated with the e-beam charge granularity (shot-noise) in the drift section  $L_d$ . The beam is then injected into an ideal magnetic dispersive section of length  $L_m$  with the current noise and energy noise being correlated. Most of the velocity modulation takes place in the drift section, and the current modulation takes place primarily in the dispersive section [30]. However, in principle both processes take place in both sections. The matrix notation [13] enables complete description of the velocity and current noise micro-dynamics in both sections. The comprehensive transfer matrix for current and velocity modulation is found explicitly from the product  $\underline{\underline{M}} = \underline{\underline{M}}_m \underline{\underline{M}}_d$  of the drift and dispersion matrices (2.61),(2.40).

If, for simplicity, we neglect the second order space-charge terms in the diagonal parameters of (2.61), the total transfer matrix becomes:

$$\underline{\underline{M}} = \begin{pmatrix} \cos \phi_{pd} + \gamma_0^2 \theta_{pd} R_{56} \sin \phi_{pd} & -\frac{i}{W_d} (\sin \phi_{pd} - \gamma_0^2 \theta_{pd} R_{56} \cos \phi_{pd}) \\ -i W_d (\theta_{pd} L_m \cos \phi_{pd} + \sin \phi_{pd}) & \cos \phi_{pd} - \theta_{pd} L_m \sin \phi_{pd} \end{pmatrix} \quad (2.84)$$

where  $\phi_{pd}$  is the plasma phase accumulated in the drift section and  $\theta_{pd}$ ,  $W_d$  are the free drift constant parameters. Applying the matrix  $\underline{\underline{M}}$  on the input vector  $(\check{i}(0, \omega), \check{v}(0, \omega))$  and calculating the averaged absolute value squared of the output parameters (at the point  $L = L_d + L_m$ ), one obtains:

$$\frac{\overline{|\check{i}(L, \omega)|^2}}{\overline{|\check{i}(0, \omega)|^2}} = (\cos \phi_{pd} + \gamma_0^2 \theta_{pd} R_{56} \sin \phi_{pd})^2 + N^2 (\sin \phi_{pd} - \gamma_0^2 \theta_{pd} R_{56} \cos \phi_{pd})^2 \quad (2.85)$$

$$\frac{\overline{|\check{v}(L, \omega)|^2}}{W_d^2 \overline{|\check{i}(0, \omega)|^2}} = (\sin \phi_{pd} + \theta_{pd} L_m \cos \phi_{pd})^2 + N^2 (\cos \phi_{pd} - \theta_{pd} L_m \sin \phi_{pd})^2 \quad (2.86)$$

where  $N^2 = \overline{|\check{v}(0, \omega)|^2} / W_d^2 \overline{|\check{i}(0, \omega)|^2}$  (the weighted ratio of initial current noise and energy noise), and it is assumed that the current and energy noises are not correlated at the entrance to the drift section. Note that the first order (in terms of  $\theta_p$ ) space charge term in the  $\underline{\underline{M}}_{m21}$  element of (2.60) affects only the velocity noise gain expression (2.86), but there is no effect of space-charge dynamics on the current gain (2.85) up to first order.

In the limit of a current shot-noise dominated beam  $N^2 \ll 1$ , (2.85) reduces into:

$$G = \frac{\overline{|\check{i}(L, \omega)|^2}}{\overline{|\check{i}(0, \omega)|^2}} = (\cos \phi_{pd} - K_d \phi_{pd} \sin \phi_{pd})^2 \quad (2.87)$$

where the normalised relative compaction parameter

$$K_d = \frac{|R_{56}|}{L_d/\gamma_0^2} \quad (2.88)$$

can be interpreted as the ratio between the momentum compaction coefficients of the dispersive section and that of the free drift section.

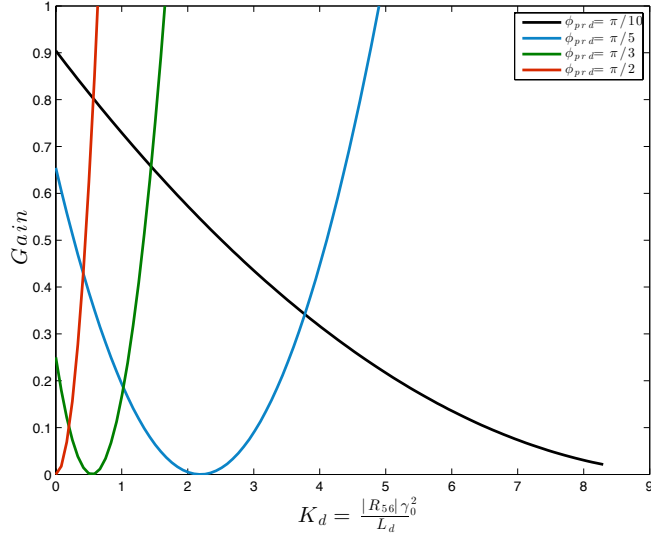


Figure 2.7: Normalized current-noise as a function of the dispersive section parameter  $K_d$  for different plasma phase values  $\phi_{pd}$  accumulated in the preceding free drift section of length  $L_d$ .

Figure 2.7 displays the current noise gain (2.87) as a function of  $K_d$  for different values of plasma modulation phase  $\phi_{pd}$  in the drift section. It appears from (2.87) that for each plasma modulation phase  $\phi_{pd}$ , it is possible to attain noise suppression by setting  $R_{56}$  in the range:

$$0 < |R_{56}| < \frac{L_d}{\gamma_0^2} \frac{1 + \cos \phi_{pd}}{\phi_{pd} \sin \phi_{pd}} \approx \frac{2L_d}{\gamma_0^2 \phi_{pd}^2} \quad (2.89)$$

and maximal suppression is attained for

$$R_{56} = \frac{L_d/\gamma_0^2}{\phi_{pd} \tan \phi_{pd}} \approx \frac{L_d/\gamma_0^2}{\phi_{pd}^2} \quad (2.90)$$

The last approximate expressions correspond to the common case  $\phi_{pd} \ll 1$ . In this case the gain expression (2.87) assumes the simple form:

$$\frac{|\check{i}(L, \omega)|^2}{|\check{i}(0, \omega)|^2} = (1 - K_d \phi_{pd}^2)^2 \quad (2.91)$$

This result is consistent with the findings of [30].

When the dispersive section is long enough (compared to the free drift section), the collective interaction that continues within the dispersive section, affects also the current noise suppression (or gain). To take into account this effect, one must keep also the second order space-charge term in the  $\underline{\underline{M}}_{m11}$  matrix element of (2.61). We take then the product  $\underline{\underline{M}} = \underline{\underline{M}}_m \underline{\underline{M}}_d$  using the more general drift and dispersion matrices (2.40),(2.61). Still assuming  $\phi_{pd} \ll 1$  and keeping second order term in  $\underline{\underline{M}}_{m11}$ , one obtains a modified expression for the total matrix element  $\underline{\underline{M}}_{11}$  and a corresponding modification of the current-noise gain expression (2.91):

$$\frac{|\check{i}(L, \omega)|^2}{|\check{i}(0, \omega)|^2} = (1 - K_d \phi_{pd}^{*2})^2 \quad (2.92)$$

where  $\phi_{pd}^*$  includes an enhancement factor that corresponds to the continued LSC interaction in the dispersive section of length  $L_m$ :

$$\phi_{pd}^* = \phi_{pd} \sqrt{1 + \frac{L_m}{2L_d}} \quad (2.93)$$

## 2.9 The Short Wavelength Limits of Noise Suppression

### 2.9.1 Ballistic electron phase spread condition in beam drift transport

In the following we analyse limitations of the validity of the fluid plasma model in the optical frequency range. A restriction on the model (and on noise suppression) is a requirement that the beam is cold enough so that bunch smearing, due to electrons axial velocity spread ( $\beta_{th}$ ), does not wash away space-charge wave bunching components at frequency  $\omega$  (and wavenumber  $k/\beta$ ) that may be excited on the beam, under a model of a cold beam (using the moment or fluid plasma equations) were found to propagate on it without decay. This condition can be expressed in terms of the optical phase spread  $\Delta\phi_b$  of the electrons along the interaction length  $L_d$ :

$$\Delta\phi_b = kL_d\Delta(1/\beta_z) = kL_d\Delta\beta_z/\beta_z^2 \ll \pi \quad (2.94)$$

This is a ballistic-electron phase spread condition, in which one assumes that for the relevant drift length, each electron retains its velocity determined by the initial axial velocity distribution. The axial velocity spread of the beam may be owing to the beam energy spread, in which case the ballistic electron phase spread condition sets a limit on the beam energy spread:

$$\Delta\gamma/\gamma_0 \ll \beta_0^3\gamma_0^3\lambda/2L_d \quad (2.95)$$

or owing to the angular spread of the beam  $\sigma'_x$ , that for a given beam width,  $\sigma_x$  sets a limit on the emittance  $\epsilon_n = \sigma_x\sigma'_x$ :

$$\epsilon_n \ll \beta_0^2\gamma_0\sigma_{x0}(\lambda/L_d)^{1/2} \quad (2.96)$$

### 2.9.2 The short wavelength condition for noise suppression in the dispersive beam transport scheme

We now address the same case as in chapter 2.8, which is a dispersive section, following a drift section. In order to evaluate the short-wavelength condition we start by differentiating (2.87) with respect to  $K_d$  using a fixed  $\phi_{pd}$ . We assume  $\phi_{pd} \ll \pi$ :

$$\frac{dG}{dK_d} \Big|_{\phi_{pd}=\text{const}} = \frac{dG}{dK_d} (1 - K_d \phi_{rd}^2)^2 + N^2 \phi_{pd}^2 (1 + K_d)^2 \quad (2.97)$$

We find the value of  $K_d$  for maximal suppression to be:

$$K_d = \frac{1 - N^2}{N^2 + \phi_{pd}^2} \quad (2.98)$$

plugging this result back in (2.87) we obtain:

$$G_{min} = \frac{N^2(1 + \phi_{pd}^2)^2}{N^2 + \phi_{pd}^2} \quad (2.99)$$

According to this result, for  $N^2 \ll 1$ , in order to achieve significant suppression ( $G \ll 1$ ), one needs to work in the region where  $1 \gg \phi_{pd}^2 \gg N^2$  and the attainable gain suppression factor is then:

$$G_{min} \approx \frac{N^2}{\phi_{pd}^2} \ll 1 \quad (2.100)$$

therefore, for any given  $N^2 (< 1)$  parameter value and any free drift section ( $\phi_{pd} < 1$ ), using a dispersive section results with a lower suppression of current noise compared with a single quater-plasma oscillation wavelength free drift section. On the other hand, using a well matched dispersive section allows a reduction of the required transport system length, and yet achieves a significant current noise

suppression. The normalized compaction parameter required to attain this gain minimum (2.98) is then:

$$K_d \approx \frac{1}{\phi_{pd}^2} \quad (2.101)$$

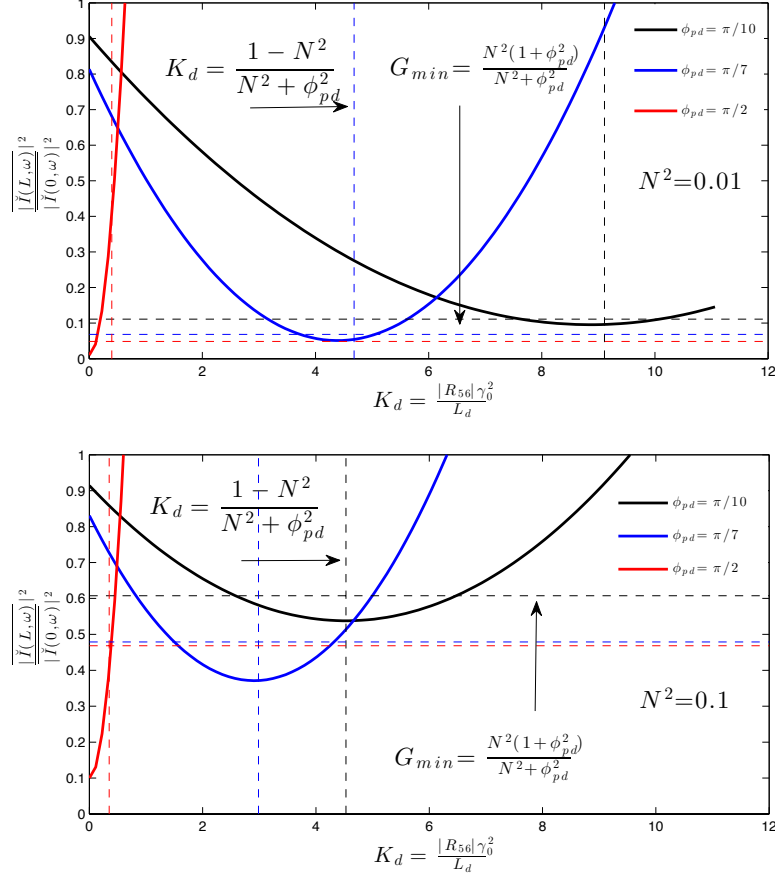


Figure 2.8: Current noise gain, for a dispersive section, following a drift section, as a function of  $K_d = R_{56}\gamma^2/L_d$  for three drift plasma phase  $\phi_{pd}$  values:  $\pi/2$ ,  $\pi/7$ ,  $\pi/10$ . (a) for  $N^2 = 0.01$  and (b) for  $N^2 = 0.1$ .

Figure 2.8 presents two plots for two different values of  $N^2$  ((a) 0.01 and (b) 0.1). For each plot we draw curves for three values of accumulated drift plasma phases ( $\pi/2$ ,  $\pi/10$ ,  $\pi/7$ ). The horizontal and vertical dashed lines represent the results of the approximated values  $K_d$  (2.98) and the gain (2.99).

In the dispersive noise suppression scheme  $\phi_{pd} \ll 1$  is required, which means that the drift section can be much shorter than the  $L_{\pi/2}$  needed in the drift suppression scheme. Since a drift length for a quarter plasma oscillation could be tens of meters for a relativistic e-beam, a short drift section, followed by a short dispersive section is advantageous in terms of space and practicality. However, one can verify in figure 2.8, that when  $N^2$  is growing (although still smaller than unity), the ability to suppress the beam noise in this case is reduced ( $N^2/\phi_{pd}^2$ ) in comparison to a suppression in a drift scheme, where the suppression factor is limited only by  $N^2$ .

### 2.9.3 Optical phase-spread neglect condition for the drift/dispersion scheme

The ballistic electron phase spread condition (2.94) was examined earlier for the case of uniform free drift. In order to estimate this condition in the case of a drift and a subsequent dispersive section, we integrate the optical frequency phase spread (2.14) over the full path of the electrons, including both sections:

$$\Delta\phi_b = k \int_0^{L_d+L_m} \Delta \left( \frac{1}{\beta_z(z)} \right) dz \ll \pi \quad (2.102)$$

Assume here that the axial velocity spread is due to energy spread  $\Delta\gamma$ . Using equation (2.50) one gets (in the limit  $\gamma_0 \ll 1$ )  $\Delta\beta_z = (\partial\beta_z/\partial\gamma)\Delta\gamma \simeq (1 + a_{\perp}^2)\Delta\gamma/\gamma_0^2$ .

With definitions (2.59)(2.88) one can express (2.102) as a sum of two optical

phase spreads accumulated in the two sections:

$$\Delta\phi_b = \frac{kL_d}{\gamma_0^2} \frac{\Delta\gamma}{\gamma_0} (1 + K_d) = N\phi_{pd}(1 + K_d) \ll \pi \quad (2.103)$$

here we identified  $N = k\Delta\gamma/\theta_p\gamma_0^3$ . We now use (2.101)  $(K_d)_{min} = 1/\phi_{pd}^2 \gg 1$  for the normalised relative compaction parameter required for maximum noise suppression. Clearly most of the phase spread accumulates in the dispersive section since  $\phi_{pd} < 1$ . Consequently, the phase spread neglect condition for the dispersive case at the conditions of maximum suppression is:

$$\frac{N}{\phi_{pd}} \ll \pi \quad (2.104)$$

Again, when  $\phi_{pd} < 1$  this condition is more stringent than the condition  $N \ll 1$  required in the drift suppression scheme.

## CHAPTER 3

# 3-D Numerical Simulations of Collective Microdynamics in an Electron Beam

### 3.1 introduction

Numerical simulations of the noise suppression effect in electron beams were performed using GPT (General Particle Tracer) [31]. The analysis of the simulation results was performed using Matlab codes. These simulations were carried out both in the particle rest frame and the laboratory frame. Results were published [9] and presented in a number of international conferences [16].

These simulations can well describe a beam with quite realistic parameters, including initial velocity spread, emittance and either flat or Gaussian transverse density profiles. In this chapter we employ the code to simulate electron-beam current noise suppression in free space drift. However, the code has more exclusive capabilities, and we have employed it to simulations of electron beam transport through dispersive sections such as focusing quadrupoles and bends. We now have a complete ability to simulate noise dynamics in every beam-line.

Micro-bunching instabilities (noise gain), have been investigated by numerous research groups for quite a while [5]. However, this research was the first to demonstrate with numerical simulations noise suppression below shot-noise in electron beam drift, in a full 3-D model using point-to-point Coulomb inter-

actions. The code allows us to understand the current noise dynamics along a complete section including all of the injector components for different beam parameters. This ability was used during the experimental research for different facilities and helped determine the proper parameters and set-up required in order to achieve noise suppression.

The output of our GPT simulation code (arrival times of particles to the end of a given transport section) makes it possible to calculate the current and velocity noise parameters at these points. Moreover, if the beam is injected into a radiation device, the particles arrival data can be used as the input for calculating the radiation output from the radiation device (e.g.. OTR element or a Wiggler). This way it can be used for simulating also radiation noise suppression. An exact formulation for calculating OTR radiation field (amplitude and phase) from individual electrons is described in the next chapter.

The combination of the electron beam micro dynamics code with the OTR computation code makes it possible to simulate OTR from the entire beam, including radiation noise suppression and coherent OTR effects.

## **3.2 General Particle Tracer (GPT) Simulations**

The 1-D (single mode) model of the noise suppression process needed to be verified within its range of validity by a 3-D study. Here we present the results of such a study based on full 3-D GPT particle simulations. In most of the 3-D simulations (in the absence of electron-optical components), the beam dynamics in the collective interaction region was computed in the rest frame of the electron beam (which moves relatively to the lab frame with velocity  $v_0$ ), by solving the motion equations of all sample particles considering the Coulomb field forces

exerted to them by all other particles in a finite dimensions bunch of electrons (long enough to regard the bunch as a caustic beam and ignore coherent edge effects).

The starting condition was a uniform or gaussian random distribution of sample particles in a pencil shaped charge bunch. The positions and velocities  $(r, v)$  were calculated for each particle  $(j)$  as a function of time  $(t)$ . In the post processing these variables were transformed to the laboratory frame  $(t, r, v)$ , using Lorentz transformation. They were calculated as a function of the position of the center of the bunch  $z = v_0 t = v_0 \gamma_0 t'$ . These were used to calculate the lab frame current and velocity noise as a function of  $z$  (see Appendix 7.1):

$$|\check{i}(\omega, z)|^2 = (q_e)^2 \left| \sum_{j=1}^N \exp[i\omega t_j(z)] \right|^2 \quad (3.1)$$

$$|\delta\check{\beta}(\omega)|^2 = \left( \frac{q_e}{I_0} \right)^2 \left| \sum_{j=1}^N (\beta_j - \bar{\beta}_{0j}) \exp[i\omega t_j(z)] \right|^2 \quad (3.2)$$

$$|\check{V}(\omega)|^2 = \left( \frac{\gamma_0^3 m c^2}{I_0} \right)^2 \left| \sum_{j=1}^N (\beta_j - \bar{\beta}_{0j}) \exp[i\omega t_j(z)] \right|^2 \quad (3.3)$$

where  $q_e$  is the charge of one macro-particle,  $\bar{\beta}_{0j}$  is the average velocity of the electrons within a wavelength range around the  $j$ th particle. Note that the micro dynamic particle velocity increment  $\delta\beta_0$  should be calculated relative to the local average velocity  $\bar{\beta}_{0j}$  and not relative to the average beam velocity  $\beta_0$ . This is done in order to take into consideration the average energy chirp effect along the bunch length due to the average space charge. The summation is performed on all the macro-particles within the pulse.

Energy	100 MeV
Pulse Current	80 A
Duration	9 pS
Radius	1 mm
Drift Length	48 m

Table 3.1: FERMI@Elettra Simulation Parameters

### 3.2.1 Beam parameters and simulation method

The simulations of the drifting beam in this exemplary case are based on parameters of the FERMI@Elettra facility (Table 3.1). For the purpose of demonstration the model is made simple: the beam does not include transverse emittance and we assumed a flat top current density distribution in both longitudinal and transverse profiles of the electron beam pulse.

The current and velocity spectral noise parameters were calculated from equations (3.1) and (3.2) in a frequency (wavelengths) range. At each wavelength it is necessary to verify that the condition:

$$n_0 A_e \lambda \beta_0 \gg 1 \quad (3.4)$$

is satisfied, where  $n_0$  corresponds to the number of particles used.

For the FERMI case, the simulations were run using GPT for several sets of random starting distributions of 30K and 60K macro-particles. In this example we investigated noise only above  $5\mu m$ , since shorter wavelengths require a much larger number of macro-particles.

The shown simulation results correspond to zero initial velocity spread. Simulations with initial axial velocity spread up to  $\Delta\beta = 0.002$ , corresponding to  $\Delta\gamma/\gamma = 0.002$  in the lab frame, produced similar results. This is in agreement

with the cold beam condition (2.34)  $\Delta\gamma/\gamma \ll \beta_0^3\gamma_0^3\lambda/2L_d$ .

### 3.2.2 Creating a pulse: Choosing a random generator

In these 3D simulations, the noise dynamics are obtained by observing a single pulse of electrons in its rest frame. We assume that the electrons ejection from the cathode that generates the electron beam pulse is a true random process. In order to create such a pulse, the electrons distribution is created by a generator of random numbers. There is a significant importance to the quality of the random generator, since initial pre-bunching caused by a poor generator might result in enhancement of such bunching and will prevent us from observing the noise suppression effect.

There are two types of random generators: pseudo random and true random generators. The pseudo random generator output is not truly arbitrary, however, its period is long enough to be considered as random, when relatively small number (in comparison to its period) is required. In our simulations we used from 30K to 200K macro-particles; for each we had to choose a set of three numbers for x,y, and z coordinates. I conducted a preliminary study to determine the quality of different random number generators. The pseudo random generator that I examined was the Matlab random generator, and the true random generator that was examined was an ultra high-speed random number generator based on a chaotic semiconductor laser [32]. Here I show the test of the two generators in representing a random process (Poisson distribution statistics) in one coordinate (axial density distribution of electrons).

As a test we used the known fact, that when the average electron beam density is defined, and the location of each particle is independent of the other ones, then the distribution of counted electron number at different sections in the array has

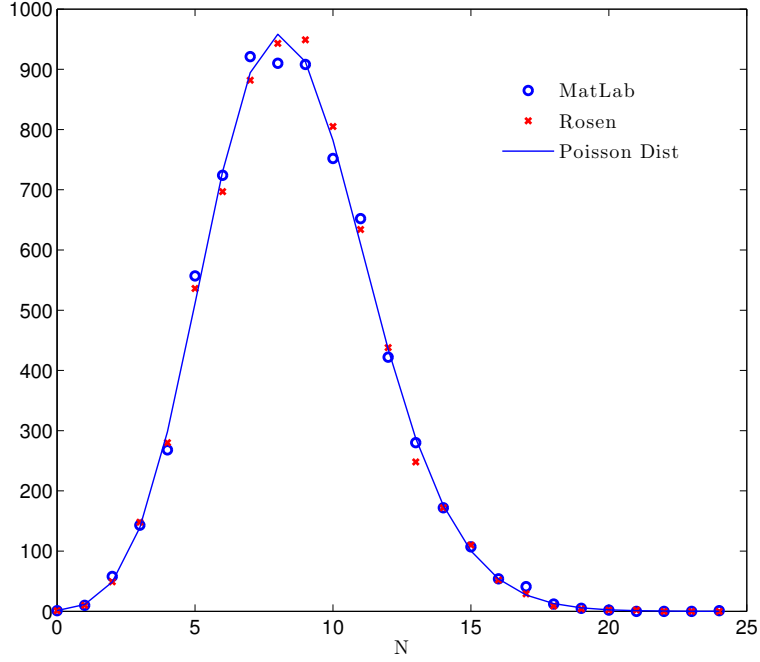


Figure 3.1: Comparison between two random generators - Rosenblu's and Matlab's. 200K numbers used and both compared to Poisson distribution curve (3.5)

a Poisson distribution characteristics [33]:

$$Pr(X = k) = \frac{\lambda^k e^{-\lambda}}{k!} \quad (3.5)$$

where  $X$  is a discrete random variable,  $k = 1, 2, \dots$ ,  $e$  is the natural logarithm and  $k!$  is the factorial of  $k$ .

We used random numbers between 0 and 1, created by the two generators, and compared their average density distribution to a poisson distribution. The results for a 200K numbers test are presented in figure 3.1. The figure displays the numerically computed current noise (3.1) at equi-spaced frequency steps. For convenience this result is shown as a function of wavelength (where the data point spacings are not equal), and the points are connected by lines. The results showed

a reasonable match of the distribution of both generators to the theoretical curve. The match of the true generator is better, but in most cases the Matlab pseudo random generator is sufficient for our purpose.

Another test used was to calculate the shot-noise current of 60K macro particles (3.1) using the two random number generators under test and comparing the result to the theoretical shot-noise formula (2.41). Figure 3.2 display the computed spectral current with the two sets of random numbers in a frequency range corresponding to  $4\mu m < \lambda < 20\mu m$ . The sample particles represented in (3.1) charge of  $q_e = 1.2 \cdot 10^{-14}C$  and beam current of  $I = 80A$ . The particles pulse duration was taken to be  $T = 9pS$ . The computed theoretical shot-noise (2.41) was:

$$eI_b = 9.6 \times 10^{-13} \frac{C^2}{S} \quad (3.6)$$

This level is compared in figure 3.2 to the average of the spectral current.

Again, the true random number generator resulted in a better match of its average noise prediction (4% off the theoretical value), compared to the pseudo-random generator ( $\approx 14\%$  difference).

### 3.3 Noise Suppression Results

The current noise variation was computed with GPT for the FERMI parameters (table 3.1), assuming an initial cold beam, as a function of drift time, and is shown in figure 3.3 for different random initial distributions. Due to the randomness of the sampled beam shot-noise, the initial shot noise level in each set was different, and therefore, in order to show the characteristics of the noise evolution the initial values of the curves are normalized.

Despite the variance between the different random starting particle distribu-

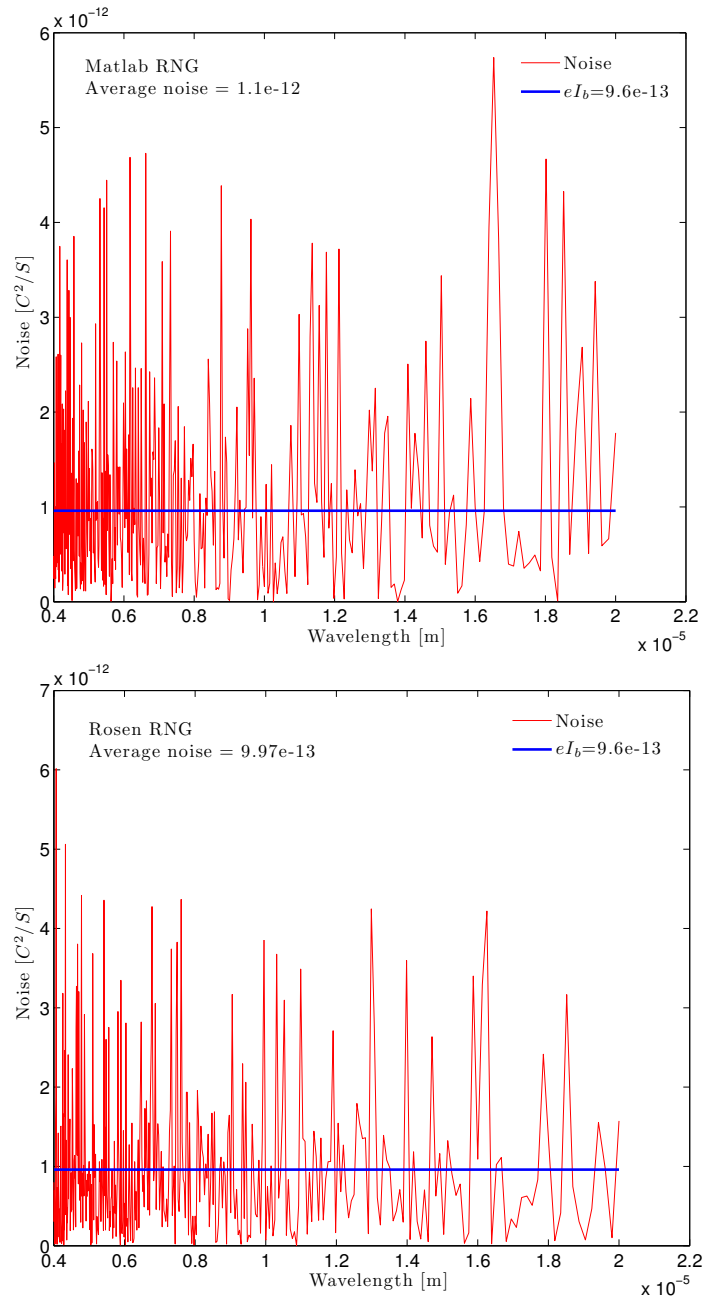


Figure 3.2: Spectral current noise from a 60K m.p. pulse created by Rosenblu's et al true random generator (a) and Matlab pseudo-random generator (b). Blue line represents the analytical Shot-noise amplitude  $eI_b$

tion sets, it is evident that there is noise suppression in all cases. Moreover, it is clear that the noise minima occur at a distance slightly longer but very close to the calculated quarter plasma oscillation length  $z = \pi c/2\omega_{pl} = 31m$ . We also calculated the velocity noise (3.2) and the corresponding kinetic voltage noise (3.3) normalised by the beam impedance  $W_d \approx 2 \times 10^3 \Omega$  (2.26) with  $r_p = 1$ , for one of the sets (figure 3.4). It reached its maximum value at the same place that the current noise reaches its minimum (quarter plasma oscillation time). This too provides good confirmation for the analytical linear single mode theory. It is quite remarkable that the simulations confirm quite well the predictions of the analytical single mode longitudinal interaction model. Note that in the 3D GPT simulations the particles are distributed randomly in the three dimensions of space, and the Coulomb force between the sample particles includes components transverse to the axial dimension.

Though the noise parameters in figure 3.4 are given in real units ( $A^2 \cdot sec$ ), they only describe the noise parameters of the sample particles. Our computer resources do not permit 1:1 sampling of the laboratory electron beam pulse. Considering the scaling of the noise with the number of particles, it is expected that the laboratory noise will be reduced relative to the simulation results by the factor of  $q_e/e$ .

### 3.4 3-D Effects and the Plasma Reduction Factor

In the parameter range  $\lambda\gamma_0\beta_0 > 2r_b$ , the single mode model holds. However, due to the finite dimensions of the beam, the plasma wave frequency deviates from the 1-D plasma frequency due to the plasma reduction factor  $r_p < 1$ . The reason for this is the fringing of the micro-bunching space charge field lines at the periphery of the beam cross-section. This reduces the effective strength of the

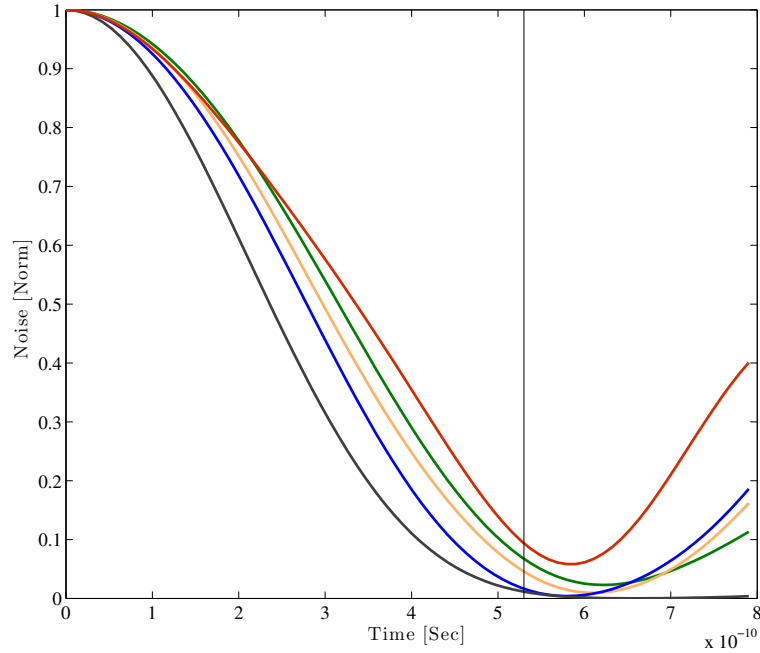


Figure 3.3: Current shot noise of  $5\mu m$ . Curves obtained from 30k macro-particles GPT simulations for 5 different initial random particle distribution sets. The vertical line represents the theoretical quarter plasma oscillation length (in lab frame)  $z = \pi c/2\omega_{pl}$

space-charge field which causes the longitudinal plasma oscillation. Therefore, in this case, the quarter-plasma oscillation length is longer. Yet, this operating regime is the desirable operating regime, since in the opposite limit (for which  $r_p = 1$ ) there may be excitation of higher order Langmuir plasma wave modes and the transverse coherence of the bunching breaks down. In this short wavelengths range, it was shown by Venturini [23], that even at short interaction length, 3-D effects wash out the transverse coherence of the bunching.

These theoretical observations are well confirmed by the calculated current noise evolution with time at different wavelengths for a particular particles simulation set (figure 3.5). The results confirm that the minimal noise point is shifted to longer drift distances for longer wavelengths.

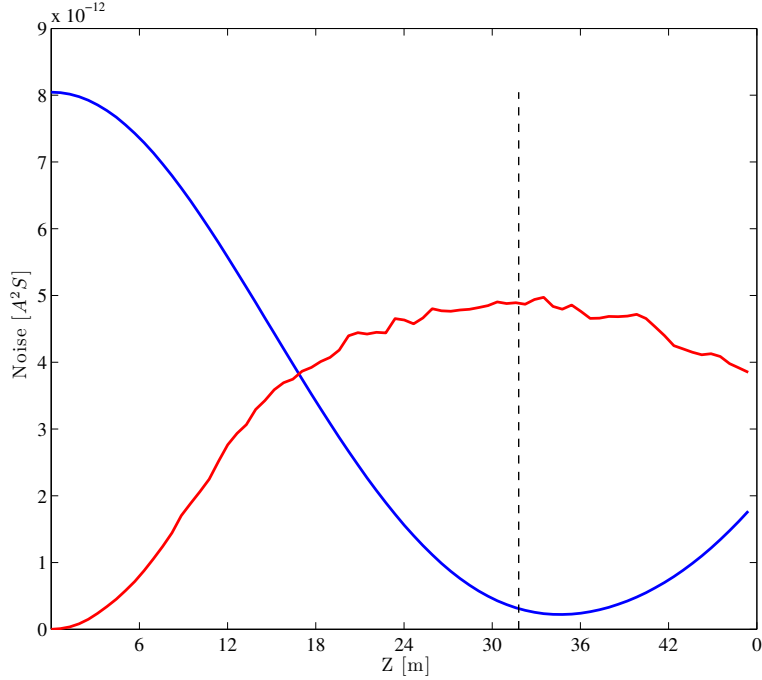


Figure 3.4: Spectral Current noise (blue) and kinetic voltage noise (red) of  $5\mu m$  normalized by the beam impedance. The curves were obtained from a 30k macro-particles GPT simulation. The vertical line represents the theoretical quarter plasma oscillation length (in lab frame)  $z = \pi c/2\omega_{pl}$

Based on [23], we estimate the plasma reduction factor of the Langmuir wave fundamental mode from:

$$r_p^2 = 1 - (kr_b/\gamma)K_1(kr_b/\gamma) \quad (3.7)$$

where  $K_1(x)$  is the modified Bessel function and  $k = 2\pi/\lambda$  is the optical wave-number. By taking the ratio between the 1-D quarter plasma oscillation length  $z = \pi c/2\omega_{pl}$  and the minimum current-noise drift length for three different wave-lengths, we calculated the plasma reduction factor for these wavelengths (marked by stars in figure 3.6). The calculated points fall quite close to the theoretical curve and confirm its go down trend.

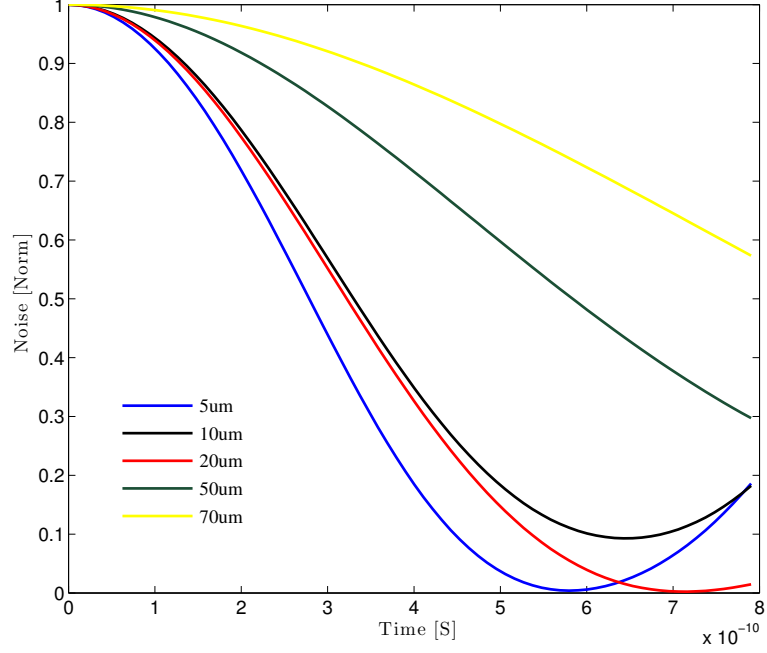


Figure 3.5: Current shot noise at different wavelengths (from 5 to  $70\mu m$ ). Results obtained from a particular 30K macro-particles GPT simulation

The conclusion of this discussion is that when  $\lambda\gamma_0\beta_0 \sim 2r_b$  is satisfied, the single mode (1-D) model is valid, and 3-D deterioration effects are negligible under condition 3.4. The model is still valid when  $\lambda \gg 2r_b/\gamma_0\beta_0$ , but the reduction of  $r_p$  shifts the maximum noise suppression point to longer lengths (figure 3.5).

### 3.5 Charge Homogenisation Effect

The spectral current shot-noise suppression effect in the laboratory frame is equivalent to spatial charge homogenisation in the e-beam rest frame. This exceptional "self ordering" effect takes place over a wide range of spatial frequencies of the beam density random spatial fluctuations (granularity).

In order to confirm this observation, we employed the GPT code to simulate

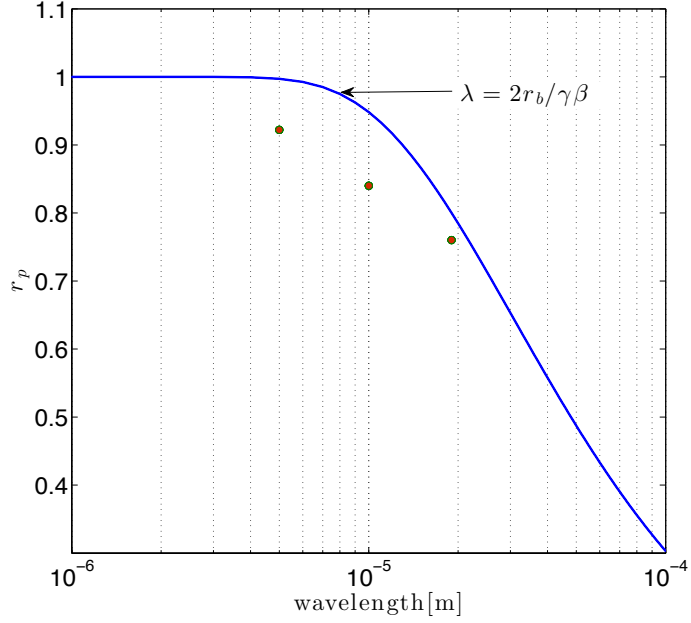


Figure 3.6: Plasma reduction factor dependence on wavelength: following (3.7) (solid curve) and from the minima of the current noise curves (red dots)). Results obtained from a particular 30k macro-particles GPT simulation

the electron beam dynamics in the beam frame using the parameters of table 3.1. However, we note that the predicted homogenisation effect is frequency dependent. At high frequencies it is limited by condition 3.4 (condition 3.4 is a physical limitation for the suppression process when  $n_0$  is the particles density in the lab frame. It is also a validity condition of the simulation procedure when  $n_0$  represents the particles density that corresponds to the number of sample particles). In order to observe the density homogenisation effect, it is desirable to view it through a transmission filter ( $\lambda_1 < \lambda < \lambda_2$ ) in a range where 3.4 and  $\lambda \approx 2r_b/\gamma_0\beta_0$  are well satisfied. In the beam frame, this corresponds to filtering a spatial frequency range ( $k_2 < k < k_1$ ), where  $k = 2\pi/\beta\gamma\lambda$ . After performing the GPT simulation we have employed in the Matlab data processing program a

spatial filtering procedure on the beam charge distribution:

$$\rho'(\vec{r}', t') = -e \sum_j \delta[\vec{r}' - \vec{r}'_j(t')] \quad (3.8)$$

in the beam frame coordinates  $\vec{r}'_j(t')$ . The data of (3.8) was obtained from the GPT code using 60K macro particles for the parameters of table 3.1. In processing the data for graphic presentation, a rectangular step-function band-pass filter in  $k$  space was employed for both positive and negative spatial frequencies in the range  $|k'_1| < |k'| < |k'_2|$ . In practice, the k-space filtering was employed by searing the point particle positions in the  $z$  dimension with a *sinc* function difference, which is the inverse Fourier transform of the rectangular frequency filter. In the transverse dimensions the point-like sample-electrons were smeared by a sinc transverse point spread function of width  $n_0'^{-1/3}$  (corresponding to low pass filtering  $|k'_x|, |k'_y| < k'_\perp = 2\pi/n_0'^{-1/3}$ ). In order to emphasis the density fluctuations, the average density was subtracted off the total density expression. Thus figure 3.7 displays the 3D density fluctuations map:

$$\begin{aligned} n'_{fil}(r', z) = 2 \sum_j \{ [k'_2 \text{sinc } k'_2(z' - z'_j) - k'_1 \text{sinc } k'_1(z' - z'_j)] \\ \times (k'_\perp \text{sinc } k'_\perp(x' - x'_j) k'_\perp \text{sinc } k'_\perp(y' - y'_j)) \} - n'_0(z) \end{aligned} \quad (3.9)$$

where  $(x'_i, y'_i, z'_i)$  are the electron locations data produced by GPT simulation at the end of the interaction region. Figure 3.7 displays a cross-section of the density map for  $y = 0$ .

This  $x' - z'$  charge distribution shown in figure 3.7 was computed for a simulation run of 60K macro particles starting with an initial random distribution of particles with initial axial velocity spread  $\Delta\beta = 0.002$ . The density distribu-

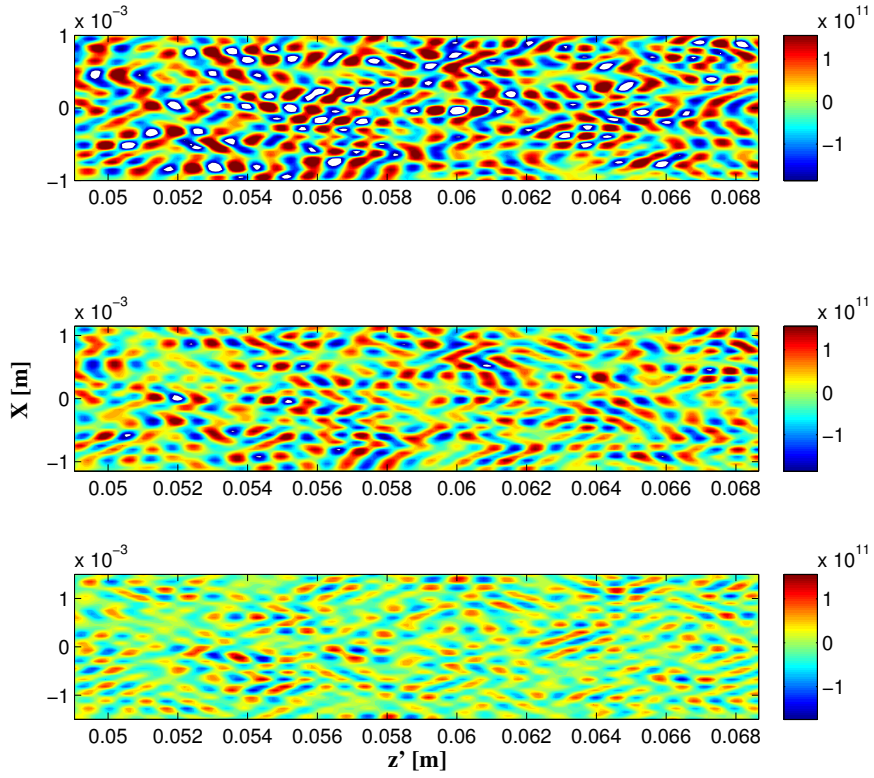


Figure 3.7: Three beam snap shots of the filtered beam  $x - z$  plane sections at different transport distances (top to bottom):  $z = 0$ ,  $z = \pi c/4\omega_{pl}$ ,  $z = \pi c/2\omega_{pl}$

tion band pass filtering was done for a laboratory frame observation wavelengths range  $5\mu m < \lambda < 10\mu m$  (which corresponds to  $1mm < \lambda' < 2mm$  in the beam rest frame). This is shown in figure 3.7 at three propagation distances using the same color scale for the three beam "snap-shots". The predicted homogenisation effect is clearly depicted.

### 3.5.1 Parseval theorem verification

For point particles the electron beam current is:

$$i(z, t) = -e \sum_{j=1}^N \delta(t - t_j(z)) \quad (3.10)$$

where the  $j$  index stands for the  $j_{th}$  electron (macro-particle in the simulations).

The spectral current of the beam (Appendix 7.1) is:

$$\check{i}(z, \omega) = \mathcal{F}\{i(z, t)\} = -e \sum_{j=1}^N \exp(i\omega t_j(z)) \quad (3.11)$$

As we pointed out in the previous section, the suppression of the spectral current (3.11) in a certain frequency range is equivalent to homogenization of the current (3.10) in the time domain (in the lab frame) or axial coordinate domain (in the beam frame).

We tested the validity of our simulation process by employing Parseval theorem, that states the equality of any signal energy computation in time and frequency domains. For a general signal  $f(t)$ :

$$\int_{-\infty}^{\infty} f(t)^2 dt = \frac{1}{2\pi} \int_{-\infty}^{\infty} |\check{F}(\omega)|^2 d\omega \quad (3.12)$$

We used the data of the sample particle positions that was simulated for the demonstration of the homogenization effect in the previous section to confirm the Parseval theorem equality by integrating  $i^2(z, t)$  over the entire pulse duration and  $|\check{i}(z, \omega)|^2$  over the filtered frequency range at different drift lengths  $z$ .

In practice, the verification was done using the simulation data in the beam frame, where the time  $t$  and frequency  $\omega$  parameters are replaced by coordinate

$z'$  and wavenumber  $k'$ . For the parameters of table 3.1 ( $\gamma = 200$ ) the band pass filtering in the range  $5\mu m < \lambda < 10\mu m$  corresponds to  $1mm < \lambda' < 2mm$  in the beam rest frame.

Note that the mathematical problem of using the current expression (3.10) in the LHS of the Parseval equality (3.12) is avoided by us using the filtered expression for the particles density (3.9).

The results of the computation of the integrated spectral current over frequencies in the filtered range, and the integrated current "energy" in the entire pulse are shown in figure 3.8. The simulation was carried out with 60K macro-particles for a drift length of 47[m].

The noise suppression factors (max/min) resulting from the two independent calculations are very similar: 4.12 in the time domain and 4.03 in the frequency domain. The minima of the suppression curves in both figures are similar as well. This calculation demonstrates well the equivalence of the noise suppression phenomenon in frequency space and the density homogenisation effect in real space.

### **3.6 Noise Suppression for the ATF Injector Parameters**

Simulation of the current noise suppression process for parameters available in ATF (Accelerator Test Facility in Brookhaven National Lab) have been conducted as preparation for experimental verification of the effect. These simulations were more advanced in several ways: use of a larger number (250K) macro-particles in a more powerful computer have allowed us to calculate noise in shorter wavelengths of 1-2 $\mu m$ , we included an initial energy spread in the e-beam as well as transverse emittance. These simulations are very close to the real beam in the

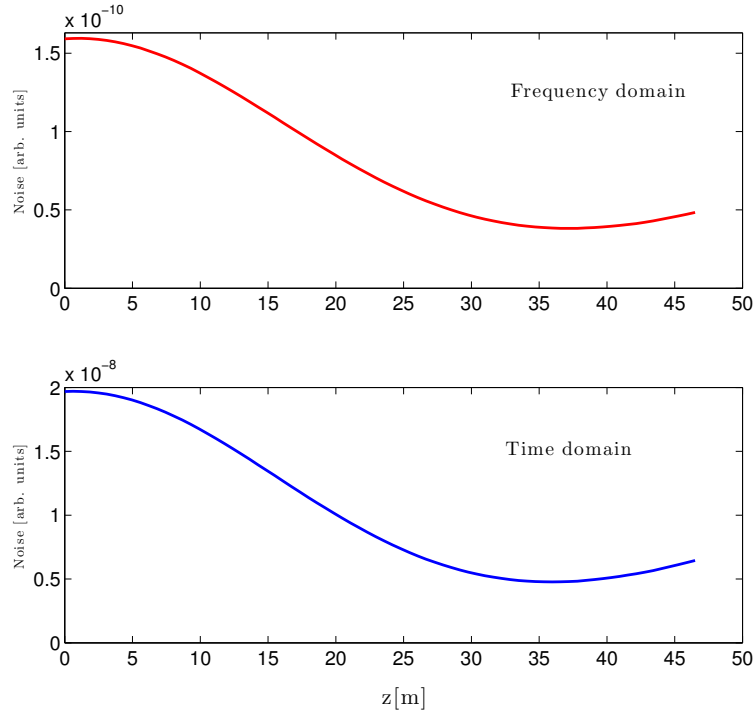


Figure 3.8: Results of noise dynamics in frequency and time domains for 60K macro-particles. Results are for 5-10 $\mu m$  modulations and show similar suppression for equal distance

ATF. Simulation results are shown in Figures 3.9 and 3.10. Figure 3.9 presents suppression results for a Gaussian transverse profile beam according to the parameters of Table 3.2. Significant noise reduction in the wavelength range 1-2 $\mu m$  is expected within a realizable drift length of less than 10m. Figure 3.10 presents the spectral noise at two locations -  $z = 0$  and  $z = \pi c/2\omega_{pl}$ . The black line represents the classical shot-noise amplitude ( $eI_b$ ) which agrees well with the computed spectral noise at  $z = 0$ .

Figure 3.11 shows the expected envelope expansion of the beam in the relevant drift section due to space charge dominated flow for the parameters used for the simulation. The beam expansion is space charge dominated (exceeding emittance dominated expansion) and small enough in comparison with the length required

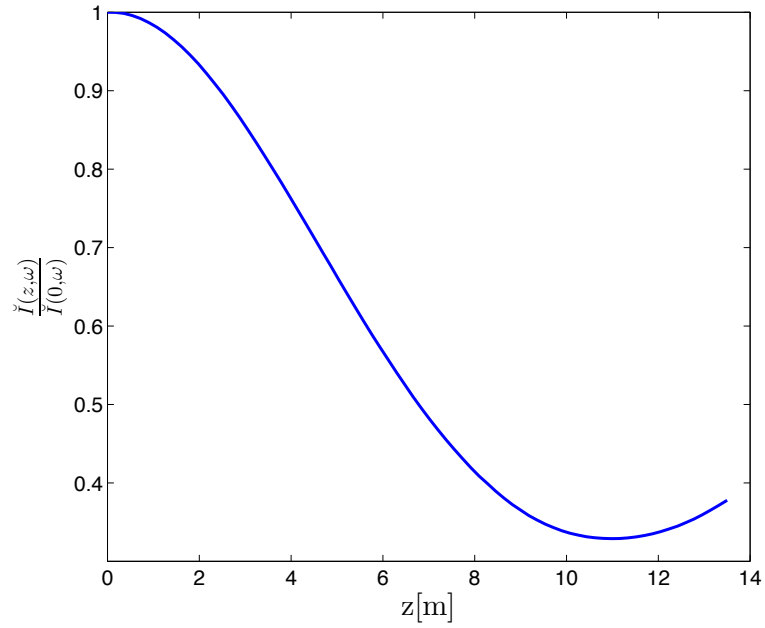


Figure 3.9: ATF simulation results - Current noise reduction at  $1\text{-}2\mu\text{m}$  for a Gaussian beam

for the interaction to take place, and for the 1-D model to be valid, so the 3-D simulation confirms quite well the prediction of the analytical model. If necessary, beam envelope expansion may be reduced also by operating quads focusing. One may be concerned that the dispersive and non-uniform field characteristics of the quads may break the simple assumptions of the 1D model. However, as shown in the next section, our simulations indicated that the noise suppression effect is not disrupted by moderate quads focusing.

These analysis and computations provided sufficient theoretical support for planning the experimental confirmation task on the ATF accelerator.

Energy	70 MeV
Transverse Density Profile	Gaussian
Pulse Charge	0.5 nC
Duration	5 pS
$\sigma$	200 $\mu\text{m}$
Transverse Norm. Emittance	2 $\mu\text{m}$
Energy Spread	5 KeV

Table 3.2: ATF Simulation Parameters

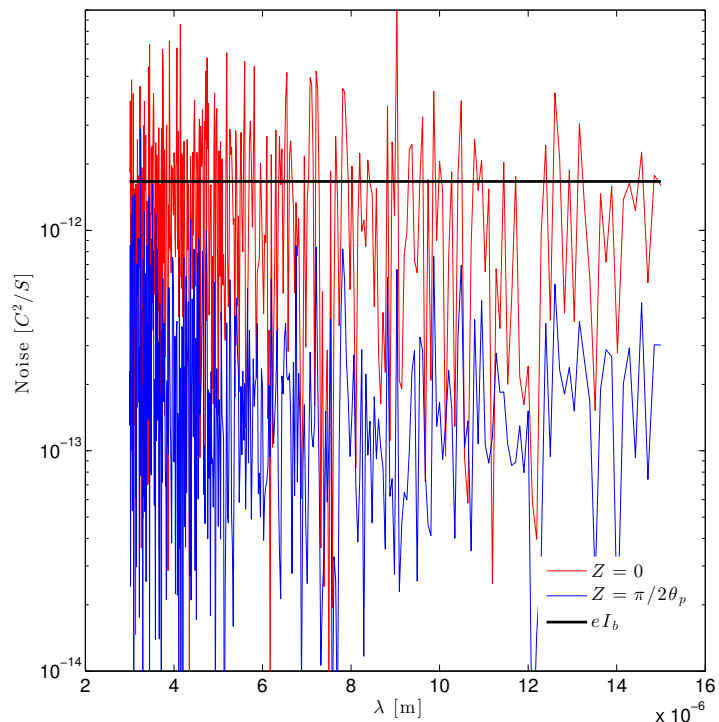


Figure 3.10: Spectral noise as a function of wavelength in a logarithmic scale according to the ATF beam parameters. The black line represents the classical shot-noise for comparison

### 3.7 Noise Dynamics of Beam Drift - LCLS Simulations

The analytical 1D model assumes a free drift. Since all injectors use quads in order to control beam transverse size, it is necessary to verify that using quadrupole

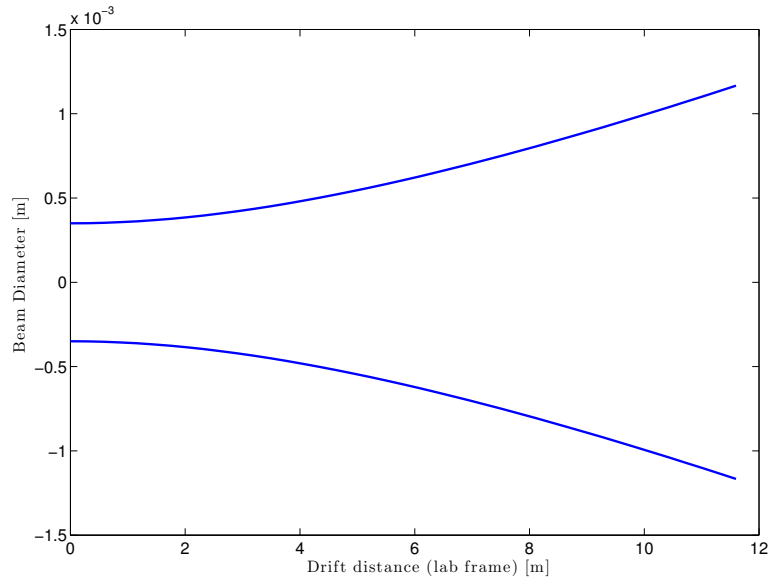


Figure 3.11: ATF beam envelope expansion

focusing does not disturb the micro-bunching dynamics. This was possible in numerical computation by indulging electron-optical components such as quads in the GPT simulations.

The modified GPT program was employed for the parameters of the injector of LCLS (table 3.3), assuming entrance beam radius of  $\sigma = 200[\mu m]$  and 3 quad triplets positioned along the drift length of 18[m] for keeping the beam envelope nearly uniform (marked as arrows in figure 3.12).

Energy	135 MeV
Transverse Density Profile	Gaussian
Pulse Charge	0.25 nC
Duration	5 pS
$\sigma$	200 $\mu m$
Transverse Norm. Emittance	<1 $\mu m$
Energy Spread	5 KeV

Table 3.3: LCLS Simulation Parameters

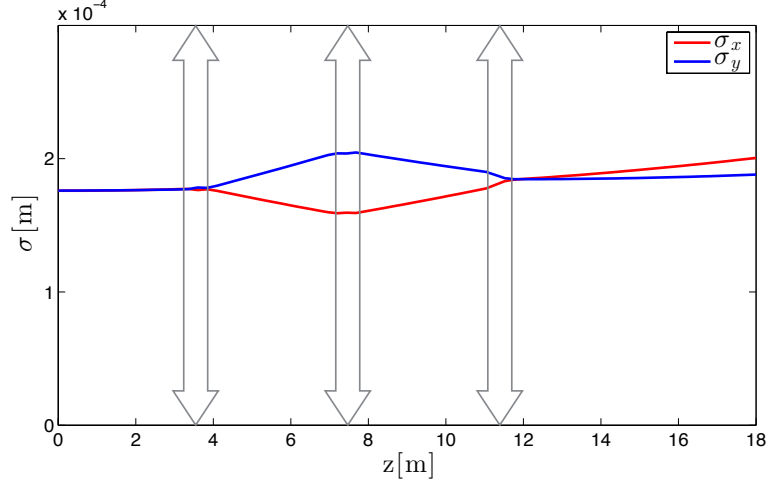


Figure 3.12: Transverse beam sizes ( $\sigma_x$ ,  $\sigma_y$ ) of the simulated beam (table 3.3) along the drift length. Three quad triplets were positioned in the arrow marked locations for keeping the beam envelope nearly uniform.

Results of the 1-D model (using the 1D model suppression tool in Appendix 7.3.3), which include the analytical calculation of the noise dynamics, as well as the validity conditions of the model [7] according to the LCLS parameters (table 3.3), are presented in figure 3.13. 3-D GPT simulation results for the same beam, using the same beam parameters as presented in table 3.3 are shown in figure 3.14. In these simulation we used 250K macro-particles and the noise was calculated for the spectral range of  $1 - 2\mu m$ .

A comparison between the 1-D model predicted results (figure 3.13) and the GPT simulation results (figure 3.14), show that moderate beam focusing using quadrupoles, does not disturb the noise suppression dynamics predicated by the 1-D model along a drift.

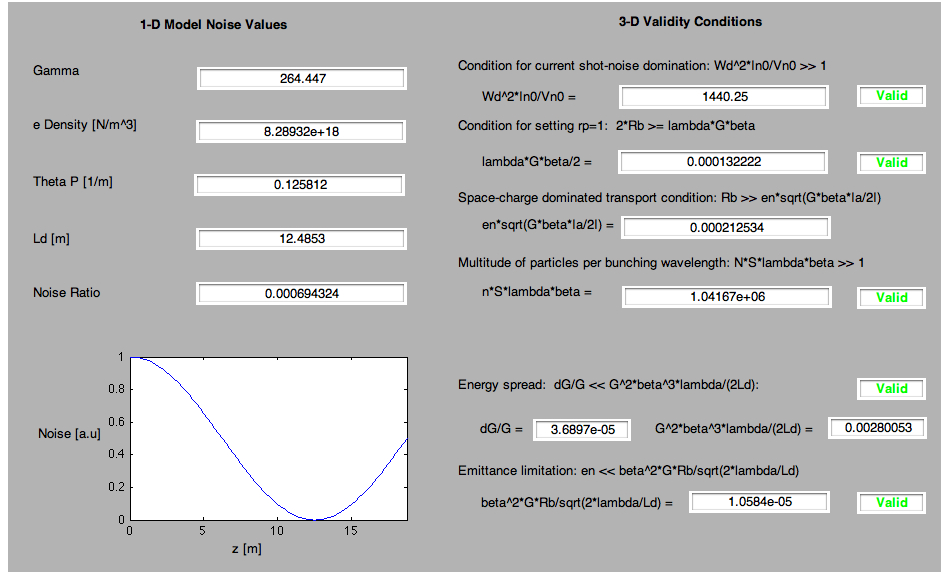


Figure 3.13: 1-D model analytical results. Results predict maximal noise suppression at  $z = 12.5[m]$ .

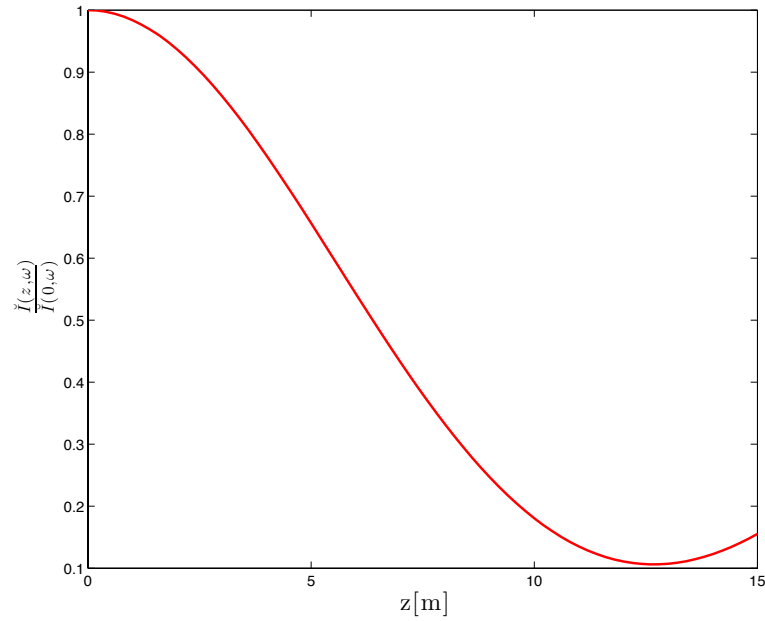


Figure 3.14: Spectral current noise for the LCLS parameters (table 3.3). Results obtained from a 250K macro-particles 3-D point-to-point space-charge interactions using GPT simulation. Noise was evaluated for the spectral range of  $1 - 2\mu m$ .

## CHAPTER 4

# Experimental Methods for Measuring Electron Beam Noise Based on Optical Transition Radiation (OTR)

Experimental measurements of current noise suppression in a relativistic charged electron beam requires evaluation of the random current modulation amplitude in a certain band of frequencies.

As no direct method is available for measuring micro-scale longitudinal density fluctuations, we rely on the effect of Transition Radiation in the Optical regime (OTR). This method is already used in accelerator facilities as beam diagnostics means for different beam properties such as size, pulse length etc [8]. OTR screens and cameras are usually already installed along the accelerators beam line, which makes it more convenient to perform such experimental measurements, since no modification of the beam line or addition of new sections is required, allowing such measurements to be relatively easy and inexpensive.

In the first part of this chapter we present the known methods and description of OTR from a single particle and using the *micro-bunching coefficient* which is commonly used to describe a pulse of many particles. A novel method, using a dyadic Green function solution approach, which takes into account the particles axial phase is presented in the second part of this chapter.

## 4.1 Optical Transition Radiation: A General Solution

The effect of transition radiation was theoretically predicted by Frank and Ginzburg in 1946 [34]. Transition radiation is a radiative emission process of basic interest on its own and as a possible practical source of radiation at a variety of different spectral regimes from THz radiation [35] to X-rays [36]. TR effect can be understood by considering the electromagnetic fields that a moving charged particle carries with it. These fields depend on the dielectric constant  $\epsilon$ . As a moving charge crosses the boundary between two different media, the fields must re-organize themselves. It is in this process of re-organization that some of the fields are "shaken off" as transition radiation.

The calculated Coulomb electrostatic field radial component in the frequency domain of an electron of velocity  $v$  that propagates perpendicularly to the screen was found to be [37]:

$$\check{E}_\rho(\rho) = \frac{q}{2\pi\epsilon_0} \frac{\omega}{c^2\gamma\beta^2} K_1 \left( \frac{\omega}{\beta c\gamma} \rho \right) \quad (4.1)$$

$$\check{H}_\phi(\rho) = \frac{q}{2\pi\epsilon_0} \frac{\omega}{c^2\gamma\beta} K_1 \left( \frac{\omega}{\beta c\gamma} \rho \right) \quad (4.2)$$

where the Fourier transform is defined by  $F\{f(t)\} = \int_{-\infty}^{\infty} f(t) \exp^{i\omega t} dt$ ,  $K_1$  is the Bessel function of the first order,  $\beta$  is the particle velocity in velocity of light units and  $\gamma$  is the Lorentz coefficient. This field was assumed to be reflected from the screen and diffracted towards an observation point in the far field.

The most general result for the case of an electron passing from medium 1 (with dielectric constant  $\epsilon_1$ ) into medium 2 (with dielectric constant  $\epsilon_2$ ) at normal incidence was presented by Ter Mikaelian [36]. The far field spectral intensity,  $\check{I}(\omega)$  of the radiation emitted in the forward direction (into medium 2),

at an angle  $\theta$  to the electron beam axis, in the frequency range  $d\omega$  and into a solid angle  $d\Omega$  is given by:

$$\frac{d^2\check{I}(\theta, \omega)}{d\omega d\Omega} = \frac{e^2\beta^2\sqrt{\epsilon_2}\sin^2\theta\cos^2\theta}{\pi^2c} \times \left| \frac{(\epsilon_1 - \epsilon_2)(1 - \beta^2\epsilon_2 - \beta\sqrt{\epsilon_1 - \epsilon_2\sin^2\theta})}{(1 - \beta^2\epsilon_2\cos^2\theta)(1 - \beta\sqrt{\epsilon_1 - \epsilon_2\sin^2\theta})(\epsilon_1\cos\theta + \sqrt{\epsilon_1\epsilon_2 - \epsilon_2^2\sin^2\theta})} \right|^2 \quad (4.3)$$

where  $\beta$  is the electron velocity in units of  $c$ ,  $e$  is the electron charge, and  $\omega$  is the frequency of the emitted radiation. In order to calculate the backward radiation, a permutation of subscripts  $1 \rightarrow 2$  and  $\beta \rightarrow -\beta$  is required.

#### 4.1.1 Relativistic OTR emission from a metallic foil

As the charge moves from the medium ( $\epsilon_1 = \epsilon$ ) into vacuum ( $\epsilon_2 = 1$ ), the radiation emitted forward is given by:

$$\frac{d^2\check{I}(\theta, \omega)}{d\omega d\Omega} = \frac{1}{4\pi\epsilon_0} \frac{e^2\beta^2}{\pi^2c} \frac{\sin^2\theta\cos^2\theta}{(1 - \beta^2\cos^2\theta)^2} \left| \frac{(\epsilon - 1)(1 - \beta^2 - \beta\sqrt{\epsilon - \sin^2\theta})}{(\epsilon\cos\theta + \sqrt{\epsilon - \sin^2\theta})(1 - \beta\sqrt{\epsilon - \sin^2\theta})} \right|^2 \quad (4.4)$$

For relativistic electrons  $\beta \rightarrow 1$ , and in the case where  $|\epsilon| > 1$  (a metallic foil) the third term in (4.4) tends to unity. Further simplification of this equation can be achieved in the small angle approximation ( $\theta \ll 1$ ,  $\sin^2\theta \approx \theta$  and  $\cos\theta \approx 1$ ) using:

$$\frac{\cos^2\theta}{(1 - \cos^2\theta)^2} = \frac{1}{(1 + \frac{1}{\cos\theta})^2(1 - \cos\theta)^2} = \frac{1}{4(1 - \cos\theta)^2} \quad (4.5)$$

which results in:

$$\frac{d^2\check{I}(\theta, \omega)}{d\omega d\Omega} = \frac{1}{4\pi\epsilon_0} \frac{e^2}{4\pi^2c} \frac{\sin^2\theta}{(1 - \beta\cos\theta)^2} \quad (4.6)$$

The small angle approximation and relativistic limit approximation ( $\beta \approx 1 =$

$1/(2\gamma^2)$ ) results in the well known angular dependence of relativistic TR from metallic foils:

$$\frac{d^2\check{I}_f(\theta, \omega)}{d\omega d\Omega} = \frac{1}{4\pi\epsilon_0} \frac{e^2}{\pi^2 c} \frac{\theta^2}{(\theta^2 + \gamma^{-2})^2} \quad (4.7)$$

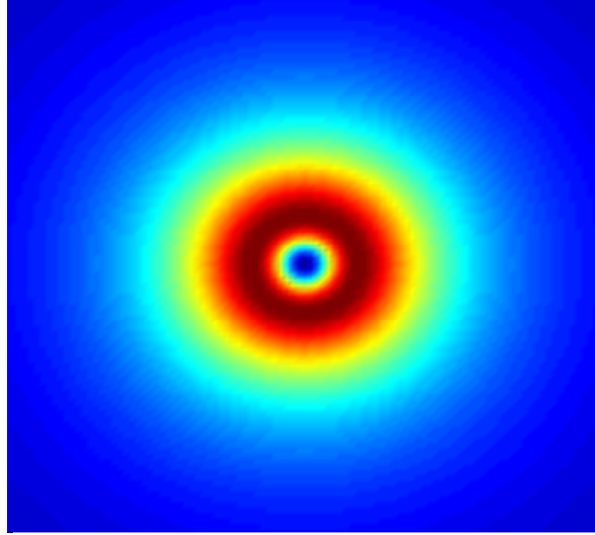


Figure 4.1: Simulated image of a single electron OTR pattern

Figure 4.1 present a simulated screen image of a single electron OTR pattern. For a relativistic electron, the "bagel shaped" far field angular radiation pattern has a peak at angle  $1/\gamma$  and a hole on axis.

For the backward radiation case (vacuum to medium) of normal incidence TR, the process is similar except for changing  $\epsilon_1 = 1$ ,  $\epsilon_2 = \epsilon$  in equation (4.4). One finds out that for a metallic foil, where  $|\epsilon| \gg 1$ , the forward and backward emission intensities into vacuum are the same, given by equation (4.7).

### 4.1.2 Integrated emitted OTR power from a metallic foil

The integration of equation (4.7) over  $\theta$  in the angular interval ( $0 - \theta_{max} \gg \gamma^{-1}$ ) gives the energy dependence of the spectral intensity (that turns out to be frequency independent in the far field):

$$\frac{dI}{d\omega} = \frac{1}{4\pi\epsilon_0} \frac{e^2}{\pi c} [2 \ln(\gamma\theta_{max}) - 1] \quad (4.8)$$

$\theta_{max}$  is defined by the aperture angle of the radiation measuring device. The equation is valid for  $\theta \ll 1$ ,  $\gamma \gg 1$ . The intensity of the TR has a logarithmic dependence on the energy. The number of photons, generated in the frequency interval  $(\omega_1, \omega_2)$  from a single electron incident on a metal foil, is obtained by dividing equation (4.8) by  $\hbar\omega$  and integrating over  $\omega$ :

$$N = \frac{\alpha}{\pi} [2 \ln(\gamma\theta_{max}) - 1] \ln\left(\frac{\omega_2}{\omega_1}\right) \quad (4.9)$$

where  $\alpha = \frac{1}{4\pi\epsilon_0} \frac{e^2}{\hbar c}$  is the Fine-structure constant in *SI* units. For the total yield of a single pulse we simply multiply this result with the number of electrons per pulse ( $N_e$ ).

## 4.2 Spatial Coherence of OTR from an Electron Beam

### 4.2.1 Far field OTR pattern from a phase correlated electron beam

The radiation field of the OTR emission from an electron beam in some measurement plane, in the far-field, is the result of the interference of the coherent radiation fields from all the electrons in the beam. If the electrons incidence times on the OTR screen are random, the radiation wave-packets arrive to the measure-

ment device with random phase, and will sum up in energy only. However, the electrons arrival times may be correlated, either by coherent current modulation or maybe the partially coherent process of noise suppression described in chapter 2. In either case, one must sum up the complex radiation field amplitudes of the field contributions of the electrons and find out the local radiation intensity distribution from the absolute value squared of the interfering fields. This would result on the observation plane a radiation intensity that is different from the OTR pattern of a random beam, both in spatial distribution and in integrated intensity. In the case of partially coherent modulation it was found to produce a speckled pattern [24].

We present here the coherent and partially coherent far-field OTR pattern phenomenon for both the coherent current modulation case and the case of partially coherent modulation due to electrons correlation after collective micro dynamic process in drift (simulated using GPT).

Using standard Fraunhofer diffraction formulation [38], we derive in appendix 7.2 a general expression for the far-field diffraction spectral intensity from an ensemble of electrons incident on a screen at  $z = 0$  at arbitrary positions  $(x_i, y_i)$  and times  $(t_{0j})$  ( $j = 1 \dots N$ ). The OTR spectral intensity distribution from a coherent or partially coherent micro-bunched electron beam is found to be:

$$\frac{d^2 \check{I}}{d\Omega d\omega} = \frac{d^2 I_e}{d\Omega d\omega} N^2 |M_b(\theta_x, \theta_y, \omega)|^2 \quad (4.10)$$

where

$$\frac{d^2 I_e(\theta, \omega)}{d\omega d\Omega} = \frac{e^2}{\pi^2 c} \frac{\theta_x^2 + \theta_y^2}{(\theta_x^2 + \theta_y^2 + \gamma^{-2})^2} \quad (4.11)$$

is the OTR spectral power distribution from a single electron,  $N$  is the number

of electrons in the bunch and

$$M_b(\theta_x, \theta_y, \omega) = \frac{1}{N} \sum_{j=1}^N \exp[-ik(\sin \theta_x x_{0j} + \sin \theta_y y_{0j} + z_{0j}/\beta)] \quad (4.12)$$

Is a bunching factor, where  $k = \omega/c$ .

This expression is identical with the commonly used expression [39] when  $\beta = 1$ . Note that this expression relates to our expression for the longitudinal current noise (3.1):

$$|M_b(\theta_x, \theta_y, \omega)|^2 = \frac{1}{N^2} \left| \sum_{j=1}^N \exp^{-i\omega t_{0j}(z)} \right|^2 = \frac{\check{i}(\omega, z)|^2}{e^2 N^2} = \frac{\check{i}(\omega, z)|^2}{N |\check{i}(\omega)|_{shot}^2} \quad (4.13)$$

In order to calculate the total radiant energy measured in a frequency range  $\omega_1 < \omega < \omega_2$  in all angles we integrate over angles and frequencies:

$$W(\omega_1 < \omega < \omega_2) = N^2 \int_{-\infty}^{\infty} \int_{\omega_1}^{\omega_2} \frac{dI_e(\theta_x, \theta_y, \omega)}{d\Omega d\omega} |M_b(\theta_x, \theta_y, \omega)|^2 d\theta_x d\theta_y d\omega \quad (4.14)$$

If we are interested in examination of simulation results, integrals should be presented in terms of sums. The formula to calculate the OTR angular distribution and intensity in a certain frequency band according to the particles incidence transverse locations and times is therefore (using small angles approximation):

$$I_{OTR}(l, p) = \frac{e^2}{\pi^2 c} N_e^2 \sum_q \frac{\theta_l^2 + \theta_p^2}{(\theta_l^2 + \theta_p^2 + \gamma^{-2})^2} \left| \sum_j \exp[-ik_q(\sin \theta_l x_j + \sin \theta_p y_j + z_j/\beta)] \right|^2 \quad (4.15)$$

where  $q = [k_{min} : k_{max}]$ ,  $l = [-\theta_{xmax}/2 : \theta_{xmax}/2]$ ,  $p = [-\theta_{ymax}/2 : \theta_{ymax}/2]$ ,  $j = [1 : N]$ ,  $N$  is the number of macro particles and  $N_e$  is the number of electrons in the simulated macro-particle.

Equation (4.15) can be used for calculating either OTR or COTR radiation patterns in the far field zone. In the first case one inserts  $x_j, y_j, z_j(t_j)$  as random variables. In the second case  $z_j(t_j)$  are determined externally (coherent modulation at a given frequency). The effect of COTR from a correlated electron beam in the collective interaction process (chapter 2) can be computed (only in the far field zone) using equation (4.15) using the particle incidence coordinates  $(x_j, y_j, z_j(t_j))$  from the GPT simulation. Such a computation is presented later on (section 4.4.2).

#### 4.2.2 Coherent external modulation and the spatial pattern of the micro-bunching coefficient

Before embarking on exact OTR computation of an electron beam with random (or coherent) modulation, I examine in this section the angular pattern of the bunching parameter  $M_b(\theta_x, \theta_y, \omega)$  (4.13) for a model electron beam current distribution that is composed of coherently modulated electrons of frequency  $\omega$  and randomly distributed electrons in different proportions or modulation amplitude, that is defined as the portion of macro-particles in the periodic bunches out of the total number of particles used in the pulse. A 25% modulated beam, for example, means that 75% of the particles are randomly distributed along the pulse and 25% are modulated periodically at a certain wavelength (see figure 4.2).

Figure 4.3 displays the spatial (or angular) pattern of the micro bunching parameter  $|M_b(\theta_x, \theta_y, \omega)|^2$  (equation (4.12)) for a perfect coherent modulation at wavelength of  $\lambda_b = 5\mu m$ ,  $\beta \approx 1$ ,  $\sigma = 300\mu m$  and various modulation ratios (100%, 75%, 50%, 25%, 1% and 0%). The micro bunches of the modulated sample particles are modeled as zero width disks of equal number. The calculation was carried out for the LCLS parameters (see table 4.1). The number of sample-

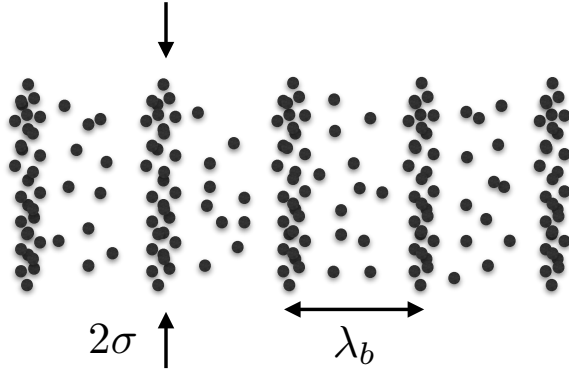


Figure 4.2: Partially modulated electron beam current distribution.

particles is 100K, corresponding to 330 particles per period. The transverse coordinates of all particles and the longitudinal coordinates of the particles in the unmodulated part were determined by a random number generator.

Note that the angular pattern of the bunching parameter  $M_b(\theta_x, \theta_y, \omega)$  displayed in figure 4.3 is not the radiation pattern. The OTR far field radiation pattern of the beam (4.10) includes a factor of the single electron radiation pattern (4.11) which is null on-axis. Therefore the OTR pattern of a zero-emittance electron beam would be the product of the patterns of figure 4.3 and the single electron OTR pattern, and is null on-axis.

For modulation ratios larger than  $1/\sqrt{N}$  (figures 4.3a-d) the angular pattern of the bunching parameter is dominated by the coherent modulation. The angular pattern is proportional to the Fourier transform of the disks and its angular width is  $\sim \lambda_b/\sigma$ , which corresponds to the diffraction angle of the radiation that it would emit. The angular pattern stays the same in figures 4.3a-d but the amplitude (presented in a colour-code) changes in proportion to the square of the modulation ratio. Figure 4.3f shows the wide spatial distribution low intensity of  $|M_b|^2$  for a random beam (0 % modulation), Figure 4.3e shows the spatial distribution when the coherent modulation ratio is of the order of the random modulation.

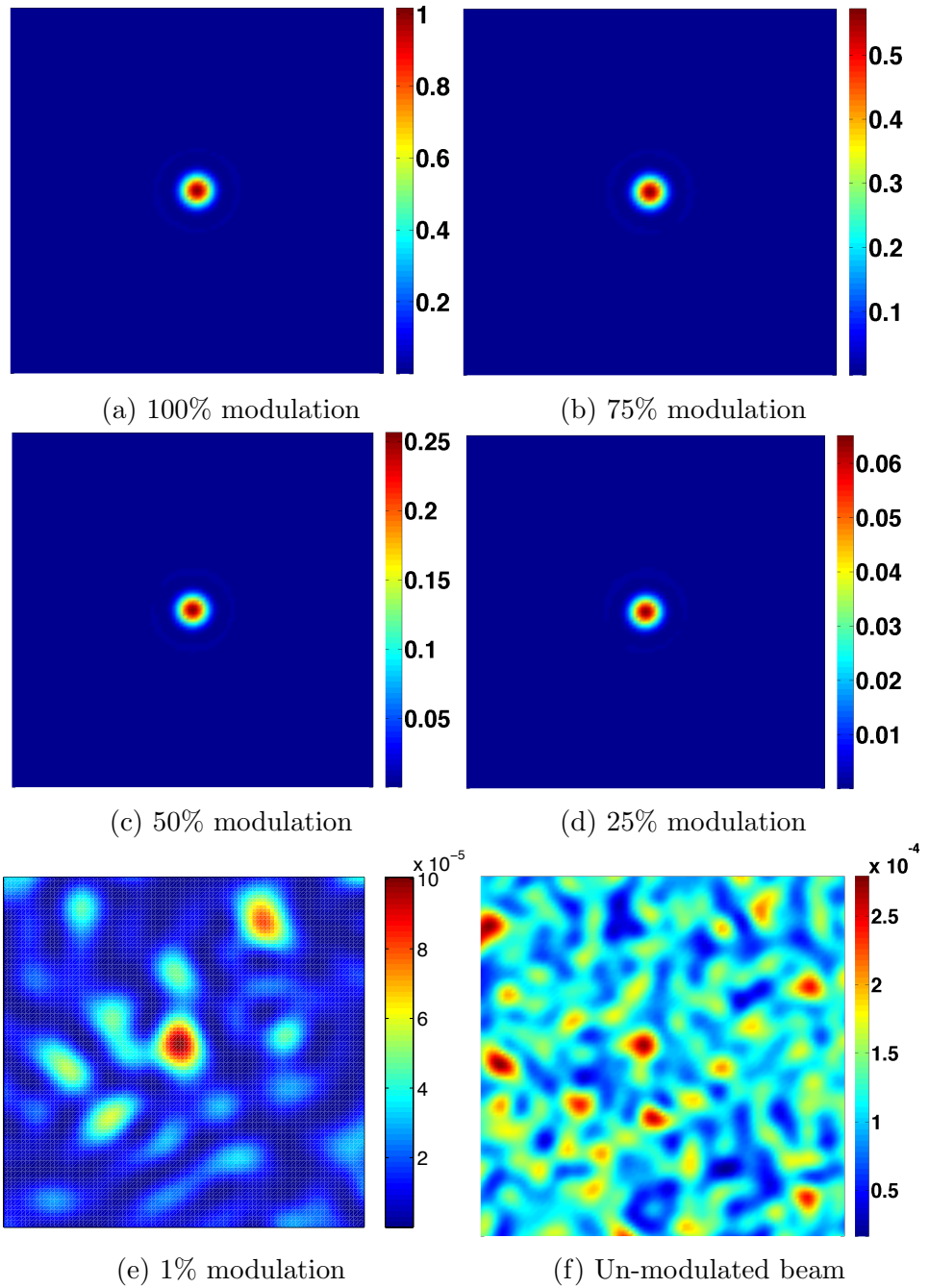


Figure 4.3: Micro-bunching coefficient for different beams of different modulation levels: 100%, 75%, 50%, 25%, 1% and un-modulated beams using 100K macro particles. Plots show significant difference in the maximal amplitude for the different modulation rates.

Energy	63 MeV
Transverse Density Profile	Flat
Pulse Charge	0.25 nC
Duration	5 pS
$\sigma$	300 $\mu m$
Transverse Norm. Emittance	<1 $\mu m$
Energy Spread	5 KeV

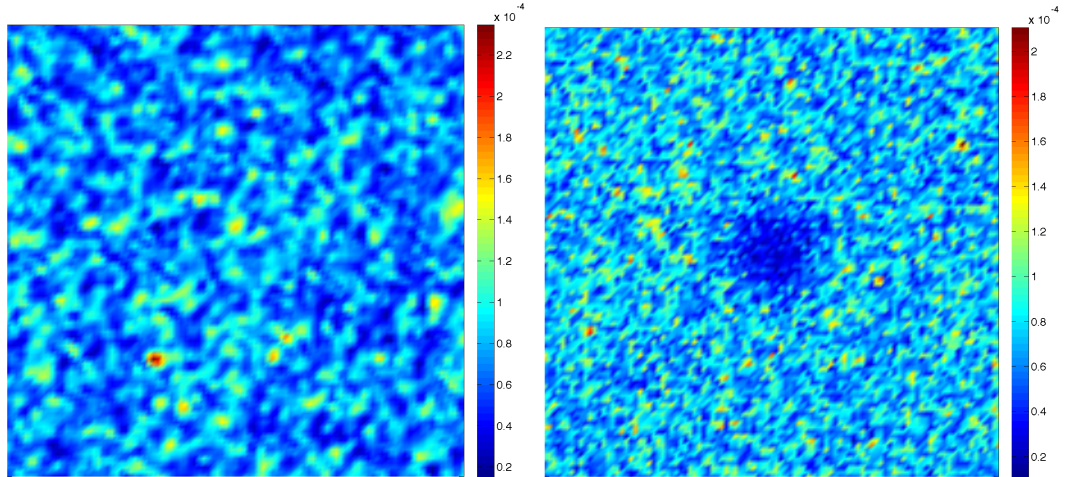
Table 4.1: LCLS OTR simulation parameters

### 4.2.3 The spatial pattern of the micro-bunching coefficient for a correlated e-beam after a collective interaction section

In order to demonstrate the suppression effect of radiation in the forward direction due to collective interaction, we compute in this section the spatial distribution of the modulation factor  $|M_b(\theta_x, \theta_y, \omega)|^2$  (4.12) using the output parameters of GPT simulations for the LCLS parameters as input particle coordinates. Note that the bunching coefficient is not yet the OTR pattern which is given in the far-field by the product of the bunching parameter pattern and the single electron OTR pattern (4.15).

We draw in figure 4.4 the computed spatial pattern of  $|M_b(\theta_x, \theta_y, \omega)|^2$  computed from the output of GPT simulation of collective interaction based on SLAC's LCLS beam parameters. The simulation was performed using 250K macro-particles. The computed modulation parameter squared was integrated in the wavelengths range of 2.5-5 $\mu m$  with 0.5 $\mu m$  intervals. (in this range the simulations shows clear reduction of the longitudinal current noise (3.1) at the appropriate distance  $L_{\pi/2} = 12m$ ). The angles run from -0.0325 mrad to 0.0325 mrad in  $x - y$  plane, with a  $100 \times 100$  mesh angular resolution. The beam simulated parameters are summarised in table 4.1.

The output of the GPT simulation was examined at  $L_d = 0$  and  $L_d = 12$  m in which minimal current noise is predicted by both the 1D model and the numerical simulations. This output of GPT presented the positions of the macro-particles in the beam frame. A Lorentz transformation was used to compute the particle positions in the laboratory frame to be used in equation (4.12).



(a) Bunching factor as a function of  $\theta_x$  and  $\theta_y$ , at  $L_d = 0$  (b) Bunching factor as a function of  $\theta_x$  and  $\theta_y$ , after a quarter plasma oscillation

Figure 4.4: Pattern of the absolute value squared of the bunching factor as a function of  $\theta_x$  and  $\theta_y$ , demonstrate reduction in the micro-bunching coefficient.

Figures 4.4a and 4.4b display the absolute value squared of the micro-bunching coefficient pattern of the beam at  $L_d = 0$  (4.4a) and at  $L_d = \pi c/2\omega_{pl} = 12m$  (4.4b). It is seen in figure 4.4b that there is a significant reduction in the micro-bunching coefficient over a wide circle of coherence in the center of the electron beam.

### 4.3 Optical Transition Radiation - Exact Solution in the Near and Far Field Employing a Dyadic Green Function

Transition radiation (TR) is the electromagnetic radiation emitted by a charged particle when it hits a conducting or dielectric plate or foil. The wide frequency band radiation emitted on both sides of the foil originates from the Fourier components of the terminated (or correspondingly suddenly appearing) current of the charged particle in either side of the foil, as well as from the currents induced on the foil by the charge particle (see figure 4.5).

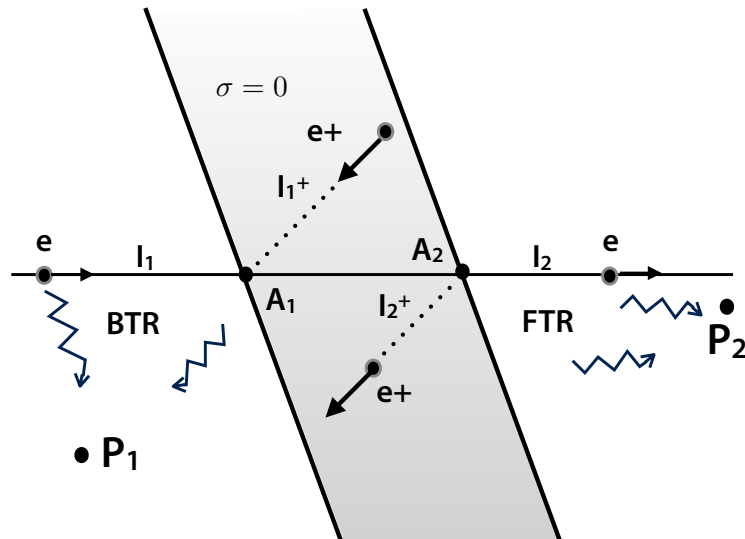


Figure 4.5: The schemes of backward transition radiation (BTR) and forward transition radiation (FTR) for a perfect conductor foil screen and their equivalent image charge representation

Based on this model the *far field* energy per unit frequency per solid angle (spectral radiant intensity) emitted from a single charge hitting a perfect conductor at normal incidence is [36]:

$$\frac{dU_e}{d\Omega d\omega} = \frac{1}{4\pi\epsilon_0} \frac{e^2\beta^2}{\pi^2 c} \frac{\sin^2\theta}{(1 - \beta^2 \cos^2\theta)^2} \quad (4.16)$$

This expression is usually used to calculate the TR emission energy distribution pattern in the far-field of a charged particle beam by convoluting it with the spatial and angular distribution function of the electron beam.

Expression (4.16) is not sufficient if one needs to find the TR field of a beam in the near field (near the screen position) or its optical image, and because it does not contain phase information, it is not useful for calculating the emission from a beam of phase correlated electrons (COTR) [8] [4]. In this case, an exact diffraction integral expression is required, including the radiation field phase. Shkvarunets and Fiorito [40] presented a more complete vector diffraction model based on Love's field equivalence theorem, but it was not employed for calculation of near field diffraction. Geloni et al developed related derivation of synchrotron and edge radiation near field analysis [41].

We present an exact vector field diffraction theory of TR from a single electron, based on dyadic Green function formulation [42]. The source of the diffraction integral is the current of the electron itself and its image charge. Since the complex field solution is exact at any distance, it reproduces on one hand the source Coulomb field of the electron on the screen (4.1) and on the other hand exactly describes the radiation field in all optical diffraction regimes, including the "reactive near field", the Fresnel near field zone and the Fraunhofer far field zone. It can be then employed to calculate coherent and partially coherent TR radiation from temporally or spatial correlated electrons in an electron beam.

Optical Transition Radiation (OTR) is used extensively as diagnostics of the charge distribution across the cross-section of electron beams [43] and pulse duration [44]. In the application of OTR screens as e-beam profile diagnostics the

screen is viewed by a camera focused to produce an image of the OTR screen on the camera sensor's screen. Assuming that there is no phase correlation between the radiation wave-packets emitted by the electrons which hit the OTR screen at different locations (namely the electrons hit the screen at random), the light density distribution on the camera image plane replicates the incident electron current distribution on the OTR screen. The e-beam profile image resolution is then limited only by the Modulation Transfer Function (MTF) of the camera. Thus in this application there is no need to know the coherent field (amplitude and phase) of the radiation wave-packets emitted by the individual electrons.

Recently, coherence effects were observed in the measurement from OTR screens (COTR) [8]. The coherence effects came into expression as speckled images on the camera imaging plane and the integrated OTR power was not proportional to the e-beam current. The coherence effects that were described originally as "unexplained physics" [4] are now understood to be the result of correlation of the electrons arrival time due to a Coulomb collective micro-dynamic process in the e-beam transport line preceding the OTR screen [7]. Evidently, in order to interpret the imaged COTR radiation pattern at the camera sensors plane, one needs to know the coherent radiation field in the "near field" of the OTR screen and the Optical Transfer Function (OTF) of the camera's optical system. The radiation field on the screen is the result of coherent interference of the radiation fields of the electrons in the beam. Therefore, besides knowledge of the incidence phase of the electrons on the OTR screen, a necessary condition for composing the OTR screen coherent near field radiation pattern is an exact complex field expression of the OTR emission from an individual electron. The derivation of such an exact expression, valid in all near and far field regimes, is the goal of this section.

### 4.3.1 Radiative emission from a general line source

Diffraction theory has been developed primarily for analysis of radiation from a surface source. For the analysis of TR we need electromagnetic diffraction theory from a line source. In the following two sections we present a general formulation for diffraction from a longitudinal current line source of arbitrary distribution:

$$\check{\mathbf{J}}(\underline{r}') = \hat{e}_z I(z') \delta(x') \delta(y') \quad (4.17)$$

as shown in figure 4.6.

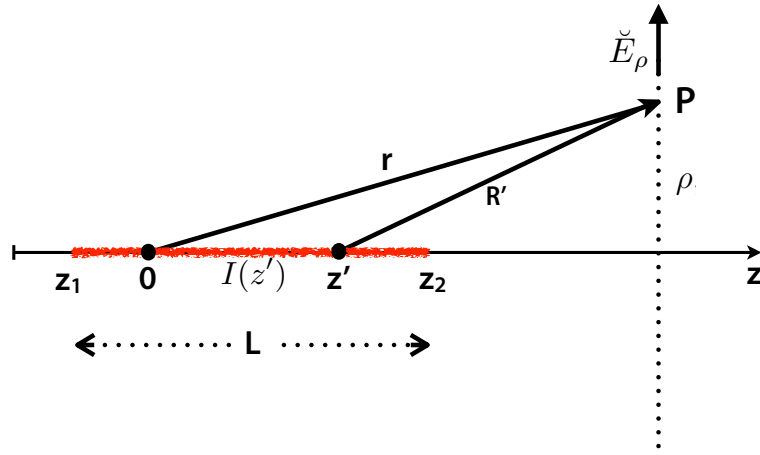


Figure 4.6: Geometry of radiation diffraction from a current line source

The electric field created by a current density  $\check{\mathbf{J}}(\mathbf{r})$  in frequency domain can be calculated as

$$\check{\mathbf{E}} = -i\omega\mu \int G_e(\mathbf{r}, \mathbf{r}') \check{\mathbf{J}}(\mathbf{r}') d^3\mathbf{r}' \quad (4.18)$$

where  $G_e(\mathbf{r}, \mathbf{r}')$  is the Maxwell equation free-space dyadic Green function [42]:

$$G_e(\mathbf{r}, \mathbf{r}') = \left( \mathbf{I} + \frac{\nabla\nabla}{k^2} \right) \frac{e^{ik|\mathbf{r}-\mathbf{r}'|}}{4\pi|\mathbf{r}-\mathbf{r}'|} \quad (4.19)$$

where  $\mathbf{r}$  and  $\mathbf{r}'$  are respectively the source and observation points coordinates (see figure 4.6). We employ equations (4.18) and (4.19) for a line source (4.17), and define  $R' = \sqrt{\rho^2 + (z - z')^2}$ , where  $\rho$  is the cylindrical coordinates radial component of the observation point  $P$  (see figure 4.6). The radiation field has transverse and axial components  $\check{\mathbf{E}} = \check{E}_z \hat{e}_z + \check{E}_\rho \hat{e}_\rho$ . We are interested in the transverse electric field component. In this case, one can express the radially symmetric field in terms of the longitudinal to transverse field component of the dyadic Green function  $G_\rho(\rho, z, z')$ :

$$\check{\mathbf{E}}_\rho(\rho, z) = -i\omega\mu \int \check{I}(z') G_\rho(\rho, z, z') dz' \quad (4.20)$$

where from (4.19) the longitudinal - transverse Green function is:

$$G_\rho = \frac{1}{k^2} \frac{\partial}{\partial \rho} \frac{\partial}{\partial z} \left( \frac{e^{ikR'}}{4\pi R'} \right) \quad (4.21)$$

or explicitly:

$$G_\rho = -\rho(z - z') \frac{e^{ikR'}}{4\pi R'^3} \left[ 1 + \frac{3i}{kR'} - \frac{3}{(kR')^2} \right] \quad (4.22)$$

The measurable optical parameter is usually the spectral power density. The expression for the spectral power density is derived from the Parseval theorem in the frequency range  $0 < \omega < \infty$ :

$$\int_{-\infty}^{\infty} \underline{S}(t) dt = \int_{-\infty}^{\infty} \underline{E}(t) \times \underline{H}(t) dt = \frac{1}{\pi} \int_0^{\infty} \text{Re} \left( \check{\underline{E}}(\omega) \times \check{\underline{H}}^*(\omega) \right) d\omega = \int_0^{\infty} \underline{S}(\omega) d\omega \quad (4.23)$$

For a line source (which has cylindrical symmetry), the axial spectral power

density is:

$$S_z(\omega) = \frac{1}{\pi} \check{E}_\rho(\omega) \check{H}_\phi^*(\omega) \quad (4.24)$$

In the far-field only, in the paraxial approximation we may define the spectral radiant intensity as:

$$\frac{dU_e}{d\Omega d\omega} = \frac{z^2}{\pi} \sqrt{\frac{\epsilon_0}{\mu_0}} |\check{E}_\rho(\omega)|^2 \quad (4.25)$$

where  $z$  is the coordinate of the observation plane.

### 4.3.2 The diffraction zones of a line source

Equations (4.20) and (4.22) constitute an exact diffraction integral formulation for a longitudinal current line source of any current distribution. As in diffraction theory from a planar source, it is possible to define also for a line source approximate diffraction integrals and diffraction zones analogous to the inductive near-field zone, the Fresnel near-field zone and the Fraunhofer far-field zone of a planar source.

In most practical cases we are interested in the field in a range longer than a wavelength:

$$kr = 2\pi r/\lambda \gg 1 \quad (4.26)$$

In this range the Green function (4.22) can be replaced by:

$$G_\rho = -\rho(z - z') \frac{e^{ikR}}{4\pi R^3} \quad (4.27)$$

We can further approximate (4.27) by employing series expansion of  $R$  in

terms of  $\frac{z'}{r}$  where (see figure 4.6):

$$R' = [(z - z')^2 + \rho^2]^{\frac{1}{2}} = [z^2 - 2zz' + z'^2 + \rho^2]^{\frac{1}{2}} = r[1 - 2\frac{zz'}{r^2} + \frac{z'^2}{r^2}]^{\frac{1}{2}} \quad (4.28)$$

where we defined  $r = \sqrt{(z^2 + \rho^2)}$  - the distance of the observation point from the coordinates origin. The expression in terms of  $\frac{z'}{r}$  is analogous to the expansion in terms of the source transverse coordinates in the case of diffraction from a planar source.

### 4.3.3 Longitudinal quadratic-phase "Fresnel" near zone limit

Defining  $\cos \theta = \frac{z}{r}$ , second order Taylor expansion results in:

$$R' \simeq r[1 - \frac{z'}{r} \cos \theta + \frac{1}{2} \frac{z'^2}{r^2} \sin^2 \theta] \quad (4.29)$$

This result is now substituted into the Green function phase. In the denominator we substitute only the zero order  $R' \simeq r$ . This results in the longitudinal-to-transverse Green function expression in a quadratic-phase paraxial approximation zone (analogous to the convention of Fresnel zone in the case of a transverse current source):

$$G_\rho = -\sin \theta \cos \theta \frac{e^{ikr}}{4\pi r} e^{-ik_z z' + ik \sin^2 \theta \frac{z'^2}{2r}} \quad (4.30)$$

where  $k_z = k \cos \theta$ .

Substituting (4.30) in (4.20) the longitudinal line current "Fresnel" integral is:

$$\check{E}_\rho = \frac{i\omega\mu}{4\pi} \frac{e^{ikr}}{r^3} \rho \int_{z_1}^{z_2} \check{I}(z') e^{-ik(\cos \theta z' + \sin^2 \theta \frac{z'^2}{2r})} (z - z') dz' \quad (4.31)$$

For a general sinusoidal current distribution  $\check{I}(z) \propto e^{ik_0 z}$  this integral can

be expressed in terms of the traditional Fresnel integrals  $c(x) = \int_0^x \cos(t^2)dt$ ,  $s(x) = \int_0^x \sin(t^2)dt$ .

The validity range of the "Fresnel" quadratic phase approximation is determined by the requirement that the contribution of the third order expansion of (4.27) to the Green function phase is much smaller than  $\pi$ . On the other hand, when also the quadratic phase term in (4.31) is much smaller than  $\pi$ , it can also be dropped, and the "Fresnel" near field approximation turns into the "Fraunhofer" far field approximation.

Using  $|z'| < L$ , the "Fresnel" near field zone of the longitudinal line current is defined in the range:

$$\left(\frac{L^3 \rho^2 z}{8\pi\lambda}\right)^{1/5} \ll r \ll \left(\frac{\rho^2 L}{\lambda}\right)^{1/3} \quad (4.32)$$

Note that in the derivation of (4.30) and (4.31) we did not need to resort to the paraxial approximation  $\rho \ll z$ . In the paraxial approximation  $r \approx z$  and the LHS of (4.32) is replaced by  $(L^2 \rho^2 / 8\pi\lambda)^{1/4}$ . Also note that in the near diffraction zone, contrary to the far zone, the parameters  $r$ ,  $\sin \theta = \rho/r$ ,  $\cos \theta = z/r$  are not uniquely defined, and depend on the choice of origin  $z' = 0$  of the line source function (see figure 4.6). Therefore, the radiation pattern  $\check{E}_\rho(\omega, z, \rho)$  may seem somewhat different for different choice of origin.

#### 4.3.4 Longitudinal "Fraunhofer" far zone limit

In the Fraunhofer far zone limit, the quadratic term of the phase is negligible. In analogy to the planar source case, the far zone of a line source is defined by the requirement that the quadratic term in the exponent of (4.30) is negligible,

resulting:

$$z \cong r \gg \left( \frac{\rho^2 L^2}{\lambda} \right)^{1/3} \quad (4.33)$$

where  $L$  is the length of the radiation line-source.

The longitudinal-transverse Green function in the Fraunhofer limit is then:

$$G_\rho = -\sin \theta \cos \theta \frac{e^{ikr}}{4\pi r} e^{-ik_z z'} \quad (4.34)$$

The line source far-field diffraction integral is then:

$$\check{E}_\rho = \frac{i\omega\mu}{4\pi} \frac{e^{ikr}}{r} \sin \theta \cos \theta \int_{z_1}^{z_2} \check{I}(z') e^{-ik_z z'} dz' \quad (4.35)$$

#### 4.3.5 Ginzburg's formation zone

The derivation so far is general for any longitudinal current line-source. We now specify to the case of OTR emission from an electron incident on a conducting screen.

Radiation from a free electron is always formed in a finite region and not in a point. This region is considered the "formation zone" according to Ginzburg [45]. The formation zone size is dependent on the emission wavelength  $\lambda$ . Its size is termed the "formation length" -  $L_f$ . The formation length is essentially the length of traversal in free space of a charged particle, such that the radiation emitted by it at wavelength  $\lambda$  accumulates a phase increment of  $2\pi$  at the observation point.

Ginzburg's formation length for a relativistic particle is [45]:

$$L_f = (1 + \beta)\gamma^2 \lambda \approx 2\gamma^2 \lambda \quad (4.36)$$

The diffraction formula integration is supposed to be carried out in the ideal

case from  $-\infty$  to 0 or from 0 to  $\infty$ . In practice, the radiation emission from the electrons well before the formation zone ( $L > L_f$ ) is negligible. This consideration provides a practical range for performing the numerical integration of the diffraction integral. We will investigate this consideration using the exact solution for different lengths in units of the formation length in order to verify the convergence of our solution.

### 4.3.6 Transition radiation model

Let us consider now the case of transition radiation emission from a perfect conductor foil screen set at arbitrary angle relative to the electron propagation direction as shown in figure 4.5. An observer at  $P_1$  in the half space before the foil would sense the non radiative Coulomb fields of the electron (both electric and magnetic - due to the electron velocity [37]) only if it is positioned very close (distance  $\sim \gamma\lambda/2\pi$ ) to the electron trajectory. However, because the electron charge vanishes upon incidence on the screen, as it seems in the back half space, the abrupt temporal change in the electron current  $I_1$  means that its Fourier spectrum contains a very wide band of frequencies, and these current spectral components radiate in free space, and would be sensed by observer  $P_1$  at any finite distance.

In addition, the electron charge induces positive surface currents on the conductor screen, that also change in time as the electron approaches the screen, and vanish almost instantaneously (at the dielectric relaxation time of the conductor) when the electron is incident on the screen. Also these time varying surface currents radiate in a wide frequency band, and their radiation would be sensed at point  $P_1$  as well.

Using the method of equivalent charge images [42], we assert that the induced

current on the infinite conductor screen radiates into the half space exactly like an imaginary point particle of charge  $+e$  that propagates along the trajectory of the mirror image (relative to the screen surface) of the electron  $e$  (current  $I_1^+$  in figure 4.5). This current terminates exactly at the same time of the electron's incidence on the screen. The combined radiation fields from both sources is the Backward Transition Radiation (BTR).

A similar physical process takes place in the forward half space of the screen, if it is made of a thin foil, through which the electron emerges into the forward half space abruptly. The Forward Transition Radiation (FTR) observed at point  $P_2$  in this half space is the same as generated in an equivalent picture of electron current  $I_2$  and a positive image charge current  $I_2^+$ , both appear to be generated abruptly in time in the forward half space (see figure 4.5).

Taking the charge propagation direction to be along coordinate  $z$ , and arbitrarily choosing the coordinate origin  $z = 0$  at the particle intersection point with the conductor surface ( $A_1$  or  $A_2$ ), the current densities corresponding to currents  $I_1, I_1^+, I_2, I_2^+$  are:

$$\mathbf{J}_1(\mathbf{r}, t) = -e\delta(x - x_0)\delta(y - y_0)\delta(z - v(t - t_0))[1 - \eta(t - t_0)] \quad (4.37)$$

$$\mathbf{J}_1^+(\mathbf{r}, t) = +e\delta(x - x_0)\delta(y - y_0)\delta(z - v(t - t_0))[1 - \eta(t - t_0)] \quad (4.38)$$

$$\mathbf{J}_2(\mathbf{r}, t) = -e\delta(x - x_0)\delta(y - y_0)\delta(z - v(t - t_0))\eta(t - t_0) \quad (4.39)$$

$$\mathbf{J}_2^+(\mathbf{r}, t) = +e\delta(x - x_0)\delta(y - y_0)\delta(z - v(t - t_0))\eta(t - t_0) \quad (4.40)$$

where  $(x_0, y_0)$  and  $t_0$  are respectively the coordinates and time of incidence (or emergence) of the real or imaginary charge particle at the screen.

The  $\eta$  function is defined as:

$$\eta(t - t_0) = \begin{cases} 1 & t > t_0 \\ 0 & t < t_0 \end{cases} \quad (4.41)$$

Fourier transforming over time and integrating over transverse coordinates, the corresponding spectral currents are:

$$\check{\mathbf{I}}_1(z) = -e e^{i\omega t_0} e^{i\frac{\omega}{v}z} [1 - \eta(z)] \eta(z + L) \quad (4.42)$$

$$\check{\mathbf{I}}_1^+(z) = +e e^{i\omega t_0} e^{i\frac{\omega}{v}z} [1 - \eta(z)] \eta(z + L) \quad (4.43)$$

$$\check{\mathbf{I}}_2(z) = -e e^{i\omega t_0} e^{i\frac{\omega}{v}z} [1 - \eta(z - L)] \eta(z) \quad (4.44)$$

$$\check{\mathbf{I}}_2^+(z) = +e e^{i\omega t_0} e^{i\frac{\omega}{v}z} [1 - \eta(z - L)] \eta(z) \quad (4.45)$$

Here we included a finite electron trajectory length  $L$  before or after the screen to account for injection or termination of the electron beam. Since most of the TR is generated in the Ginzburg formation length [45], the diffraction integrals should be independent on  $L$  only if:

$$L \gg L_f \quad (4.46)$$

in which case one may set  $L = \infty$ . However, it is desirable to keep  $L$  finite, not only for purposes of numerical computation, but because in practical situations (high electron beam energy, finite screen dimensions ) the effective interaction length  $L$  is realistically finite.

In principle, the diffraction fields of both  $\check{I}_1$  and  $\check{I}_1^+$  (for BTR) need to be calculated separately and summed up coherently and vectorially at the observation point  $P_1$  (and correspondingly so with  $\check{I}_2$  and  $\check{I}_2^+$  for FTR). This is essential

when the electron is not relativistic and its radiation lobe has wide angle [46]. In most practical situations the electrons are relativistic, and the inclination angle of the screen is 45 deg, the two interfering radiation lobes are perpendicular and their angular width is nearly  $2/\gamma \ll \pi/2$ . In this case the radiation lobes do not overlap and one only measures the forward emission of  $I_1^+$  in BTR and of  $I_2$  in FTR.

In the following we analyze the exact and approximate diffraction integrals of  $I_1^+$ , which is the relevant current source for the more useful BTR measurement scheme. The conclusions we derive are equally valid for the other current sources.

#### 4.3.7 Exact Solution

We substitute  $I_1^+(z)$  (4.43) as the line current source in the diffraction integral (4.20) with the exact Green function (4.22).

$$\check{E}_\rho = -\frac{i\omega\mu e}{4\pi} e^{i\omega t_0} \rho \int_{-L}^0 \frac{(z-z')}{R'^3} \left(1 + \frac{3i}{kR'} - \frac{3i}{(kR')^2}\right) e^{ik(R'+\frac{z'}{\beta})} dz' \quad (4.47)$$

If the observation point position satisfies  $kR' \gg 1$  (a sufficient condition is that it is more than a wavelength off axis), then a good approximation for (4.47) is:

$$\check{E}_\rho = -\frac{i\omega\mu e}{4\pi} e^{i\omega t_0} \rho \int_{-L}^0 \frac{(z-z')}{R'^3} e^{ik(R'-\frac{z'}{\beta})} dz' \quad (4.48)$$

here  $z' = -L$  is the inception point of the drifting electron before hitting the screen.

It is important to note that OTR is not emitted instantaneously at the incidence of the electron on the screen, but during its entire traversal time from the point of inception up to the screen incidence time. As discussed in section 4.3.5, most of the contribution to the TR field is accumulated during the elec-

tron traversal through Ginzburg's formation zone  $-L_f < z < 0$ . In figure 4.7 we examine numerically for a specific example, convergence of the OTR field amplitude to a finite value as  $L$  is increased to the limit  $L \gg L_f$ . Equation (4.48) was integrated for exemplary parameters:  $\beta = 0.9999$  ( $\gamma = 75$ ),  $\lambda = 1\mu m$  ( $L_f = 11mm$ ) and observation plane in the far field zone at  $z = 10m$ . The OTR field  $|\check{E}_\rho|^2$  is shown in figure 4.7 as a function of the transverse coordinate  $\rho$  for different values of  $L$ . It is seen that the curves converge slowly to a stable value as  $L$  increases. In this particular example  $N = L/L_f > 1$  provides convergence within 5% to the analytical solution of a semi-infinite long beam (see equation (4.51) in the next section).

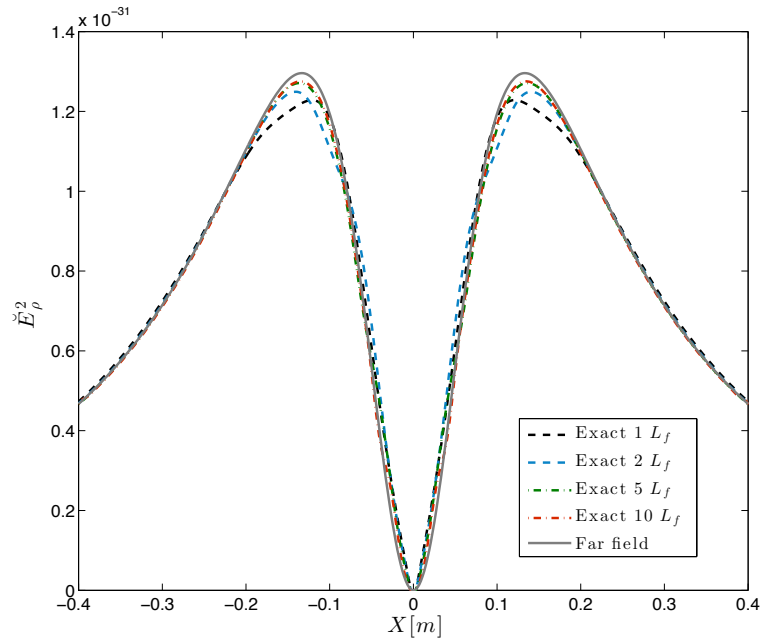


Figure 4.7: Transverse electric field amplitude of TR ( $\lambda = 1\mu m$ ,  $\gamma = 75$ ) at a distance of  $10m$ . Different curves are for increasing integration lengths in formation length units

### 4.3.8 Far field approximation

Using the longitudinal "Fraunhofer" approximation of section 4.3.4, we substitute the "Fraunhofer" Green function (4.34) and the image-charge current source  $I_1^+(z)$  (4.43) in equation (4.20), and obtain for the case of BTR<sup>1</sup>:

$$\check{E}_\rho = -\frac{\omega\mu e^{ikr}}{4\pi r} e^{i\omega t_0} \frac{1}{\left(\frac{\omega}{v} - k_z\right)} \sin\theta \cos\theta \quad (4.49)$$

Substituting  $k_z = \frac{\omega}{c} \cos\theta$ , we find the far-field approximation for the electric field:

$$\check{E}_\rho = -\frac{\mu c e^{ikr}}{4\pi r} e^{i\omega t_0} \frac{1}{\frac{1}{\beta} - \cos\theta} \sin\theta \cos\theta \quad (4.50)$$

Taking the square of the absolute value, we get for small angles:

$$|\check{E}_\rho|^2 = \frac{\mu^2 c^2 e^2 \beta^2}{16\pi^2 z^2} \frac{\sin^2\theta}{(1 - \beta \cos\theta)^2} \quad (4.51)$$

Finally, using (4.25) and  $c^2 = 1/\mu_0\epsilon_0$  we obtain the well-known result for the far-field TR pattern (4.16):

$$\frac{dU_e^2}{d\Omega d\omega} = \frac{e^2 \beta^2}{16\pi^3} \sqrt{\frac{\mu_0}{\epsilon_0}} \frac{\sin^2\theta}{(1 - \beta \cos\theta)^2} \quad (4.52)$$

The analytical expression (4.51) for a semi infinite electron trajectory is presented in figure 4.7 in a solid line, shown to be the limit of convergence of the numerical solution in the far field zone and  $L \rightarrow \infty$ .

As indicated earlier, the complete TR field should include (for BTR) also the

---

<sup>1</sup>The strict mathematical integration of equation (4.35) results in an oscillatory dependence on  $(z_2 - z_1)$ . The commonly used approximation (4.49) results in from neglect of the lower limit of the integral in equation (4.35) for physical reasons (e.g. diffraction effect due to the finite dimensions of the screen). In any case, a necessary condition for the validity of (4.49) is  $L = z_2 - z_1 \gg L_f$ .

contribution of the real electron current  $\check{I}_1(z)$  (4.42) summed up coherently and vectorially with the main field contribution of the image charge (4.50). This can be straightforwardly done in the case of normal incidence on the screen, resulting in equation (4.16). The difference may be significant only at non-relativistic electron energies, but also in this case, if the screen tilt angle is different from 0, one must use (4.50) and the corresponding field distribution of  $\check{I}_1(z)$  to calculate the resultant OTR field [45].

### 4.3.9 Fresnel Approximation

In the longitudinal quadratic phase ("Fresnel") approximation (section 4.3.3), the transverse electric field is given by equation (4.31). We apply the diffraction formula, integrating over  $I_1^+(z)$  (4.43).

Figure 4.8 presents the results of the numerical computation for the distance of  $z = 10\text{cm}$  ( $\gamma = 75$ ), which is well within the approximation regime (4.32). We display the results of the computation with the exact diffraction formula (4.47) and with the "Fresnel" diffraction formula (4.31). The curves overlap. The integration length used was one formation length. We also display for comparison the field radiation pattern that would be expected from the far-field formula (4.51).

The example shows good match between the exact and the "Fresnel" solutions, while the far field approximation curve differs significantly, both in amplitude and peak locations.

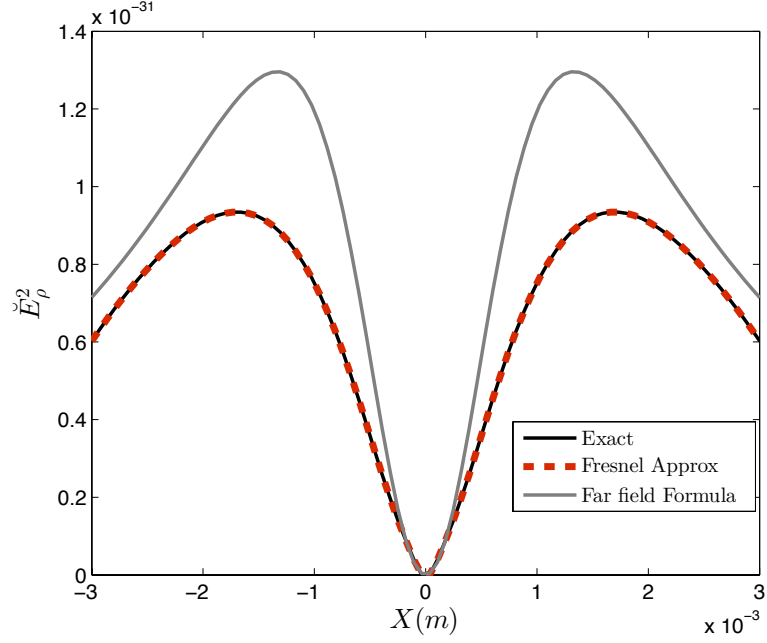


Figure 4.8: Transverse electric field amplitude in the near field zone of TR ( $\lambda = 1\mu m$ ,  $\gamma = 75$ ,  $z = 10cm$ ). The exact solution and the Fresnel approximation, computation results overlap. The numerical integration was performed over 1 formation length. We show for comparison the field radiation pattern that would be predicted from the far zone formula (4.51).

#### 4.3.10 Reactive near field regime

In order to verify the correctness of the transverse electric field expression in all space, we compare the obtained exact solution computation results to the Coulomb field of a relativistic particle (4.1). At the screen location  $z = 0$ , one must expect that the computed field solution replicates the Coulomb field of the electron.

Figure 4.9 presents the transverse electric field variation as a function of  $\rho$  calculated using the exact solution (4.47) in the reactive near-field zone -  $z = 0.1, 1, 5, 20\mu m$  and the Bessel  $K_1$  function solution (dots) of the analytical Coulomb field expression [37] in the frequency domain (4.1). The X-axis val-

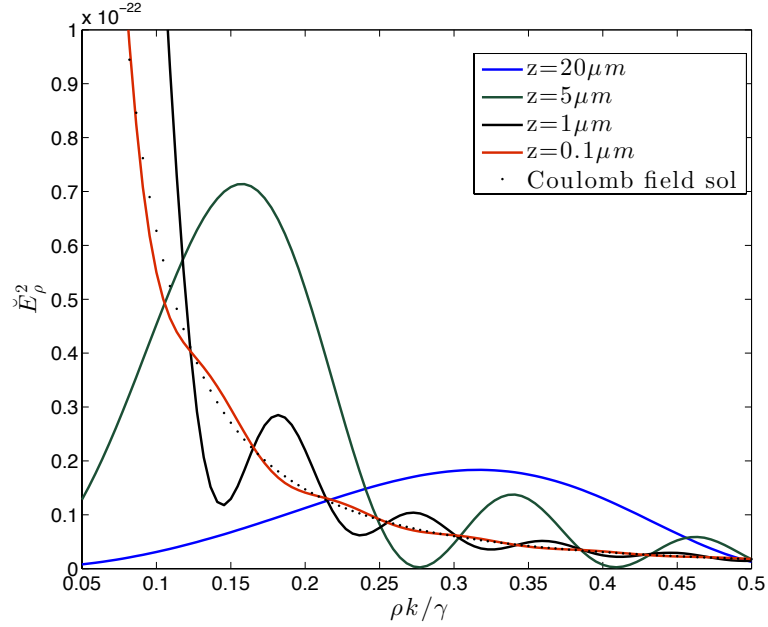


Figure 4.9: Transverse electric field amplitude calculated using the exact solution, at various observation distances in the reactive near-field compared to the Coulomb field of a relativistic particle (4.1) (dots). The figure demonstrates the transition of the Coulomb field to radiation field. X-axis values are presented in normalised units  $\rho k/\gamma$ .

ues are presented in normalised units  $\rho k/\gamma$ . The reconstruction of the Coulomb field is very good. The figure demonstrates vividly the transition of the electron Coulomb field to radiation field.

#### 4.4 OTR and COTR from an Electron Beam Using the Exact (Dyadic Green Function) Diffraction Formula

The exact single electron OTR diffraction formula derived in the previous section makes it possible to calculate the resultant OTR field of a beam of electrons at

any distance - near or far field. Due to the fact that the field solution we obtain is in the complex plane (amplitude and phase), we can sum the field contributions from the different electrons taking into account interference effect, as well as polarisation.

In this section we show simulation results of OTR emission from an electron beam in the near and far field for random, coherently modulated and partially coherent (noise-suppressed) electron beams. In principle, simulation of OTR of a beam does not require separate computation of the diffraction field for each electron in the beam. Using the exact expression for the field from a single electron propagating on axis (4.47) we can express the field of an electron that propagates in the forward direction off axis and at an angle relative to the beam axis, by simple coordinate transformations of translation and rotation.

For simplicity we consider here only a beam of finite uniform transverse distribution in a cylindrical (pencil beam) geometry, neglecting angular spread. In this case the exact resultant OTR field of a beam of  $N$  particles is:

$$\check{\mathbf{E}}(x, y, z, \omega) = \sum_{i=1}^N \check{\mathbf{E}}_e(\rho_j, \phi_j, z, \omega) \hat{e}_{\rho_j} \quad (4.53)$$

where

$$\rho_j = |\mathbf{r}_{\perp} - \mathbf{r}_{\perp j}| = [(x - x_{0j})^2 + (y - y_{0j})^2]^{1/2} \quad (4.54)$$

$$\hat{e}_{\rho_j} = \frac{\mathbf{r}_{\perp} - \mathbf{r}_{\perp j}}{|\mathbf{r}_{\perp} - \mathbf{r}_{\perp j}|} = \hat{e}_x \cos \phi_j + \hat{e}_y \sin \phi_j \quad (4.55)$$

$$\cos \phi_j = \frac{x - x_j}{\rho_j(x, y)} \quad (4.56)$$

$$\sin \phi_j = \frac{y - y_j}{\rho_j(x, y)} \quad (4.57)$$

and  $\check{\mathbf{E}}_e$  is the single electron exact solution (4.47), for which we write  $R'_j$  as:

$$R'_j = \sqrt{\rho_j^2(x, y) + (z - z_j)^2} \quad (4.58)$$

This method makes it possible to combine coherently the radiation fields of the different electrons of the beam, and compute the total OTR radiation field emitted by the beam and thus observe COTR effects.

In the next subsection we use the exact OTR computation code for a beam (4.53) for the simple case of coherent periodic modulation, and compute the OTR field pattern in the near and far zones. A coherently modulated beam is expected to produce increased integrated radiation intensity (super-radiance [14]) in proportion to the square of the number of electrons  $N^2$  and the modulation factor  $M_b^2$ . This intensity is orders of magnitude larger than the OTR emission from a random un-modulated beam (that is proportional to  $N$ ).

In the subsequent subsection we employed the same code for calculating the OTR intensity pattern in the near and far field where the coordinates and entrance times of the electrons were imported from the output of GPT simulations of beam transport. Both cases of a non-interacting beam (drift length  $L = 0$ ) and quarter plasma wavelength drift length ( $L = L_{\pi/2}$ ) were simulated in order to demonstrate that the integrated OTR intensity is suppressed in the case of an interacting beam, reflecting the suppression of the beam current noise [7]. In all examples the transverse profile of the beam was taken to be uniform, and particles transverse coordinates at entrance was randomly distributed.

#### 4.4.1 Coherently modulated beams

In this computation I used a model in which a fixed number of macro-particles in the beam ( $N = 150K$ ) was used in each case, but a different fraction  $0 < M_b < 1$  were current-amplitude modulated periodically. The periodic modulation function was assumed to be a train of Gaussian bunch distribution function as shown in figure 4.10 in the spatial dimension. The period of the density modulation is  $\lambda = (2\pi c/\omega)\beta$ , where  $\omega$  is the radiation frequency. The Gaussian bunches standard deviation width was taken to be  $\sigma = \lambda/6$ . The integrated number of particles in the modulated part is  $M_b N$ .

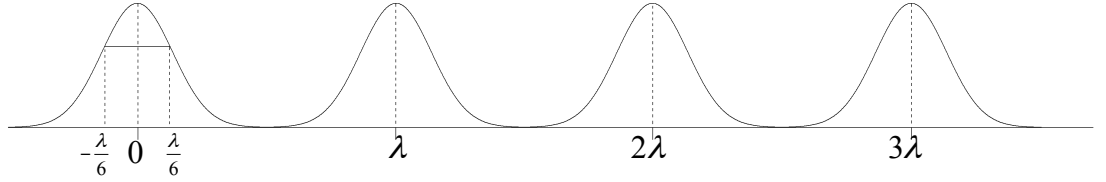


Figure 4.10: Density modulation function in the time-domain for a perfectly modulated beam.

Figure 4.11 presents results of the far-field radiation patterns of OTR emission ( $z=10m$ ) for the parameters of LCLS 4.1, at modulation and radiation emission wavelength of  $1\mu m$ . Computation results are shown for various beam modulation levels: from a randomly distributed beam ( $M_b = 0$ ), partially modulated beam ( $M_b = 0.5$ ) and a full coherently modulated beam ( $M_b = 1$ ). The same colour-bar scale is used in all images. Figure 4.12 shows a cross-cut of the radiation lobes for the three cases. A significant increase in radiation can be noticed between the un-modulated and the modulated beams, as was expected. This is the result of the coherent contributions from the modulated electrons. The intensity from the radiation of the modulated beam grows as  $M_b^2$  (factor of  $\times 4$  between  $M_b = 0.5$  and  $M_b = 1$ ) in figure 4.12.

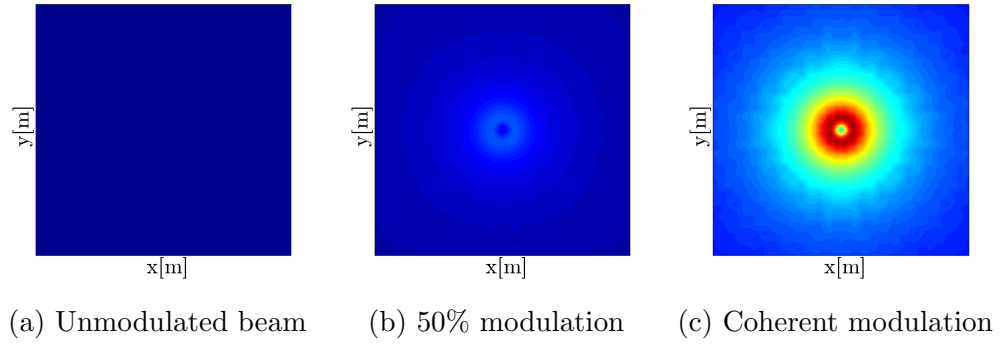


Figure 4.11: OTR emission ( $1\mu m$  wavelength), at  $z=10m$  from a randomly distributed beam (a), partially modulated beam (b) and a coherently modulated beam (c). The same colour-bar scale is used in all images. A significant increase in radiation power takes place for higher coherence levels.

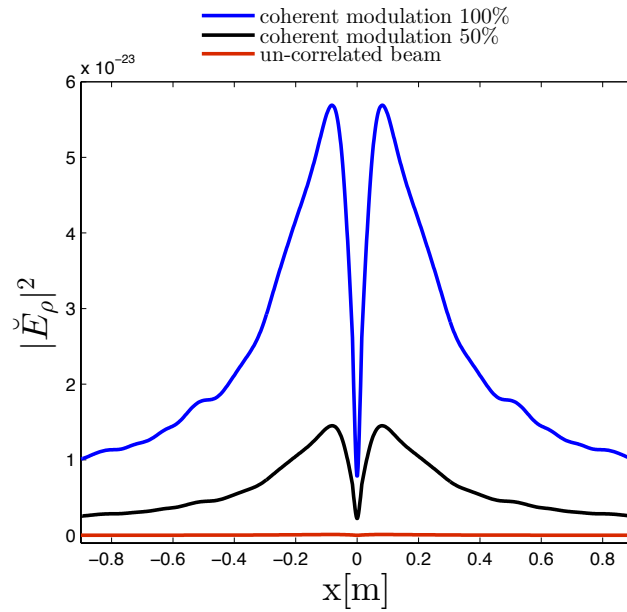


Figure 4.12: OTR emission ( $1\mu m$  wavelength), at  $z=10m$  from a randomly distributed beam (red), partially modulated beam (black) and a coherently modulated beam (blue). The same colour-bar scale is used in all images. A significant increase in radiation power takes place for higher coherence levels.

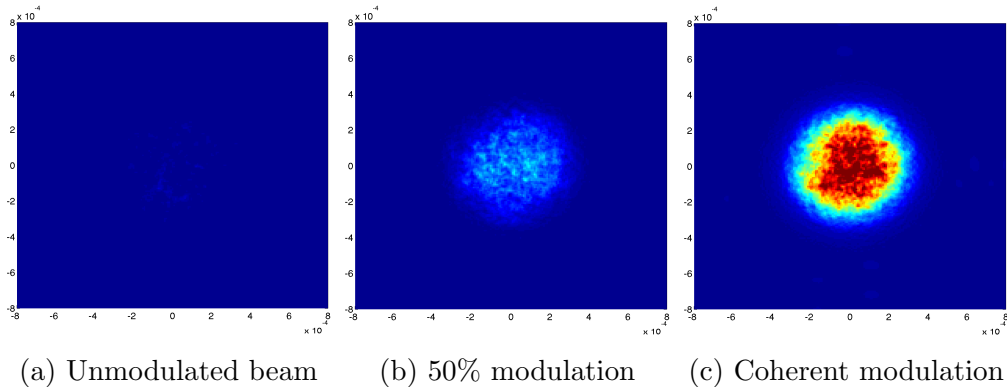


Figure 4.13: OTR emission at  $1\mu\text{m}$  wavelength, at  $z=1\text{mm}$  from a randomly distributed beam (a), partially modulated beam (b) and a coherently modulated beam (c). The same colour-bar scale is used in all images. A significant increase in radiation power takes place for higher coherence levels.

Simulated radiation patterns in the near field for OTR emission at a short distance ( $1\text{mm}$ ) are presented in figure 4.13 for the same three modulation levels. We used the same colour scale for the three images in order to demonstrate the significant increase in emitted power for higher modulation level in the electron beam. Figure 4.14 shows the cross cut of the radiation pattern for the three cases presented in 4.13. the increase in radiation power for higher modulation levels (factor of  $\times 4$ ) is clearly depicted. The spiky characteristics of the curves reflect the limited number of sample particles used.

#### 4.4.2 GPT simulated beam

In this subsection we use the code for exact calculation of OTR emission from an electron beam in order to evaluate the OTR pattern and intensity of a correlated electron beam that underwent collective micro-dynamics in a drift section. Since OTR measurements is the experimental diagnostics we use for verifying the current noise suppression effect, this computation is most relevant for the present work.

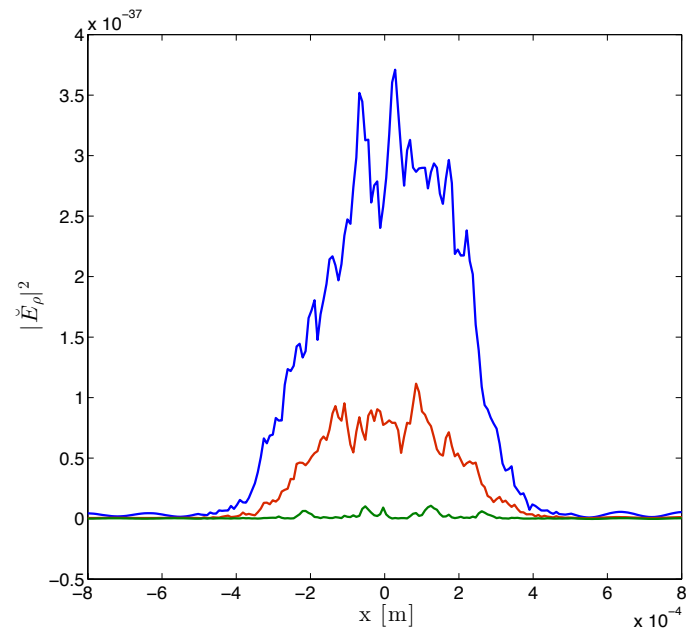


Figure 4.14: A cross-cut of the OTR emission at  $1\mu m$  wavelength, at  $z=1mm$  using a randomly distributed beam (green), partially modulated beam (red) and a coherently modulated beam (blue). A significant increase in radiation power takes place for higher coherence levels.

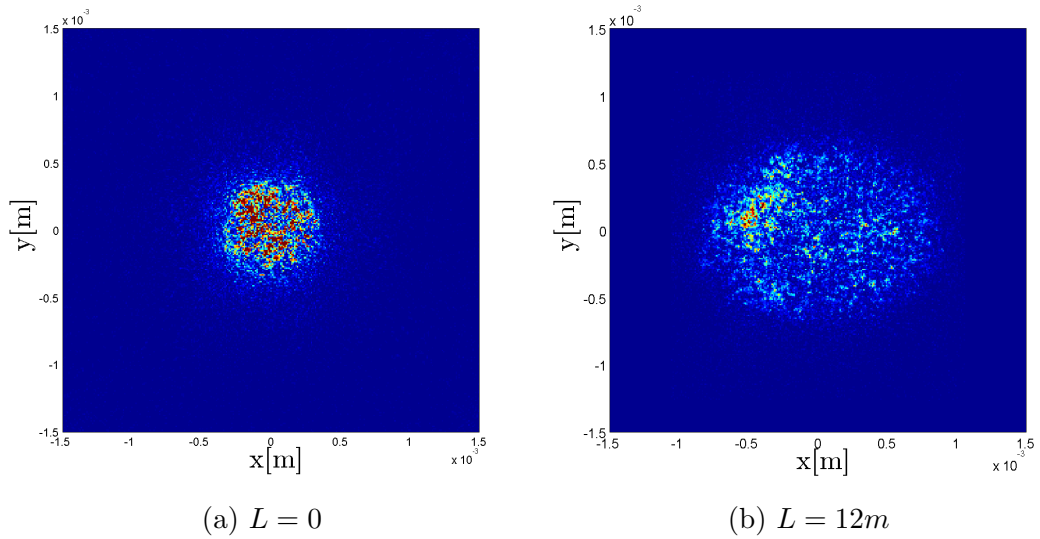


Figure 4.15: Near-field OTR emission ( $z = 1\text{mm}$ ) at  $1\mu\text{m}$  wavelength, from a GPT simulated beam at  $L = 0$  (shot-noise) and at  $L = L_{\pi/2} = 12\text{m}$  (quarter plasma wavelength oscillation).

We used the OTR computation code for an input electron beam, where the 3D coordinates of each electron near the OTR screen were imported from the earlier GPT simulations. These simulations were carried out for the SLAC injector parameters (table 4.1). We computed the OTR field pattern in the near field  $z = 1\text{mm}$  (figure 4.15) and in the far field at  $z = 1\text{m}$  (figure 4.17) and  $z = 10\text{m}$  (figure 4.19) for radiation wavelength  $\lambda = 1\mu\text{m}$  in two cases: (a) A randomly phased electron beam ( $L = 0$ ) that is expected to be dominated by the classical shot-noise and produce conventional OTR (figures 4.15a and 4.17a). (b) A correlated beam that underwent collective interaction in the GPT simulation code for an interaction length of  $L = L_{\pi/2} = 12\text{m}$ , and was shown to have current noise suppression (relative to shot noise - chapter 3), and is expected to exhibit coherently suppressed COTR.

This pattern approximately replicates the actual beam transverse distribution at the screen and the camera's image pattern if it is focused to image the OTR

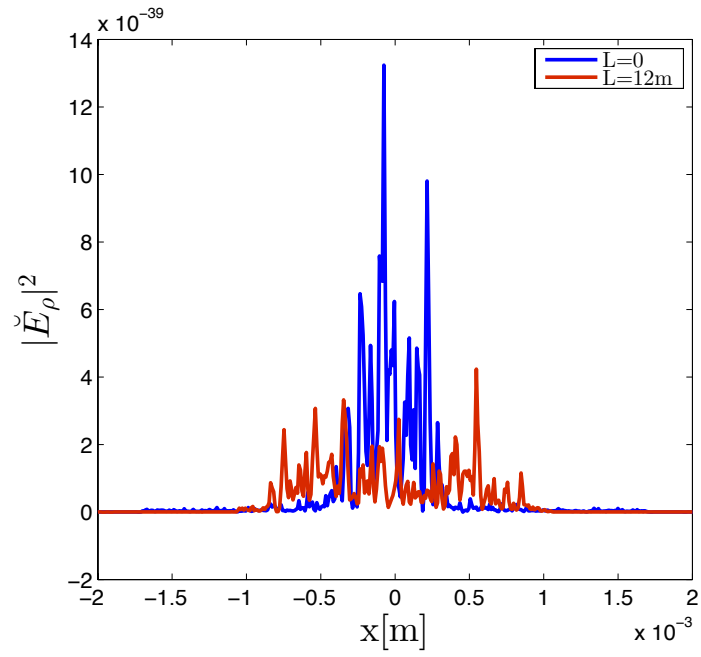


Figure 4.16: A cross-cut of the near field OTR emission at  $1\mu m$  wavelength, at  $z = 1mm$  at two locations:  $L = 0$  (shot noised beam) and at  $L = L_{\pi/2} = 12m$  (quarter plasma wavelength oscillation)

screen. We also present the cross-cut of this pattern in figure 4.16. An appreciable suppression can be seen between the radiations of the uncorrelated ( $L = 0$ ) and correlated beam ( $L = 12m$ ). The suppression of the integrated intensity was computed to be about 25% ( $1.85 \times 10^{-35}$  to  $1.5 \times 10^{-35}$ ).

Figures 4.17a and 4.17b present results for the far-field OTR images using the same scheme. This time, radiation was calculated for a distance of  $z = 1m$ . We note that in the case of the non-correlated beam 4.17a, the "bagel" pattern of OTR emission from a single electron is approximately preserved. The irregularity may be attributed to the limited number of sample particles used (150K). On the other hand, in the case of the correlated beam 4.17b, not only the intensity is reduced but also the "bagel" pattern is somewhat destroyed (for the same number of particles).

Figure 4.18 presents the cross-cut of this pattern at the two locations. The cross cut results show appreciable suppression. The integrated intensity of the images in 4.17a, 4.17b (summation over all image pixels) showed suppression of about 40% ( $7.7 \times 10^{-39}$  to  $4.6 \times 10^{-39}$ ) between the far-field emission images. Note that the calculated integrated intensity suppression in the far field is somewhat higher than the suppression in the near field. It is possible that this fact is associated to the number of sample particles used (limited by our computational resources).

Figures 4.19a and 4.19b present results for the far-field OTR images for a distance of  $z = 10m$ . Figure 4.20 presents the cross-cut of this pattern at the two locations. The bagel shape here is clear and the suppression is almost identical to the previous far field case (40% as for  $z = 1m$ ).

These results of the numerical computation indicate that noise-suppression can be detected using OTR measurements.

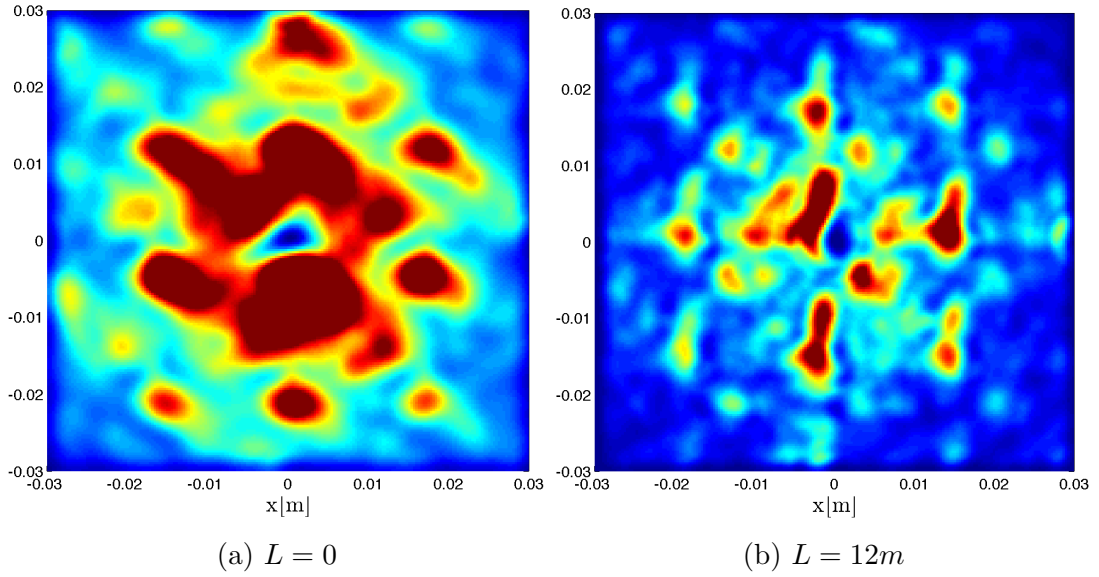


Figure 4.17: Far-field OTR emission ( $z = 1m$ ) at  $1\mu m$  wavelength, from a GPT simulated beam at  $L = 0$  (shot-noise) and at  $L = L_{\pi/2} = 12m$  (quarter plasma wavelength oscillation).

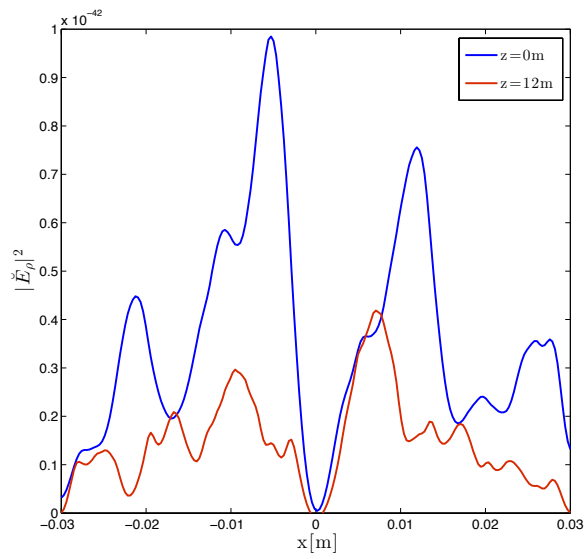


Figure 4.18: A cross-cut of the far field OTR emission at  $1\mu m$  wavelength, at  $z = 10m$  at two locations:  $L = 0$  (shot noised beam) and at  $L = L_{\pi/2} = 12m$  (quarter plasma wavelength oscillation)

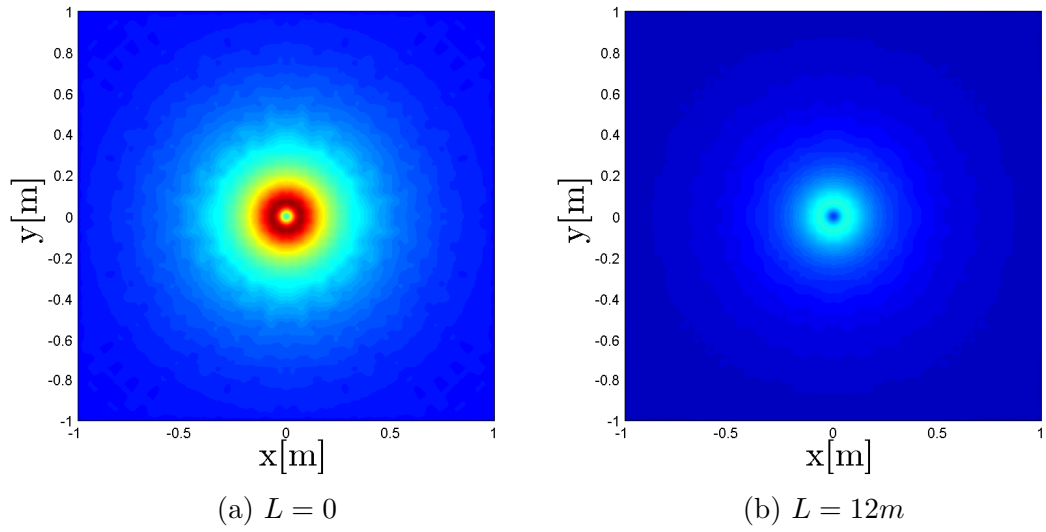


Figure 4.19: Far-field OTR emission ( $z = 10m$ ) at  $1\mu m$  wavelength, from a GPT simulated beam at  $L = 0$  (shot-noise) and at  $L = L_{\pi/2} = 12m$  (quarter plasma wavelength oscillation).

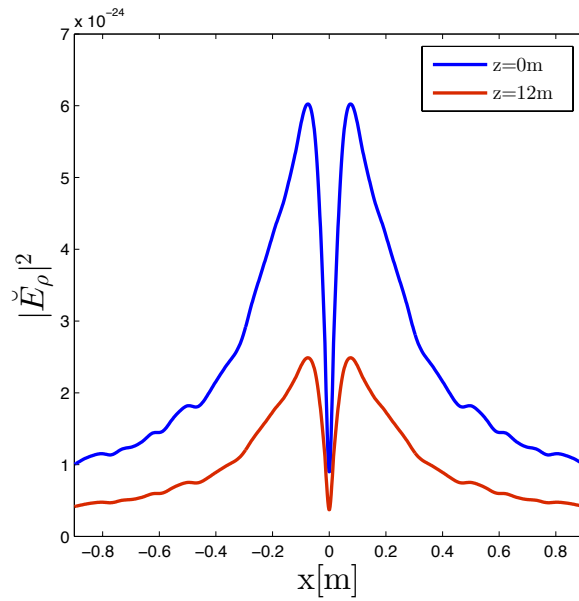


Figure 4.20: A cross-cut of the far field OTR emission at  $1\mu m$  wavelength, at  $z = 10m$  at two locations:  $L = 0$  (shot noised beam) and at  $L = L_{\pi/2} = 12m$  (quarter plasma wavelength oscillation)

## CHAPTER 5

# Preliminary Experimental Study of Collective Noise Dynamics Control in LCLS

The Linac Coherent Light Source (LCLS) is currently the most advanced 4th generation FEL facility in the world. LCLS is located in Stanford's Linear Accelerator (SLAC). This facility is the first ever to demonstrate a functional X-ray FEL [3] and was successful in realising a long hoped-for goal. LCLS produces pulses of X-rays more than a billion times brighter than the most powerful existing sources, the so-called synchrotron sources which are also based on large electron accelerators.

In order to achieve this, the LCLS gun and acceleration sections were carefully designed to produce a bright, high charge, extremely low emittance electron beam. These requirements introduced some new diagnostics problems (specifically COTR interference speckled patterns on the OTR beam diagnostics screens), which initially could not have been explained [4].

Our first experimental study of collective noise dynamics was conducted in LCLS. Following the experiment of [4] in this facility that essentially indicated current noise gain in the LCLS injector, we expected that this would be a fitting vehicle for demonstrating the predicted noise suppression effect. We obtained a very short period of machine time to examine the effect in the injector section by measuring OTR from screens along the drift section between the accelerator

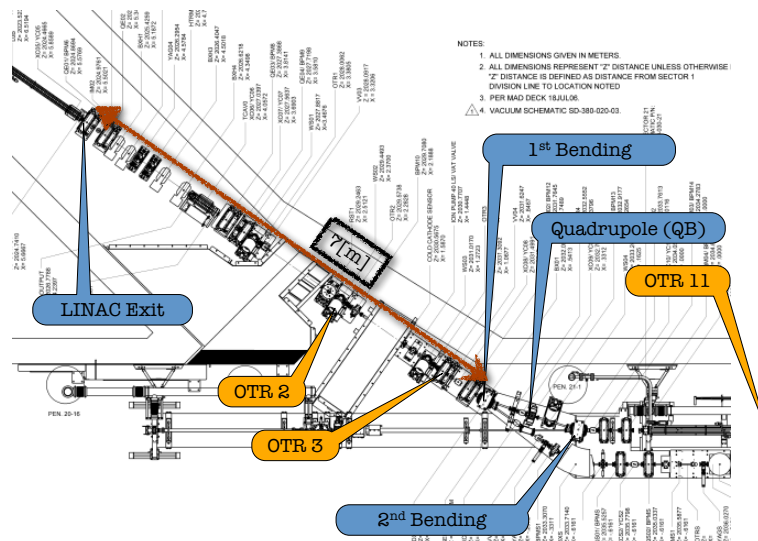


Figure 5.1: LCLS injector section. OTR screens are marked in yellow

exit and the dog-leg bend (Figure 5.1).

In preparation for the experiment I conducted GPT simulations of the noise dynamics in the injector beam from the accelerator exit up to the dog-leg bend passing through two OTR screen stations (OTR2 and OTR3 see figure 5.2. Another OTR screen - OTR1- further upstream was unavailable at the time). Furthermore, I continued the simulation also beyond the bend up to a third OTR screen (OTR11) beyond the accelerator section  $L1s$  (see figure 5.2 OTR11 is not shown), which was assumed to be turned off. This was in essence a simulation of the noise gain experiment [4].

As discussed in the next sections, the simulation confirmed the attainment of noise gain beyond the bend (due to the  $R_{56}$  parameter of the bend), but also showed appreciable current noise suppression in the drift section before the bend that could be possibly measured in the OTR3 screen.

Encouraged by the simulation results we conducted noise suppression exper-

iment by measuring the integrated OTR output in screens OTR2 (before the drift) and OTR3 (after the drift).

The experimental results, as reported in the next sections, were encouraging and indicated a small noise suppression effect in agreement with the simulation predictions. Because of the limits of approved machine time for experiments, the experiment was not reproduced at different beam parameters for a complete characterisation of the effect. However the results were promising enough to justify a follow-up experiment, that was conducted later-on in the ATF (Accelerator Test Facility in Brookhaven National Lab) and is described in chapter 6.

## 5.1 Constructing the Simulation Model of the LCLS Injector

The injector section in LCLS is constructed of an RF gun, followed by an emittance compensation solenoid, two acceleration sections, a laser heater chicane (that is used for removal of micro-bunching instabilities, but was turned off during the experiments and was not included in the simulations), three OTR screens and a dog-leg bend which inject the beam into the main beam-line before final acceleration and injection into the Undulator (Figure 5.2). Electron-optics such as quadrupoles magnets, which are used in order to control the beam focusing along the beam line, are installed along the transport line and can be controlled during the measurements.

Estimation of the extent of the collective interaction current noise suppression effect required simulation only of a simple drift section from the exit of the first two Linac sections  $L0a$ ,  $L0b$  downstream to the dog-leg bend. Never the less, in order to compare our simulations earlier experiment of Akre et al [4], we continued

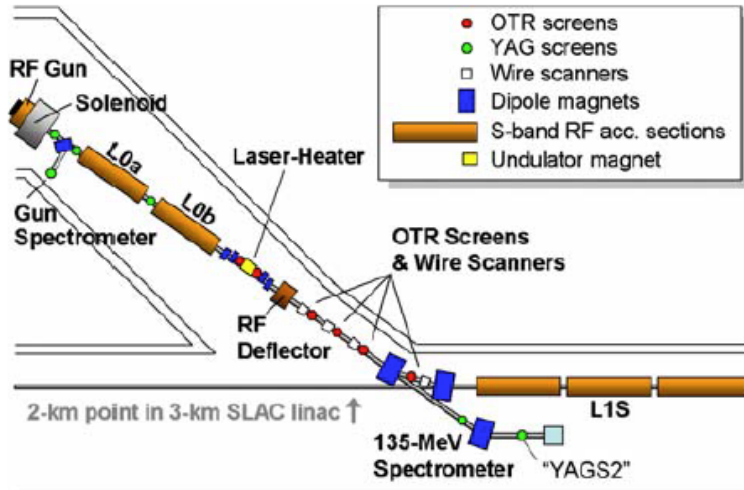


Figure 5.2: LCLS injector section

the simulation also beyond the bend. We expected [7], [6] to see suppression in the current noise during the drift to the bend and gain after the bend. The current-gain is expected to grow after the bend due to the transformation of the velocity-noise enhancement before the bend into current noise after the bend, by the  $R_{56}$  parameter dispersion effect of the bend.

In order to do so, we used the GPT simulations with an adaptive coordinate system that measures the location of each particle from a vector, pointing in the direction of beam propagation ( $\hat{e}_z$ ), regardless of where it points in space. Magnet simulations included the two magnets which the dog-leg bend is constructed of, including the fringing field effects of the 1st order. The simulation was carried out up to the position of screen of OTR11 assuming that the accelerator units  $L1s$  are turned off.

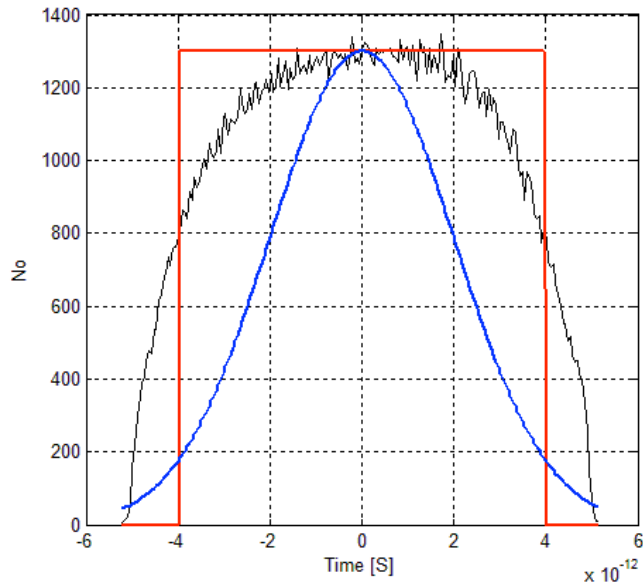


Figure 5.3: LCLS beam axial current profile measurements (black), a Gaussian model (blue) and a step function (red). In our simulations we used a step function model of the axial current distribution.

### 5.1.1 Simulation Considerations

The LCLS beam has a Gaussian transverse distribution. We used equal beam width sizes in both axes ( $x$  and  $y$ ). The longitudinal profile of the e-beam bunch current was treated in the simulations as a flat distribution. Figure 5.3 presents the real profile (in black), and for reference another two curves - a step function (red) and a Gaussian with  $\sigma_z=2.5\text{pS}$  (blue). One can notice that a step function (especially in the center of the pulse) is more appropriate model assumption for describing the current profile. Note that the noise calculation in the Matlab scripts carried out *in the center* of the pulse and therefore the choice of the rectangular profile model is reasonable.

Table 5.1 presents the e-beam parameters used in the simulations. Beam focusing along the drift was achieved using quadru-pole magnet models included in

Energy	135 <i>MeV</i>
Transverse density profile	Gaussian
Charge	0.25,0.5 <i>nC</i>
Duration	5 <i>pS</i>
$\sigma$	170 $\mu m$
Emittance	1 $\mu m$
Energy spread	5 <i>KeV</i>

Table 5.1: LCLS simulations beam parameters

the GPT simulations. Point to point space charge 3D was used in all simulations. We used 250K macro particles for each simulation. Current noise was estimated for a band of 1-2 $\mu m$  wavelengths.

GPT simulations were carried out for these parameters in order to calculate the current noise suppression level at the positions of OTR2, OTR3 and OTR11. Furthermore, I used the data of beam particle locations at OTR2 and OTR3 for calculating the expected near field OTR pattern using equation (4.53), to be used for comparison with OTR screen image recordings.

## 5.2 Simulation Results

Figure 5.4 presents the results of noise dynamics for a GPT simulated LCLS beam for drift along more than a quarter plasma oscillation. According to the beam parameters, quarter plasma oscillation would take place after a propagation distance of 12*m*. This figure demonstrates a maximal suppression after such distance. The black vertical line represents the location of the dog-leg bend.

The red and blue vertical lines indicate the positions of OTR2 and OTR3 respectively. Evidently, it is not possible to measure in this configuration maximum noise suppression at the maximum suppression point because the bend is

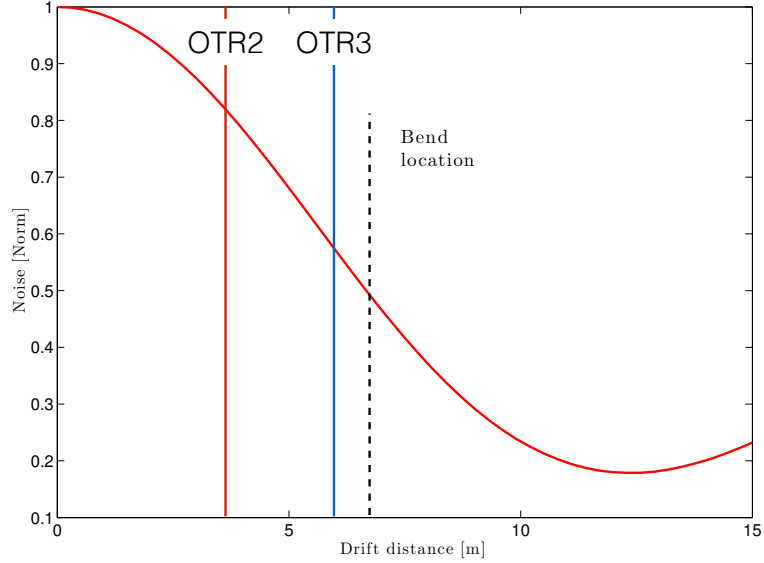


Figure 5.4: Noise dynamics for more than a quarter plasma oscillation. Noise was estimated in bandwidth of  $1-2\mu m$ . Quarter plasma oscillation distance is  $12m$ . Vertical dashed black line represent the location of the dog-leg bend in LCLS machine. This simulation is a reference simulation for the real-life bend-included simulation.

located before this point. However, the curve shows that appreciable suppression still takes place from OTR2 to OTR3.

For comparison with the earlier experiment of Akre et al [4] I operated GPT for the real parameters of the LCLS beam transport including the magnetic field of the bending dipole. In this case we expect to replicate the noise gain effect observed in that experiment. Figure 5.5 displays the current-noise development as a function of transport length for two examples of beam charge:  $0.25 nC$  and  $0.5 nC$ .

The noise suppression due to the collective interaction noise dynamic is demonstrated well in the drift section before the bend  $0 < z < 7m$ , with more pronounced effect in the case of the high charge example (and larger  $\omega_p$ ), as expected theoretically. After the bend the trend turns into current noise growth due to the

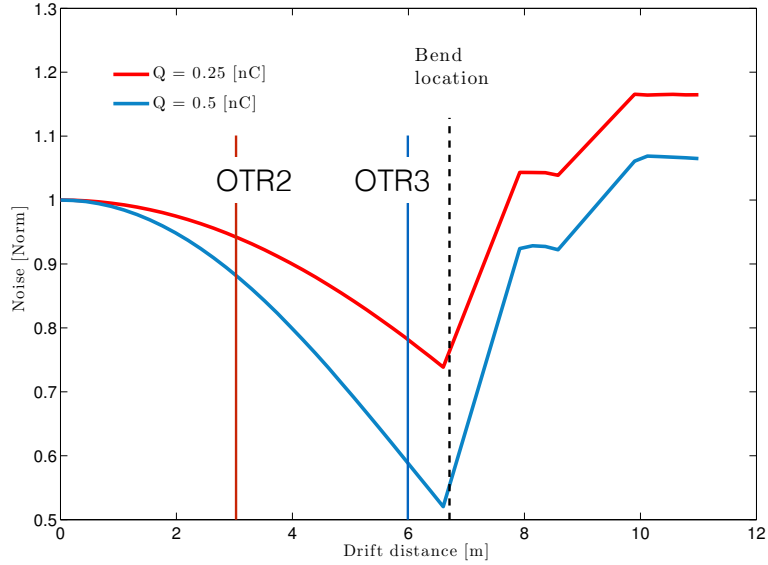


Figure 5.5: Noise dynamics from GPT simulation of LCLS for two pulse charges - 0.25 and 0.5 nC. Noise was estimated in bandwidth of 1-2  $\mu\text{m}$ . Vertical dashed black line represent the location of the dog-leg bend in LCLS machine. Current noise gain takes place after the bend.

$R_{56}$  effect in the two bending magnets of the bend. The noise level at the end is larger than at the start in either case.

Figure 5.6 presents the predicted near field OTR intensity pattern from the GPT pulse at the location of OTR-2 ( $z = 3\text{m}$ ) (red) and just before the bend - the location of OTR-3 ( $z = 6\text{m}$ ) (blue). OTR was calculated using the exact diffraction dyadic Green function expression that was presented in the previous chapters (4.53).

The expansion of the pattern at  $z = 6\text{m}$  is the result of the electron beam expansion in the drift section from  $z = 3\text{m}$  to  $z = 6\text{m}$ . However, it is evident that the integrated OTR intensity within the spot is smaller at  $z = 6\text{m}$  than in  $z = 3\text{m}$ , indicating predicted effect of OTR energy suppression (a computed factor of app. 20%) between OTR2 to OTR3).

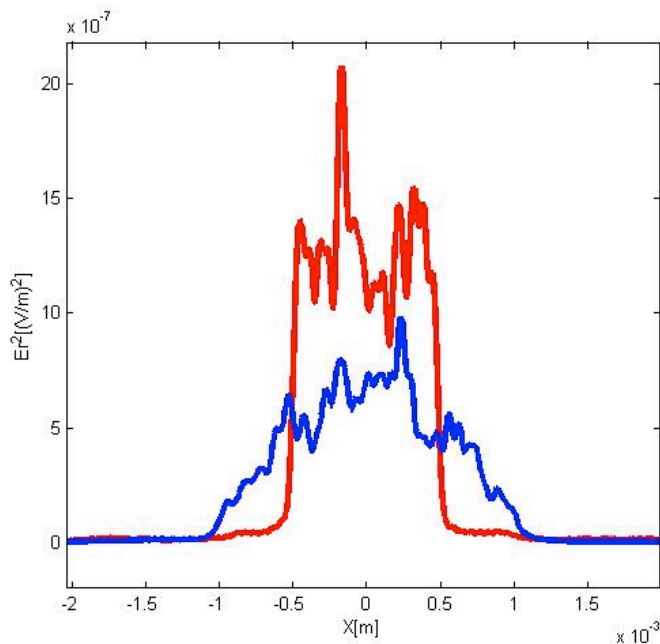


Figure 5.6: OTR intensity calculated from GPT simulation of LCLS beam, at OTR2 -  $z = 3$  - (red) and at location of OTR3 -  $z = 6m$  - (blue).

## 5.3 Experimental Measurements

### 5.3.1 Measuring OTR in LCLS

The beam diagnostics in the linac for the Linac Coherent Light Source (LCLS) X-ray FEL at SLAC includes optical transition radiation (OTR) screens for measurements of transverse and longitudinal beam properties. Diagnostics using OTR are implemented at various stages of the LCLS accelerator. We used the screen after the first acceleration section (labeled OTR2), the screen before the dogleg (OTR3) and the first screen after the bend and the (turned off) accelerator *L1s* (OTR11).

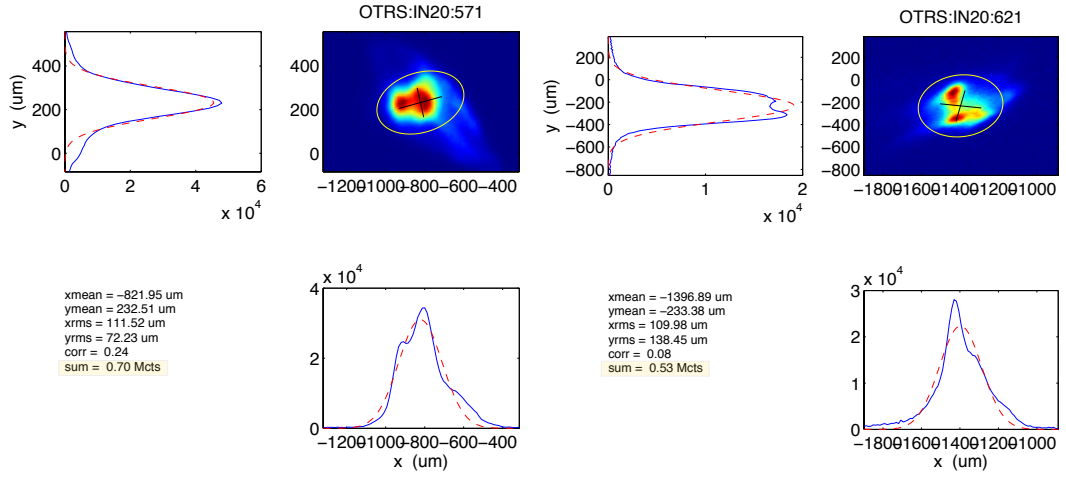
The OTR diagnostics consist of a  $1\mu m$  thick Aluminum foil oriented at 45 degrees to the beam, two insertable neutral density filters, a telecentric lens with

numerical aperture of 0.18 and working distance of 160 *mm*, and a mega-pixel CCD camera with a 0.42 magnification, giving a calibration of 11 pixels per  $\mu m$  in the object plane. The CCD has a 12-bit digitizer with an effective signal to noise ratio of 1000. The efficiency in terms of number of photons per electron is usually of the order of  $10^{-3}$ ,  $10^{-2}$  and has only a logarithmic dependence on the beam energy. The resolution is only limited by the imaging optics, and beam sizes as small as 5  $\mu m$  have been observed.

### 5.3.2 Indication of OTR Sub-Radiance?

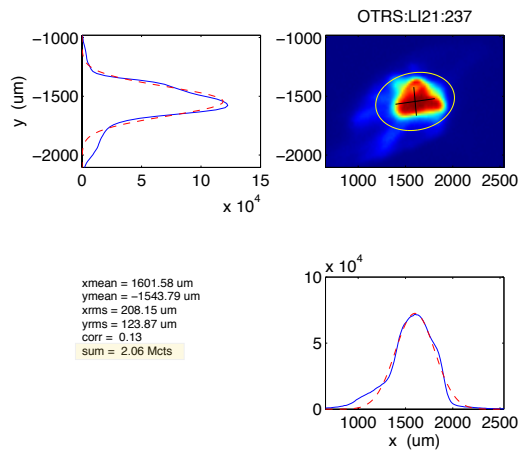
The experimental results of measurements in OTR2, OTR3 and OTR11 are presented in figure 5.7. The camera was focused to image the screen. Figure 5.7 displays a Matlab script processing of the measured signal data from the camera. The figure shows colour code intensity map of the OTR screen image, location of the mean-value of the image pattern, the pattern functional radiation in two vertical cross section cuts in the image plane and their standard deviations. It also indicates the integrated intensity as the number of counts (cts) from each image.

The beam charge used in the experiment was 500 *pC*. The OTR2 image had an integrated intensity (summation) of 0.7 Mcts, while the OTR3 image integrated intensity indicated reduction to 0.53 Mcts. Since the beam charge was the same in both locations (no beam loss) and there were no electron-optical components between the two locations except for a simple drift, it is reasonable that the suppression effect of the OTR intensity at the second screen, though small, is a result of the collective dynamics in the beam during the drift section as expected theoretically and predicted by the numerical simulations (4.4.2).



(a) OTR2 screen image

(b) OTR3 screen image



(c) OTR11 screen image

Figure 5.7: OTR Images of screens OTR2 (a) OTR3 (b) and OTR11 (c), located between the accelerator exit, the dog-leg bend and after the bend and  $L1s$  acceleration section respectively. Results show integrated intensity reduction from 0.7 Mcts to 0.53 Mcts within the drift section, and a significant enhancement of the OTR intensity to 2 Mcts at OTR11. Beam charge was  $500pC$ .

## CHAPTER 6

# First Observation of Current Noise Suppression Below the Shot-Noise Limit in Relativistic Charged Electron-Beam

Noise suppression below the shot-noise limit in electron beams was never demonstrated experimentally in the optical regime. In this chapter we describe the experiment conducted in order to demonstrate this effect. We present in this chapter the experimental set-up, the experimental results and a full analysis, which includes numerical simulations in order to fully understand the conditions and also the limitations of this experiment.

### 6.1 The Experimental Concept

The noise suppression demonstration experiment was conducted on the 70 *MeV* RF-LINAC of ATF (Figure 6.1). The beam current noise measurement was made by recording the OTR emitted from a copper screen placed  $L=6.5$  *m* away from the accelerator exit. Keeping the camera and screen CTR1 position fixed, the practical way to control the plasma phase  $\phi_p$  was to vary the beam pulse charge (200-500 *pC*), and the beam energy  $E = (\gamma - 1)mc^2$  (50 to 70 *MeV*). The quadrupoles settings were readjusted for each beam acceleration energy, and the beam spot sizes  $\sigma_x, \sigma_y$  were measured at four points (YAG1-YAG4) along the

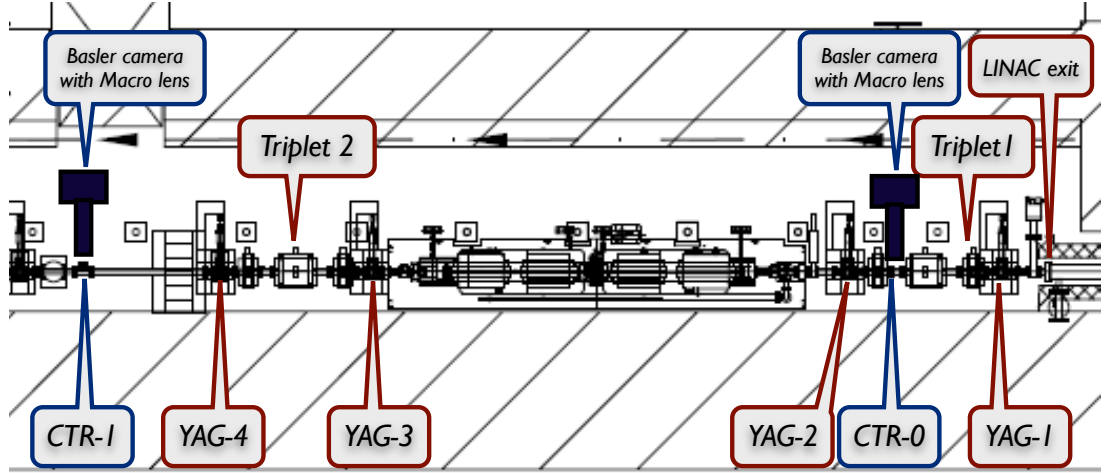


Figure 6.1: The experimental set-up. The ATF e-beam transport set-up is shown from the injector RF-LINAC exit to the OTR viewer site (CTR-1). The accelerated beam energy was varied from  $50\text{MeV}$  to  $70\text{MeV}$  and the beam charge was varied from  $200\text{pC}$  to  $500\text{pC}$ . The beam spot dimensions were measured at four locations using fluorescent screens (YAG-1 to YAG-4). The beam envelope was kept nearly uniform, except in the main section between quadrupole lenses TRIPLET-1 and TRIPLET 2 where it was focused to a narrow waist in the center of the free drift section between the triplets (the chicane in the drawing was turned off). An electronic signal proportional to the photon number of integrated OTR emission from CTR-1 was measured using a CCD camera. Independently, similar reference measurement was carried out at CTR-0 prior to the collective interaction drift region.

beam transport line (Figure 6.1). For reference, the OTR signal was measured independently also on a screen CTR-0 preceding the drift section.

## 6.2 Experimental Method

The experimental setup is presented in Figure 6.1. The e-beam, that was generated in a photocathode by ultra-fast pulses ( $t_{pulse}=5\text{ pS}$ ) of a Nd-Yag laser, was accelerated by an RF-LINAC to beam energies 70, 64, 57 and  $50\text{ MeV}$ . It was accelerated at on-crest phase in order to avoid chirped energy variation along

the beam. The noise measurements were carried out by recording the integrated OTR radiation from the beam in screen CTR-1, positioned 6.5 *m* after the LINAC exit. The beam was drifted freely between two quad triplets (QUAD-1, QUAD-2) which focused the beam, and were readjusted for different beam energies. A reference OTR measurement was done in a separate setting (CTR-0), just after the LINAC exit, showing lack of noise suppression effect at this point.

In order to control the collective micro-dynamic process we varied the plasma phase  $\phi_p$  by varying the beam charge  $Q_b$  in 50 equal increments (in the reference measurement 8 increments) between 0.2-0.5 *nC* in each of the four beam energy experiments. The photo-cathode current was varied by attenuating the incident laser beam using variable angle crossed polarisers. This method made it possible to fix the OTR screen and camera at the same position in all experiments, and enabled stable comparative data collection in all experiments.

There was no change in the beam spot dimensions as the beam charge was varied in the range 200-500 *pC*. As the acceleration energy was varied, the beam spots on the screens were readjusted and kept small by controlling the two quad triplets. We used a (Basler) scA-1400 CCD camera equipped with a (Nikkor) macro lens (100 mm F/#=2.8) in order to obtain 1:1 image magnification of the OTR Copper screen (CTR-1). The screen was placed at 45° to the beam line.

The current noise measurement is based on its proportionality to the integrated OTR photon number, measured by integrating all the pixels using a frame grabber. The camera aperture opening angle, operating in screen imaging mode, was wide enough to collect the entire OTR radiation lobe (of opening angle  $\sim 4/\gamma$ ) in all experiments. The photographed 1:1 image of the OTR spot on the 11 *mm* (diagonal size) CCD chip was small enough to assure full collection of photons in the measured wavelengths range. Since the optical spectrum of the

noise (and the OTR photons) is quite uniform in the spectral range of the camera sensitivity ( $\lambda=0.4-1\mu m$ ), and the integrated OTR photon number is only weakly (logarithmically) dependent on the beam energy [45], the proportionality factor between the measured integrated pixels charge,  $S_{OTR}$  and the current noise power within the measured spectral range, was nearly the same for all experiments.

The quad currents were varied as the beam acceleration energy was changed, in order to focus the beam within the drift section, and keep the beam spot well within the camera frame in all experiments. The beam spots on screens YAG-1 to YAG-4 were recorded. In order to evaluate the beam profile dimensions along the drift section for different acceleration energies, a 3D numerical code simulation with space-charge effects (General Particles Tracer - GPT) [31] was used.

### 6.3 Experiment Results

The measured signal  $S_{OTR}$  was the integrated charge accumulated in all the pixels of a CCD camera exposed to the OTR emission upon the incidence of single micro-bunch e-beam pulses on the screen. The measured data of  $S_{OTR}/Q_b$  in CTR-0 and CTR-1 is shown in Figure 6.2 as a function of the varied bunch charge  $Q_b$  in the range 200-500  $pC$ . The pulse duration in all experiments remained approximately the same (5  $pS$ ) corresponding to average current 40-100  $A$ .

In a shot-noise dominated beam, in the absence of collective micro-dynamics, the current noise and consequently  $S_{OTR}$  are proportional to  $I_b$  [7]. Our measured data of  $S_{OTR}/Q_b$  in CTR-0 lies approximately on a horizontal line, confirming absence of collective micro-bunching and current-velocity noise correlation or noise suppression before this point. On the other hand, the data measured on CTR-1 displays systematic drop as a function of charge (200-500  $pC$ ) for all beam

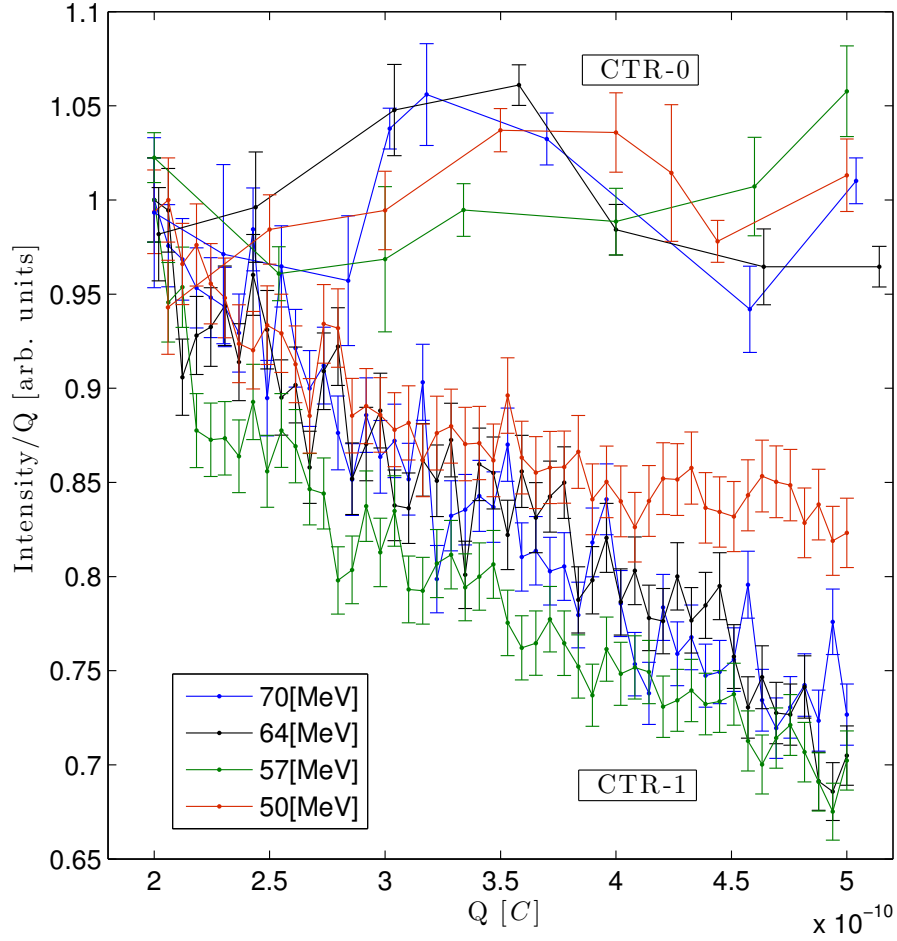


Figure 6.2: Integrated OTR intensity measurement signals divided by the electron pulse charge. The CTR-1 data corresponds to OTR measurement from a screen, intercepting the e-beam 6.5 m away from the LINAC exit. The curves negative slope indicates relative current shot-noise suppression of 20%-30% as the beam charge varies from 0.2-0.5 nC at different beam energies (50-70 MeV). The CTR-0 data corresponds to OTR measurement right after the LINAC exit. Used for reference, its horizontal slope (linear scaling of  $S_{OTR}$  with beam charge) indicates that there was no charge suppression prior to the collective micro-dynamic process in the subsequent drift section. The error of the camera integrated signal measurement - 3%, was determined from the variance in the value of the signal due to pulse-to-pulse variation, measured repeatedly while keeping all beam control parameters fixed. The charge measurement error is 1%.

energies (50-70  $MeV$ ). Since the measurement conditions at the two measurement positions and at different beam energies could not be made identical, the absolute suppression level between the two points could not be determined. However, the normalized data of all measurements of noise per unit charge depicted in Figure 6.2, shows the scaling with charge for all beam energies. It demonstrates attainment of 20%-30% relative noise suppression, and confirms the predicted effect of collective micro-dynamic noise suppression process in the drift section.

### 6.3.1 Interpretation of the Experimental Results

Beyond observation of noise suppression, interpreting the measured data and the noise suppression rate in terms of a simple theoretical model would be very crude. For  $N^2 \ll 1$  the 1D theoretical model predicts maximum suppression by a factor  $N^2$  at  $\phi_p = \pi/2$  but this is only true for uniform beam transport. In the present transport configuration the beam was focused to a tight waist in the section between triplet 1 and triplet 2 (the location of the turned-off chicane).

According to a theorem of Gover and Dyunin [7], a plasma phase increment  $\phi_p = \pi/2$  is accumulated along a beam waist, but this applies only if the beam transport is fully space-charge dominated. This is not the case when the beam angular spread due to emittance and beam focusing is significant, which compromises the collective micro-dynamic noise suppression process. Solution of the more general equations (2.28) under conditions of varying beam cross-section and increased angular spread (the focusing at triplet 1 at different beam energies led to rather high values of  $N^2$ : 0.3 - 0.8) shows that the noise suppression expected in a model configuration similar to the present experimental configuration is substantially smaller than anticipated in the uniform beam model (will be explained more thoroughly in 6.4).

This model calculation also shows that the observed weak dependence of the relative suppression rate on the beam energy is consistent with the experimental conditions (the down scaling of  $\omega_{pl}$  with  $\gamma^{3/2}$  is offset by the increased current density) and with a point of view that in the beam rest frame the beam envelope expansion and the charge homogenization effects are related.

Other reasons that can reduce the collective micro-dynamic suppression rate may be 3-D effects and excitation of higher order Langmuir plasma waves of different wavenumber values  $\theta_{pr}$  [9]. These and other deviations from ideal conditions can explain why the relative noise suppression effect in the range of charge variation (200-500 pC) is quite modest (20%-30%).

## 6.4 Computational Model Analysis for Experimental Observation of Optical Current Noise Suppression Below the Shot-Noise Limit

At the exit of the Linac, the beam is current-noise dominated, and  $N^2 \ll 1$ . However, due to finite emittance, the axial velocity spread becomes significant as the beam is focused and consequently  $N^2$  (Eq (2.74)) is no longer negligible. Furthermore, at tight focusing the uniform beam expression (Eq. (2.38)) cannot be used and in order to calculate the noise suppression, one should solve differential equations for variable beam parameters.

In this section we show through a model case computational solution of equations (2.31) and (2.32), that the axially varying beam cross section and the excess axial velocity spread due to angular spread can account for a substantial moderation of the noise suppression effect that was realized in the experiment. This example also explains some parameter scaling features of the measurement data.

We turn to the coupled current and kinetic voltage equations (2.24) and (2.25). This set of equations can be solved explicitly numerically if  $A_e(z) = 2\pi\sigma_x(z)\sigma_y(z)$  is given, and the initial conditions  $\check{i}(0, \omega), \check{v}(0, \omega)$  are specified, and the solution at the end of the drift section  $L$  is a linear combination of the initial conditions:  $\check{i}(L, \omega) = A(L)\check{i}(0, \omega) + B(L)\check{v}(0, \omega)$ . Assuming that the current modulation noise and the focusing enhanced velocity noise are uncorrelated at  $z = 0$ , we set

$$\overline{|\check{i}(L, \omega)|^2} = |A(L)|^2 \overline{|\check{i}(0, \omega)|^2} + |B(L)|^2 \overline{|\check{v}(0, \omega)|^2} \quad (6.1)$$

$$\overline{|\check{i}(0, \omega)|^2} = eI_b \quad (6.2)$$

$$\overline{|\check{v}(L, \omega)|^2} = \left( \frac{mc^2}{e} \gamma_0 \beta_0 \right)^2 \frac{e}{I_0} \sigma_{\beta z}^2 \quad (6.3)$$

To compute the noise evolution for the parameters of the reported experiment it is necessary to estimate the cross section dimensions  $\sigma_x(z), \sigma_y(z)$  along the interaction length. This was done based on the measurements on screens YAG-1 to YAG-4, the recorded quad excitation parameters, and performing full 3-D simulation (with space-charge) using GPT.

The beam axial velocity spread due to energy spread ( $\Delta E \simeq 3 \text{ KeV}$ ) is small, and its effect on the initial velocity noise is negligible. We assume that the initial velocity noise is determined by the standard deviation of the axial velocity spread (equation (6.3)), which was calculated for each quad setting from the angular spread standard deviations due to the focusing and emittance ( $\epsilon_x, \epsilon_y \sim 2 - 5 \mu\text{m}$ ):

$$\sigma_{\beta z} = \frac{1}{4} (\sigma_{\beta x}^2 + \sigma_{\beta y}^2) \quad (6.4)$$

The coefficients  $A(z = L), B(z = L)$  were computed by iterative integration of

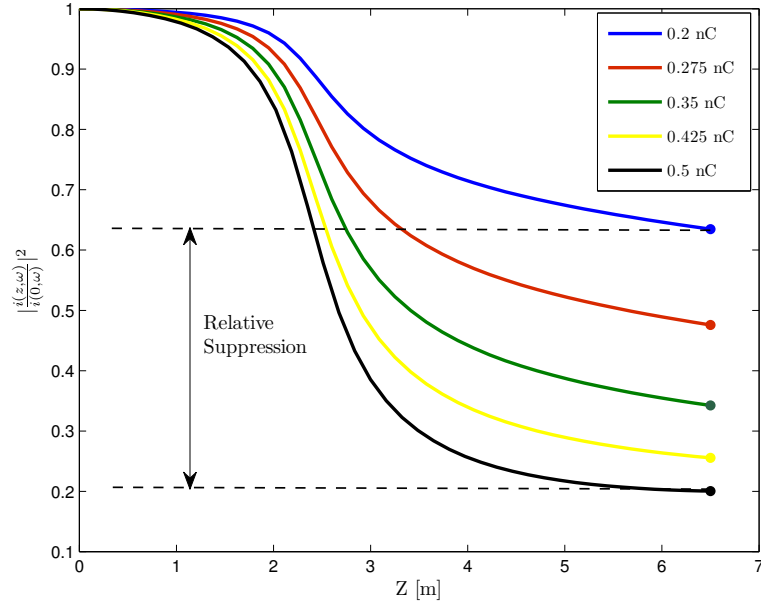


Figure 6.3: Noise suppression along the collective interaction region as calculated from solution of the coupled differential equations with  $\sigma_x(z)$ ,  $\sigma_y(z)$  of 70 MeV.

the coupled linear differential equations 2.31 and 2.32, with the initial conditions (6.3). Figures 6.3 and 6.4 display the results of the model computation of the variable parameters differential equations. The curves show the noise suppression as function of drift distance  $z$  and of the beam current  $Q$  for the two extreme energy cases of  $E=50$  MeV and 70 MeV. The relative suppression rate in the range  $Q_b=0.2-0.5$  nC at the drift section exit  $L=6.5$  m is displayed in 6.5 for the two beam-energy examples.

Figure 6.5 can only be regarded as a model explanation for the reduced relative noise suppression effect observed in the experiment. As mentioned, there can be additional factors affecting the suppression rate. It is noted that the computed curves display significantly larger relative suppression in the range  $Q_b=0.2-0.5$  nC than the experimental curves, but in either case there is only little dependence on the acceleration energy. In the simple uniform beam model one would expect

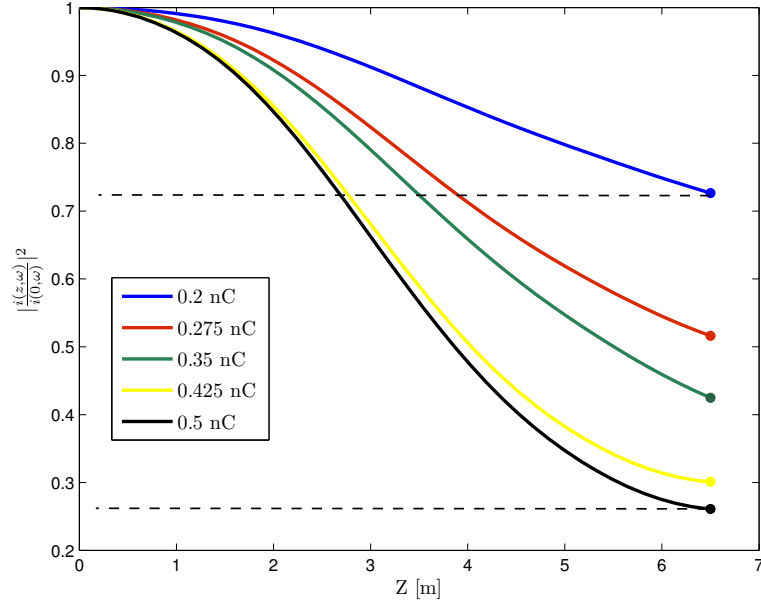


Figure 6.4: Noise suppression along the collective interaction region as calculated from solution of the coupled differential equations with  $\sigma_x(z)$ ,  $\sigma_y(z)$  of 50 MeV.

dependence of the noise suppression factor on the beam energy due to the 3/2 power dependence of the plasma frequency on  $\gamma$ , which corresponds to smaller plasma phase accumulation at higher beam energy. However, the beam envelope had to be varied in the experiment in different beam energies, and one must keep in mind, that at the higher energy the beam focuses into a tighter waist due to the reduced space charge effect. This tends then to increase the plasma frequency at the waist, where most of the microdynamic process takes place.

#### 6.4.1 Conclusions

This observation is consistent with the point of view that the beam envelope expansion and the beam charge homogenization process are in essence the same process of excess charge beam expansion when viewed in the beam rest frame

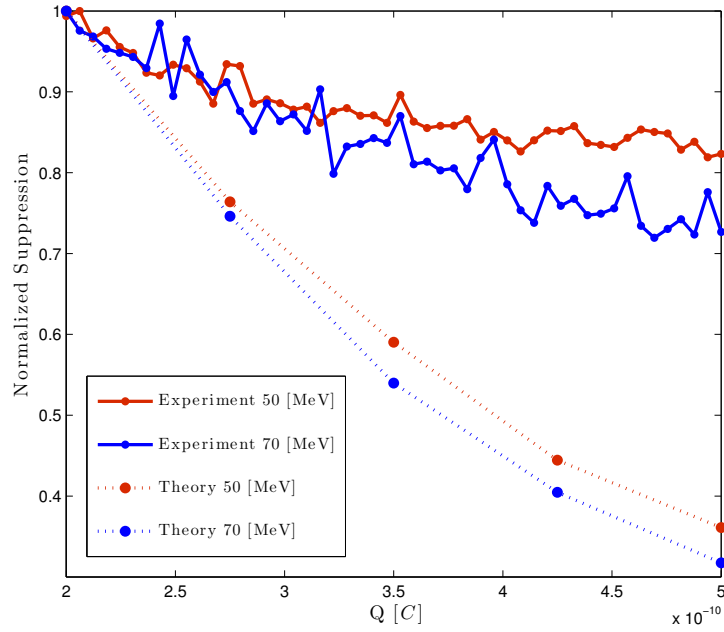


Figure 6.5: Relative noise suppression rate computed from Eq. 2.31 and 2.32 for  $E=50 \text{ MeV}$ ,  $70 \text{ MeV}$  compared to the experimental suppression results.

(independent of the acceleration energy). This is consistent with the plasma phase accumulation theorem of constant plasma phase accumulation in a space charge dominated beam waist [7]. This provides qualitative physical explanation for the weak dependence of the relative noise suppression on the beam energy in the 50-70  $\text{MeV}$  range, as depicted in both the experimental (figure 6.2) and model calculation (figure 6.5) curves.

## CHAPTER 7

### Appendix

#### 7.1 Current and Velocity Noise Parameters of a Particle Beam in General and in the Case of a Random Uncorrelated Beam

The fluid model amplitudes of the current and kinetic voltage (or density) modulation as a function of frequency, are derived here in the linear regime starting from a single particle model. The e-beam current consists of zero-dimensions discrete particles (neglecting quantum effects). We obtain the beam current as a function of axial coordinate ( $z$ ) and time ( $t$ ) by integration of the axial component of current density

$$\mathbf{J}(\mathbf{r}, t) = -e \sum_j u_{jz}(z) \delta(\mathbf{r} - \mathbf{r}_j(t)) \hat{\mathbf{e}}_z \quad (7.1)$$

over the beam cross section ( $dxdy$ ):

$$I(z, t) = -e \iint_{-\infty}^{\infty} \mathbf{J}(\mathbf{r}, t) \cdot \hat{\mathbf{e}}_z dxdy = -e \sum_j u_{jz}(z) \delta(z - z_j(t)) \quad (7.2)$$

where  $\delta$  is the Dirac delta function,  $z_j(t)$  and  $\frac{dz_j(t)}{dt} = u_{jz}$  are the axial coordinate and velocity of the  $j^{th}$  particle respectively. If  $z_j(t)$  is a single valued function of time, it can be inverted. Therefore,  $t_j(z)$  is the moment when the  $j^{th}$  electron crosses the plane  $z$ .

Thus, using the identity  $\delta(z - z_j(t))dz = \frac{1}{u_{jz}}\delta(t - t_j(z))dt$ , we obtain:

$$I(z, t) = \sum_j -e \cdot \delta(t - t_j(z)) \quad (7.3)$$

Likewise we derive an expression for the line particle density by integrating the particle 3-D density:

$$n(\mathbf{r}, t) = \sum_j \delta(\mathbf{r} - \mathbf{r}_j(t)) \quad (7.4)$$

over the beam cross section ( $dx dy$ ):

$$N(z, t) = \iint_{-\infty}^{\infty} \mathbf{n}(\mathbf{r}, t) dx dy = \sum_j \delta(z - z_j(t)) = \sum_j \frac{1}{u_j(z)} \delta(t - t_j(z)) \quad (7.5)$$

By using a Fourier transform, we obtain the current and density spectra:

$$\begin{aligned} \check{I}(z, \omega) &= \sum_j \int_{-\infty}^{\infty} -e \delta(t - t_j(z)) \exp(i\omega t) dt = \sum_j -e \exp(i\omega t_j(z)) \\ \check{N}(z, \omega) &= \sum_j \int_{-\infty}^{\infty} \frac{1}{u_j(z)} \delta(t - t_j(z)) \exp(i\omega t) dt = \sum_j \frac{1}{u_j(z)} \exp(i\omega t_j(z)) \end{aligned} \quad (7.6)$$

The fluid-plasma equation for the beam current is:

$$I(z, t) = -e[N_0(z) + N(z, t)][u_{0z}(z) + u_z(z, t)] \quad (7.7)$$

Our theoretical analysis is based on a small signal (linear) model. It means that we express all parameters as the sum of two terms: a time-averaged term and a time-varying term whose amplitude is much smaller than the time-averaged

one. Thus, the beam current is presented by the linearised expression:

$$I(z, t) \simeq -eN_0(z)u_{0z}(z) - e(N(z, t)u_{0z}(z) + N_0(z)u_z(z, t)) \quad (7.8)$$

where  $N_0$  and  $u_{0z}$  are the time-average (DC) linear density of particles and axial velocity of the beam respectively,  $N$  and  $u_z$  are the time-varying (AC) density and the axial velocity of the beam respectively.

The velocity of the beam at a space point is defined as an average velocity of all electrons in a physically small space volume around the point. It is found from the beam particle kinetic distribution function (first moment of the distribution function). Thus, the time-varying axial velocity ( $u_z$ ) is the temporal variation of the first moment.

The small signal current of the beam in the frequency domain is the Fourier transform of the two last terms in equation (7.8):

$$\check{I}(z, \omega) = -e(\check{N}(z, \omega)u_{z0}(z) + N_0(z)u_z(z, \omega)) \quad (7.9)$$

At this point we can use the spectral expressions for the single particle model current and density (7.6) in the linearised spectral equation for the fluid model current (7.9) and derive an expression for the velocity spectrum:

$$\begin{aligned} \check{u}(z, \omega) &= \frac{\check{I}(z, \omega) + \check{n}u_0eA_e}{-eA_en_0u_0}u_0 = \frac{\check{I}(z, \omega) + eu_0 \sum_j \frac{1}{u_j(z)} \exp(i\omega t_j(z))}{I_0}u_0 = \\ &= \frac{e}{I_0} \sum_j \frac{(u_j(z) - u_0(z))}{u_j(z)} u_0(z) \exp(i\omega t_j(z)) \quad (7.10) \end{aligned}$$

We represent the velocity of each particle ( $u_j(z)$ ) as the sum of the average velocity ( $u_0$ ), and the particular particle deviation velocity ( $\delta u_j$ ) from the ensemble

average:  $u_j = u_0 + \delta u_j$  when  $\langle \delta u_j \rangle = 0$ . Substituting this into our previous result (7.10), assuming that the particular particle deviation velocity is small compared to the average velocity ( $|\delta u_j| \ll u_0$ ), we can write:

$$\check{u}(z, \omega) = \frac{e}{I_0} \sum_j \left( \delta u_j - \frac{(\delta u_j)^2}{u_0} \right) \exp(i\omega t_j(z)) \quad (7.11)$$

Here we kept the second order term and neglected higher order terms. Note, the beam current spectrum (7.6) depends on the random crossing time  $t_j(z)$  of each particle, whereas the spectrum of the beam velocity (7.11) depends on both the random crossing time  $t_j(z)$  of each particle and its random velocity deviation from the average  $\delta u_j$ .

The spectral density of the product of two random signal parameters ( $\check{X}(\omega)$  and  $\check{Y}(\omega)$ ) is defined as the average over an ensemble of the product  $\check{X}(\omega)\check{Y}^*(\omega)$ . For an ergodic stationary system, the average of the ensemble may be replaced by an average over time ( $T$ ):

$$\overline{\check{X}\check{Y}^*} = \frac{1}{T} \langle \check{X}\check{Y}^* \rangle_T \quad (7.12)$$

where  $T$  is larger than the coherence time of the signal.

All the spectral equations above are valid for propagation of coherent signal modulation of the beam as well as for random modulation (noise).

Let us assume now that the crossing times of electrons ( $t_j(z)$ ) are statistically independent random variables at a plane  $z$ , namely, the crossing times of all electrons are uncorrelated (for example, this is the case at the cathode plane). Using (7.12) to obtain the spectral density of the current of a random particle

beam, we obtain the familiar "shot-noise" formula:

$$\overline{|\check{i}(\omega)|^2} = \frac{\langle |\check{I}(\omega)|^2 \rangle_T}{T} = \frac{1}{T} \left| \sum_j -e \exp(-i\omega t_j(z)) \right|^2 = e \frac{eN_T}{T} = -eI_0 \quad (7.13)$$

where  $N_T$  is the total number of electrons crossing the plane  $z$  within time  $T$ . The conventional definition of shot-noise relates to positive frequencies only, and therefore is twice as large ( $-2eI_0$ ). The sign minus here demonstrates that if an electron moves to  $+z$  direction, then the current  $I_0$  is negative.

The same procedure is applied to the velocity spectrum (7.11) assuming also that the electron velocity deviations  $\delta u_j$  are statistically independent random variables (uncorrelated), and also are independent of their crossing times  $t_j$ . Keeping only second order terms in  $\delta u_j$  this results in:

$$\overline{|\check{u}(\omega)|^2} = \frac{\langle |\check{u}(\omega)|^2 \rangle_T}{T} = \frac{e^2}{I_0^2} \frac{1}{T} \sum_j (\delta u_j)^2 = -\frac{e}{I_0} (u_{th})^2 \quad (7.14)$$

where  $u_{th}$  is the velocity spread defined from the beam velocity distribution:

$$u_{th} = \sqrt{\frac{1}{N_T} \sum_j (\delta u_j)^2} \quad (7.15)$$

and  $N_T = TI_0/e$ .

Using this result, we define the spectral density of the kinetic voltage (see equation (2.7) in the article) in the frequency range  $-\infty < \omega < \infty$  for an e-beam with velocity spread as:

$$\overline{|\check{v}(\omega)|^2} = \frac{\langle |\check{v}(\omega)|^2 \rangle_T}{T} = -\left(\frac{m_0 c}{e} \gamma_0^3 \beta_0\right)^2 \frac{e}{I_0} (u_{th})^2 \quad (7.16)$$

It is important to note that the thermal distribution of the electrons ( $\delta u_{th}$ )

defines the kinetic voltage noise only at the plane where velocity deviations of all electrons are uncorrelated with their crossing times  $t_j$ . Note also that in the case where the electron axial velocity spread originates from the beam energy spread, they are related by:

$$\delta\gamma = \gamma_0^3 \beta \delta\beta \quad (7.17)$$

where  $\delta\beta = u_{th}/c$ . We can then write an expression for the spectral "energy-noise":

$$\overline{|\delta\check{\gamma}(\omega)|^2} = \left(\frac{e}{mc}\right)^2 \overline{|\check{v}(\omega)|^2} = -\frac{e}{I_0} (\delta\gamma)^2 \quad (7.18)$$

The kinetic voltage spectral noise parameter  $\overline{|\check{v}(\omega)|^2}$  (7.16) and the energy noise parameter  $\overline{|\delta\check{\gamma}(\omega)|^2}$  (7.18), depend on the energy spread, but these are definitely different characteristic parameters of the beam, and have different units.

## 7.2 The Bunching Factor of an Electron Beam

The electric field of a beam of  $N$  particles is the summation of the single particle field contributions. For simplicity we handle here only a case of a finite cross section beam of electrons, all propagating in parallel to the beam axis (zero emittance beam). Extension to a finite emittance beam is quite straight forward.

In Cartesian coordinates we write:

$$\check{\mathbf{E}}(x, y, z = 0) = \sum_{j=1}^N \check{\mathbf{E}}_e(x - x_i, y - y_i, z = 0) e^{i\omega t_{0j}} \quad (7.19)$$

In the far field (Fraunhofer) zone, the transverse electric field component can

be written [38] as:

$$\check{E}_x(x, y, z, \omega) = \frac{-i}{\lambda z} e^{i \frac{\pi}{\lambda z} (x^2 + y^2)} \iint e^{i \frac{\pi}{\lambda z} (xx' + yy')} \check{E}_x(x', y', 0, \omega) dx' dy' \quad (7.20)$$

$$\check{E}_y(x, y, z, \omega) = \frac{-i}{\lambda z} e^{i \frac{\pi}{\lambda z} (x^2 + y^2)} \iint e^{i \frac{\pi}{\lambda z} (xx' + yy')} \check{E}_y(x', y', 0, \omega) dx' dy' \quad (7.21)$$

The bunching parameter of an electron beam  $M_b(\theta_x, \theta_y, \omega)$  (4.12) that was defined in section 4.2 is a property of the beam that can be useful for characterising its radiation field in the far field zone. Here we show its derivation for any radiative emission scheme from free electron using a general optical diffraction formulation in the paraxial far field (Fraunhofer) zone [38].

If we substitute the components of equation (7.25) in the integrands we obtain (here for  $E_x$  only):

$$\begin{aligned} \check{E}_x(x, y, z, \omega) &= \frac{-i}{\lambda z} e^{i \frac{\pi}{\lambda z} (x^2 + y^2)} \iint e^{-i \frac{2\pi}{\lambda z} (xx' + yy')} \sum_{j=1}^N \check{E}_{xj}(x' - x_j, y' - y_j) e^{i\omega t_{0j}} dx' dy' = \\ & \frac{-i}{\lambda z} e^{i \frac{\pi}{\lambda z} (x^2 + y^2)} \sum_{j=1}^N e^{-i \frac{2\pi}{\lambda z} (xx_{0j} + yy_{0j}) + i\omega t_{0j}} \iint e^{-i \frac{2\pi}{\lambda z} (xx'' + yy'')} \check{E}_{xj}(x - x'', y - y'') dx'' dy'' \end{aligned} \quad (7.22)$$

where we substituted  $x'' = x' - x_j$ .  $y'' = y' - y_j$  as integration variables. Obviously the far-field of the beam can be written as a product of the far-field of a single electron and a bunching factor:

$$\check{E}_x(x, y, z, \omega) = NM_b(\theta_x, \theta_y, \omega) \check{E}_{ex}(x, y, z, \omega) \quad (7.23)$$

$$\check{E}_y(x, y, z, \omega) = NM_b(\theta_x, \theta_y, \omega) \check{E}_{ey}(x, y, z, \omega) \quad (7.24)$$

where  $M_b$  is the complex bunching factor or "form factor" of the beam:

$$M_b(\theta_x, \theta_y, \omega) = \frac{1}{N} \sum_{j=1}^N e^{-ik(\sin \theta_x x_{oj} + \sin \theta_y y_{oj}) + i\omega t_{oj}} \quad (7.25)$$

where  $k = \frac{2\pi}{\lambda}$  and we define  $\sin \theta_x = \frac{x}{z}$ ,  $\sin \theta_y = \frac{y}{z}$  and  $\check{\mathbf{E}}_e(x, y, z, \omega)$  is the far field diffraction field of a single electron.

Note that this definition of the bunching factor parameter is properly used for calculation of radiation emission only in the far field zone. In other diffraction zones one must keep the general free space Green function (equation (4.47) for the case of OTR). Only in the far zone the integration of the Green functions over the sources (or their radiation fields at some plane) reduces into a spatial Fourier transform and the emission can be characterised in terms of the compact expression for the bunching parameter (7.25).

## 7.3 Numerical Computation Tools

This work included numerical computations mostly using two softwares: General Particle Tracer (GPT) and Matlab. GPT was used to simulate an electron beam, including 3D point to point Coulomb interactions, using a relatively large number of sample particles. In these simulations we can change various beam parameters such as pulse duration and charge, emittance and energy spread and various beam distributions both in the axial and transversal dimensions.

Matlab scripts were used in order to calculate noise suppression conditions according to the 1D model - including the validity conditions of the model, and to perform the analysis of the simulations results. It was also used sometimes to create the initial macro-particles distributions which were then imported to GPT for the simulations. these main uses will be presented in this section, including some of the codes.

### 7.3.1 GPT simulations

The General Particle Tracer (GPT) code is a simulation platform for the study of charged particle dynamics in electromagnetic fields. The code is completely 3D, including the space-charge model. GPT can be customized without compromising its ease of use, accuracy or simulation speed.

The GPT executable starts by reading one or more ASCII inputfile(s) describing the simulation to perform. These files are marked as *\*.in* files. The input file specifies the initial particle distribution, the 3D electromagnetic field configuration (set-up), the required accuracy of the calculations and the output method. The initial particle distribution consists of a number of macro-particles, each typically representing a large number of elementary particles. Hammersley

sequences are employed to minimize statistical errors due to the finite number of particles. Each projection of the initial distribution can be specified using built-in particle generators or can be read from an external file. Complicated particle distributions can consist of any number of separate particle distributions, each having their own distribution in position-momentum space.

In this work I used mainly flat and Gaussian axial and transverse distributions, included beam emittance and energy spread. Below is an exemplary input file, used for a rest frame simulation according to the SPARC parameters (including few quads as well). I will describe in short its major commands which define the simulation properties. For more info one can use the GPT manual available in [31].

The *basic beam parameters* section is where the beam parameters such as energy and pulse length are inserted as described in the code. In the *simulation parameters* section we define parameters such as the number of macro-particles in the simulation, and more advanced ones such as electron-optics elements (quads in this simulation) strengths and physical lengths. The *start bunch* section is used to command the software to create the pulse using the *setparticles* (or *setstartpar* and more) and define the distributions along its different axes. Here we define a randomly uniform distribution (to use equally spaced particles we use the "u" option instead of " $\sim u$ ") in  $r$  (cylindrical coordinates) and uniform in  $\phi$  from 0 to  $2\pi$  using the *setdist* command. We also define the average of  $\gamma$  (here it is set to one - rest frame simulation) and its distribution/spread. Space charge algorithm is chosen here to be a full 3D algorithm. The next lines are setting the quads in their locations using a "wcs" coordinate system (in which  $z$  points towards the axial dimension and  $x$  and  $y$  are the transverse coordinates) - the location on the  $z$  axis, and define their strengths and dimensions using the pre-defined variables

```

# SPARC Simulation in rest Frame
#=====
# Basic beam parameters
#=====
randomize();
Eo = 100e6 ; # Energy [eV]
G = 1+|qe|*Eo/(me*c^2) ; # Corresponding Lorentz factor G
dG = (G-1)/1e4;
Beta = sqrt(1-G^-2) ; # Corresponding normalized velocity
sigx = 450e-6 ; # Initial x Bunch sigma [m]
sigy = 450e-6 ; # Initial y Bunch sigma [m]
T = 5.7e-12 ; # Bunch Duration [m]
zlen = c*T*G ; # Bunch Length [m]
Qtot = -0.37e-9 ; # Total charge in tlen [C]
#=====
# Simulation parameters
#=====
nps = 15e4 ; # Number of macro-particles
Ld = 16; # Drift length for minimal noise
V = zlen * 2*pi * sigx * sigy ; # Pulse volume [m^3]
n = nps / V;
eps = 0.1 * n^-(1/3); # Space-charge coefficient

Q11_K1 = 0; # 1/m^2 1st triplet
Q12_K1 = 0; # 1/m^2
Q13_K1 = 0; # 1/m^2

Q21_K1 = 0; # 1/m^2 2nd triplet
Q22_K1 = 0; # 1/m^2
Q23_K1 = 0; # 1/m^2

Q1_K1 = 0; # 1/m^2
Q2_K1 = 0; # 1/m^2
Q3_K1 = 0; # 1/m^2
Q4_K1 = 0; # 1/m^2
Q5_K1 = 0; # 1/m^2

Qt_LEN = 0.172; # Quad length (short)[m]
Q_LEN = 0.54; # Quad length [m]

Q11_STR = G*me*c*Q11_K1/qe; # Quad strength [T/m]
Q12_STR = G*me*c*Q12_K1/qe; # Quad strength [T/m]
Q13_STR = G*me*c*Q13_K1/qe; # Quad strength [T/m]

Q21_STR = G*me*c*Q21_K1/qe;
Q22_STR = G*me*c*Q22_K1/qe;
Q23_STR = G*me*c*Q23_K1/qe;

Q1_STR = G*me*c*Q1_K1/qe;
Q2_STR = G*me*c*Q2_K1/qe;
Q3_STR = G*me*c*Q3_K1/qe;
Q4_STR = G*me*c*Q4_K1/qe;
Q5_STR = G*me*c*Q5_K1/qe;
#=====
# Start bunch
#=====
setparticles("beam",nps,me,qe,Qtot) ;

#setxdist( "beam", "g", 0, sigx , 1, 1 ) ;
#setydist( "beam", "g", 0, sigy , 1, 1 ) ;
setxydist( "beam", "~u", sigx/2, sigx ) ;
setphidist("beam", "~u", 0, 2*pi) ;
setzdist("beam", "~u", zlen/2, zlen ) ;
#setGdist("beam", "~u", 1, dG ) ;
#=====
# Space-charge
#=====
spacecharge3Dtree(eps, 0.3, 1) ; # Space-charge 3D algorithm
#=====
# Set-up
#=====
quadrupole("wcs", "z", 0.363, Qt_LEN, Q11_STR);
quadrupole("wcs", "z", 0.614, Qt_LEN, Q12_STR);
quadrupole("wcs", "z", 0.861, Qt_LEN, Q13_STR);

quadrupole("wcs", "z", 4.132, Qt_LEN, Q21_STR);

```

```

quadrupole("wcs", "z", 4.383, Qt_LEN, Q22_STR);
quadrupole("wcs", "z", 4.634, Qt_LEN, Q23_STR);

quadrupole("wcs", "z", 8.014, Q_LEN, Q1_STR);
quadrupole("wcs", "z", 10.574, Q_LEN, Q2_STR);
quadrupole("wcs", "z", 13.134, Q_LEN, Q3_STR);
quadrupole("wcs", "z", 15.694, Q_LEN, Q4_STR);
quadrupole("wcs", "z", 18.254, Q_LEN, Q5_STR);
#=====
# Output
#=====
tout(0, 1.5*Ld/c/G, Ld/c/50/G);

```

$Q\_LEN$  and  $Q\_STR$ . Finally, we define the output times required. Here we ask the simulation to run from  $t = 0$  to  $t = 1.5t_{Ld}$  where  $t_{Ld}$  is the drift length for  $16m$ , with 50 equally spaced increments.

In the case of a bend, a transformation matrix is required in order to export the particles coordinates relative to the propagation direction of the beam. In order to do so, a rotation matrix is used to re-define the coordinate system used. We show next, a code section which simulates a simple bend using the LCLS dog-leg bend which constructs of two bending magnets (*sectormagnet* command in GPT) and a quadrupole magnet between them. The *ccs* command is what defines the new coordinate system and it is divided into three sections: before the bend, during the first bend ("bend") and during the second bend ("bend2"). For each we define a new coordinate matrix according to the pre-defined angle of the bend. Physical location and strength of the magnetic field are defined in the simulation as well. Note that three different time outputs are exported here which include the particles coordinates in each section relative to the propagation direction of the electron beam.

Operation of the simulations is done using a batch file. This file also performs the transformation of the simulation data to an ASCII file including the required data. This is used to perform an analysis using another program such as Matlab.

```

#=====
#                                     bend
#=====
Bfield = +0.67 ;
angle = -0.305432619 ;
phiin = 0 ;
phiout = 0 ;
fuzz = 0.59 ; # You could usu GDFsolve for this.
Rbend = fuzz * (-me*c*G*Beta/(qe*Bfield)) ;
pp(Rbend) ;
dl = 0 ;
b1 = 10 ;
b2 = 0 ;
#=====
ccs("wcs", 0, 0, 7.4, cos(angle), 0, -sin(angle), 0, 1, 0, "bend") ;
sectormagnet("wcs","bend", Rbend, Bfield, phiin/deg, phiout/deg, dl, b1, b2) ;

quadrupole("bend", "z", 0.83, QB_LEN, QB_STR);

ccs("bend", 0, 0, 1.68, cos(angle), 0, -sin(angle), 0, 1, 0, "bend2") ;
sectormagnet("bend","bend2", Rbend, Bfield, phiin/deg, phiout/deg, dl, b1, b2) ;
#=====
#                                     More Quads
#=====

quadrupole("bend2", "z", 0.51, QM03_LEN, QM03_STR);

quadrupole("bend2", "z", 0.92, QM04_LEN, QM04_STR);

#=====
# Output
#=====

tout(0, 0.6*Ld/c, Ld/c/50);
tout(0.72*Ld/c, 0.78*Ld/c, Ld/c/50, "bend");
tout(0.9*Ld/c, Ld/c, Ld/c/50, "bend2");

```

The output file of GPT (*\*.gdf*) can be used to check results and plot the results as a simple 2D plots. One can also export a file containing the plots obtained as a video file. For more info read [31].

### **7.3.2 Matlab scripts**

#### **7.3.3 1D model suppression tool**

This program includes a GUI (user interface) for the estimation of the noise suppression parameters from an electron beam by inserting the beam parameters based on the analytic expressions of chapter 2. The input parameters are beam energy, charge, radius, pulse duration, wavelength (of noise) emittance and energy spread (sliced). The tool calculates the 1D model validity conditions and noise suppression parameters according to chapter 2. Its use is demonstrated in figure 3.13 for the LCLS beam parameters. Matlab code file name is (Noise\_reduction\_conditions.m).

##### **7.3.3.1 Noise suppression**

Many different Matlab scripts were used in this work, and not all of them can be covered here, but I will present few of the main ones. The first script demonstrates the use of GPT simulation results in order to calculate the current noise as a function of the propagation distance in the rest frame. The difference between a rest frame simulation to a lab frame simulation is mainly considered in the GPT simulation and its output. This code allows direct reading from an output file, choosing a specific section in the middle of the simulated bunch, filtering and slicing (if required) of the bunch and even creating an output video file of the results.

The noise is calculated for chosen frequencies, and the band resolution can be defined using the  $n$  variable. The *lambdamax* variable is the upper limit and the band is calculated according to the values of  $n$ . In this example  $n = 200 : 400$ . The band is the maximal value multiplied and divided by  $n$ , which results in a band of  $5 - 10\mu m$  with 200 increments. This method is used to allow us to use the same number of periods for different wavelengths in the case where we choose a specific section inside the pulse (200 of  $5\mu m$  periods total length is different than 200 periods of  $2\mu m$ ).

The function *GPT\_ASCII\_Read\_3D* imports a 3D simulation data (x y z coordinates) from an output of a GPT file. It basically cleans the titles, lines ext from the ASCII file to create a matrix of values instead. This matrix is then used to perform the analysis of the noise dynamics.

The function *NR\_filtered\_3D\_slice* is using the algorithm described in section 3.5 to spatially filter specific frequency band. This is done when one needs to create a movie which demonstrates the homogenisation process (a few snap-shots from it are shown in 3.5). This function is presented in this section as well. Its inputs are the particles coordinates in 3D, the required resolution in the transverse and axial dimension and the lower-upper limits of the wavelength band. The output is an z-x slice density image *n\_xz\_final*.

### 7.3.3.2 OTR from a single electron and from a beam

The function *single\_otr\_xy.m* calculates OTR from a single particle based on 4.3. The single particle function inputs are *lambda*: radiation wavelength, *dist*: distance to the measuring point, *x*, *y*: limits of the XY mesh that is used to calculate the image (their length will determine the image resolution), *nt\_res*: resolution of integration (number of elements in the line charge vector), *n\_ginz*:

```

%%%%%%%%%%%%%%%%%%%%%%%%%%%%%%%%%%%%%%%%%%%%%%%%%%%%%%%%%%%%%%%%%%%%%%%%
% This program imports results from GPT and calculates noise dynamics in
% rest frame and can create a video file as well
%%%%%%%%%%%%%%%%%%%%%%%%%%%%%%%%%%%%%%%%%%%%%%%%%%%%%%%%%%%%%%%%%%%%%%%%
%-----
%Constants
%-----
c=3e8;%m/S
me=9.11*10^-31;%Kg
e=1.6e-19;
eps=1/(c*120*pi);
%-----
% Pulse Parameters
%-----
Ek = 70e6;
gamma = Ek*e/(me*c^2)+1;
beta = sqrt(1-1/gamma^2);
vz0 = beta*c;
sigma = 500e-6;
Rb = 500e-6; %sqrt(2)*sigma;
dE = 5e3;
en = 2e-6;
pulse_duration = 2e-12; %Seconds. in lab frame
charge = 0.2e-9;
pulse_length = pulse_duration*c*gamma; %in rest frame
I = charge/pulse_duration;

% textfile=load('/Users/Ariel/Documents/Simulations/Rest_Frame/Work_archive/shot_noise43_full.txt');

%-----
% Analysis Parameters
%-----
Ld = 10;
ddist = 400; % step size in distance at Ld units
dist = (0 : Ld/ddist : Ld); % beam propagation in lab frame
parnum = 60000; % number of m.particles
lambdamax = 10*1e-6; % modulations max wave length
num_periods = 10; % Number of periods from center to each direction
pulse_length = pulse_duration*c*gamma; % in rest frame
pulse_charge = I*pulse_duration; % C
num_electrons = pulse_charge/e; % number of electrons in one pulse
electrons_in_macro = num_electrons/parnum; % electrons per macro particle
macro_charge = electrons_in_macro*e; % charge of single macro particle

%-----
% Importing the text data from GPT simulation
%-----
% mat1 = GPT_ASCII_Read_3D(parnum);
N = size(mat1,2);
n = 200:1:400; %defines the number of noise differential elements
%-----
% Creating figure and define parameters
%-----
xres = 300;
zres = 300;
density_res = 150;
n_xz_max = 0;
n_xz_min = 0;
noise_max = 0;
ymin = -0.1e-3; % Determines the slice size in y coordinate
ymax = 0.1e-3;
X0 = zeros(length(dist), (xres+1));
n_xz_final = zeros(length(dist), xres+1, zres+1);
%-----
% Noise calculations and filtered density
%-----
for t = 1:length(lambdamax)
    lambda = lambdamax(t)*n(1)./n;
    k = 2*pi./lambda;
    omega = 2*pi*c./lambda;
    current_noise = zeros(length(k),length(dist));
    int_current_noise = zeros(length(t), length(dist));
%-----
% Determine boundaries
%-----
m = 0;
for j = 1:3:N
    j
    m = m+1;
    z_tag = mat1(:,j + 2);
    x_tag = mat1(:,j);
    y_tag = mat1(:,j + 1);

    min_z = mean(z_tag) - num_periods * lambdamax(t) * gamma;
    %Defines size of z range to investigate
    max_z = mean(z_tag) + num_periods * lambdamax(t) * gamma;
    z_fil = z_tag.*(z_tag>min_z).*(z_tag<max_z); %z value filtered to required band
    y_fil = y_tag.*(y_tag>ymin).*(y_tag<ymax); %z value filtered to required band
end

```

```

ind = find(z_fil.*y_fil);
z_tag_fil = z_tag(ind);
x_tag_fil = x_tag(ind);
y_tag_fil = y_tag(ind);

current_noise_amp = exp(1i*k'*z_tag_fil'/gamma); % Calculating noise amplitude

current_noise(:,m) = (electrons_in_macro*e)^2/pulse_duration*abs(sum(current_noise_amp,2)).^2;
int_current_noise(t,:) = sum(current_noise,1); % summation of noise amplitudes
[x0, z0, n_xz] = NR_filtered_3D_slice( x_tag_fil, y_tag_fil, z_tag_fil ,xres, zres, min(lambda),
max(lambda)); % If filtering is needed

if max(max(n_xz)) > n_xz_max
    n_xz_max = max(max(n_xz));
end

if min(min(n_xz)) < n_xz_min
    n_xz_min = min(min(n_xz));
end

if max(max(int_current_noise(t,m))) > noise_max
    noise_max = max(max(int_current_noise(t,m)));
end

X0(m,:) = x0;
n_xz_final(m,,:) = n_xz;
end
end
den_level = n_xz_min : (n_xz_max-n_xz_min)/density_res : n_xz_max; %density level to draw

% A = movie_maker(X0, z0, den_level, dist, int_current_noise, N, n_xz_final); % Creating a video
%-----
%           Creating the movie
%-----

% movie2avi(A, 'density_movie.avi','compression', 'i420', 'quality', 80, 'fps', 30)

%-----
%           Plotting noise vs z data
%-----
figure(10)
plot(dist,int_current_noise(1,+)/max(int_current_noise(1,+)),'-xr'); % normalized plot band 1
% hold on
% plot(dist,int_current_noise(2,+)/max(int_current_noise(2,+)),'-x'); % normalized plot band 2
xlabel('Z distance [m]')
ylabel('Noise [Norm]')
%title('Noise Suppression ATF Rest, 1-2um')
%-----

```

```

function [x0, z0, n_xz_final] = NR_filtered_3D_slice( x, y, z, xy_res, z_res, lambdamin, lambdamax)
%-----
% Applying filtering in z axis and drawing e-density in the xz and yz planes
%-----
parnum = numel(z);
pulse_length = max(z)-min(z);
Rb = max(x);
n = parnum/pulse_length./(pi*Rb.^2);
kmin = 2*pi/lambdamax; % low kz band pass filter rest frame
kmax = 2*pi/lambdamin; % high kz band pass filter rest frame
kmax_xy = 2*pi./(n).^(-1/3);
kmin_xy = 2*pi./(2*Rb);
center_of_pulse = pulse_length/2;
%-----
ave_den = parnum / ( 2*Rb*(max(y)-min(y)) * pulse_length );
x0 = [-Rb: 2*Rb/xy_res : Rb];
% y0=[min_y:(max_y-min_y)/xy_res:max_y];
z0 = [min(z) : pulse_length/z_res : max(z)];
n_xz = zeros(length(x0), length(z0), length(z));

for u = 1:length(z)
clear n_x; clear n_z;
n_z = 2*pi^2*(kmax*sinc(1/pi*kmax*(z0-z(u))) - kmin*sinc(1/pi*kmin*(z0-z(u))));
% n_x = 1/pi*kmax_xy*sinc(1/pi*kmax_xy*(x0-x(u)));%-kmin_xy(j)*sinc(1/pi*kmin_xy(j)*(x0-x_tag_fil(u)));

n_x = 2*pi^2*(kmax_xy*sinc(1/pi*kmax_xy*(x0-x(u))) -kmin_xy*sinc(1/pi*kmin_xy*(x0-x(u)) ) );

% n_y=2*pi^2*(kmax_xy(j)*sinc(1/pi*kmax_xy(j)*(y0-y_tag_fil(u)))-kmin_xy(j)*sinc(1/pi*kmin_xy(j)*(y0-
y_tag_fil(u))));
% n_x0=2*pi^2*(kmax_xy(j)*sinc(1/pi*kmax_xy(j)*(-x_tag_fil(u)))-kmin_xy(j)*sinc(1/pi*kmin_xy(j)*(-x_tag_fil(u))));
% n_y0=2*pi^2*(kmax_xy(j)*sinc(1/pi*kmax_xy(j)*(-y_tag_fil(u)))-kmin_xy(j)*sinc(1/pi*kmin_xy(j)*(-y_tag_fil(u))));

n_xx(:,u) = n_x;
n_xz(:,u) = n_x'*n_z; %*2*n_y0;
% n_yz(:,u)=n_y'*n_z*2*n_x0;
end

n_xx1 = sum(n_xx,2);
n_xz_final = sum(n_xz,3);
% n_z_final1 = sum(n_xz_final1,1);

end

```

number of Ginzburg lengths used in the calculation, *gamma*: Lorentz factor according to the electron's energy, *regime*: whether to use the full exact solution or to use the far-field approximation (saves computation time) by choosing the appropriate Green function to be used. The outputs of the function are the complex XY electric field  $E_{xy}$ , and the absolute squared value of the complex electric field  $I_{xy}$ . If one needs to create an image based on many particles, calculation of the single particle is performed once, and the coordinates of the other particles are used for a 2D interpolation and summation of the complex results from all particles.

```

%%%%%%%%%%%%%%%%%%%%%%%%%%%%%%%%%%%%%%%%%%%%%%%%%%%%%%%%%%%%%%%%%%%%%%%%
%
% OTR
%%%%%%%%%%%%%%%%%%%%%%%%%%%%%%%%%%%%%%%%%%%%%%%%%%%%%%%%%%%%%%%%%%%%%%%%
% This function calculates OTR from a single particle in 2D
%%%%%%%%%%%%%%%%%%%%%%%%%%%%%%%%%%%%%%%%%%%%%%%%%%%%%%%%%%%%%%%%%%%%%%%%

function[E_xy,I_xy] = single_otr_xy(lambda, dist, x, y, int_res, n_ginz, gamma, regime)
% lambda- Wave length
% dist- detector location
% int_res- integration resolution
% n_ginz- number of Ginzburg lengths
% gamma- gamma factor
% regime- the approximation which will be used: 'exact', 'far'
%-----
% Constants
%-----
c=3e8;% [m/sec]
q=1.6e-19;%[C]
myu=4*pi*1e-7;%[N/A^2]
epsilon= 8.85e-12;
k=2*pi/lambda;
w=k*c;
t0 = 0;
beta=(1-(1/gamma^2))^0.5;
Lf=2*lambda*gamma^2;%[m]
%-----
% Defining current density
%-----
J_pos=@(z) -q*exp(1i*(w*t0+(k*z/beta)));
J_neg=@(z) -q*exp(1i*(w*t0-(k*z/beta)));
%-----
% Green functions to be used
%-----
R = @(Ro,z) ((dist-z).^2+Ro^2).^0.5;
r = @(Ro) (dist^2+Ro^2)^0.5;
sin_theta = @(Ro) Ro/r(Ro);
cos_theta = @(Ro) dist/r(Ro);
kz = @(Ro) k*cos_theta(Ro);

switch regime
case 'exact'
Green_Function=@(Ro,z) -(1/(4*pi))*Ro*(dist-z).*(exp(1i*k*R(Ro,z))./(R(Ro,z).^3)).*(1+(3i./(k*R(Ro,z)))-(3./((k*R(Ro,z)).^2)));
case 'far'
Green_Function=@(Ro,z) -sin_theta(Ro)*cos_theta(Ro)*exp(1i*k*(r(Ro)))/(4*pi*r(Ro)).*exp(1i*kz(Ro).*z);
end

%-----
% creating used variables
%-----
z_neg = linspace(-n_ginz*Lf,0,int_res);
%-----
% Calculation of electric field
%-----
E = @(Ro) -1i*J_pos(z_neg).*Green_Function(Ro,z_neg)*ones(length(z_neg),1)*(n_ginz*Lf/int_res);

[X,Y] = meshgrid(x,y);
Ro = sqrt(X.^2+Y.^2);

tic
E_xy=arrayfun(E,Ro); % Calculates the transverse E field in the XY mesh
toc
I_xy = abs(myu*w*E_xy).^2;

return

```

## REFERENCES

- [1] W. Schottky and Heinrich Welker. *Physics Today*, 29(6)(63), 1976.
- [2] H.A. Haus and N.H. Robinson. The minimum noise figure of microwave amplifiers. *Proc. IRE*, 43(981), 1955.
- [3] P. Emma et al. First lasing and operation of an angstrom-wavelength free-electron laser. *Nature Photonics*, 4:641–647, 2010.
- [4] R. Akre et al. Commissioning the linac coherent light source injector. *Phys. Rev. ST Accel. Beams*, 11:030703, 2008.
- [5] D. Ratner, A. Chao, and Z. Huang. Three-dimensional analysis of longitudinal space charge microbunching starting from shot noise. In *Proceedings of the 2008 Free Electron Laser Conference*, 2008.
- [6] E. Dyunin and A. Gover. The general velocity and current modulation linear transfer matrix of fel and control over sase power in the collective regime. *Nuclear Instruments and Methods in Physics Research Section A*, 593:49–52, 2008.
- [7] A. Gover and E. Dyunin. Collective-interaction control and reduction of optical frequency shot noise in charged-particle beams. *Phys. Rev. Lett.*, 102(15):154801, Apr 2009.
- [8] A. H. Lumpkin. First observations of cotr due to a microbunched beam in the vuv at 157mm. *Nuclear Instruments and Methods in Physics Research A*, 528:194–198, 2004.
- [9] A. Nause, E. Dyunin, and A. Gover. Optical frequency shot-noise suppression in electron beams. *J. of Applied Physics*, 107:103101, 2010.
- [10] A. Gover, A. Nause, E. Dyunin, and Fedurin M. Beating the shot-noise limit. *Nature Physics*, 2012.
- [11] Daniel Ratner and Gennady Stupakov. Observation of shot noise suppression at optical wavelengths in a relativistic electron beam. *Phys. Rev. Lett.*, 109:034801, Jul 2012.
- [12] Daniel Ratner, Zhirong Huang, and Gennady Stupakov. Analysis of shot noise suppression for electron beams. *Phys. Rev. ST Accel. Beams*, 14(6):060710, Jun 2011.

- [13] A. Gover. Collective microdynamics and noise suppression in dispersive electron beam transport. *Physics of Plasmas*, 18(123102), 2011.
- [14] R. H. Dicke. Coherence in spontaneous radiation processes. *Phys. Rev.*, 93:99–110, Jan 1954.
- [15] James M. Glowina, J. Cryan, J. Andreasson, A. Belkacem, N. Berrah, C. I. Blaga, C. Bostedt, J. Bozek, L. F. DiMauro, L. Fang, J. Frisch, O. Gessner, M. Gühr, J. Hajdu, M. P. Hertlein, M. Hoener, G. Huang, O. Kornilov, J. P. Marangos, A. M. March, B. K. McFarland, H. Merdji, V. S. Petrovic, C. Raman, D. Ray, D. A. Reis, M. Trigo, J. L. White, W. White, R. Wilcox, L. Young, R. N. Coffee, and P. H. Bucksbaum. Time-resolved pump-probe experiments at the lcls. *Opt. Express*, 18(17):17620–17630, Aug 2010.
- [16] A. Nause, E. Dyunin, and A. Gover. Electron beam shot noise suppression by collective coulomb interaction. *Proceedings of the 2009 Free-Electron Laser Conference (Liverpool, UK)*, 2009.
- [17] R. C. Davidson. *Methods in Nonlinear Plasma Theory*. Academic, New York, 1972.
- [18] J. B. Rosenzweig. *Fundamentals of beam physics*. Oxford University Press, 2003.
- [19] P. Musumeci, R. K. Li, and A. Marinelli. Nonlinear longitudinal space charge oscillations in relativistic electron beams. *Phys. Rev. Lett.*, 106:184801, May 2011.
- [20] L. J. Chu. A kinetic power theorem. In *IRE-PGED Electron Tube Research Conference*, 1951.
- [21] E. Dyunin. *Noise Propagation on Relativistic E-Beam and Coherence Limits of FELs*. PhD thesis, Tel Aviv University, 2013.
- [22] G.M. Brunch and T.G. Mihran. Plasma frequency reduction factors in electron beams. *IRE Transactions on Electron Device*, 2:3, 1955.
- [23] M. Venturini. Models of longitudinal space-charge impedance for microbunching instability. *Phys. Rev. ST Accel. Beams*, 11:034401, 2008.
- [24] A. Marinelli and J.B. Rosenzweig. Microscopic kinetic analysis of space-charge induced optical microbunching in a relativistic electron beam. *Phys. Rev. ST Accel. Beams*, 13:110703, 2010.

- [25] R. A. Bosch, K. J. Kleman, and J. Wu. Modeling two-stage bunch compression with wakefields: Macroscopic properties and microbunching instability. *Phys. Rev. ST Accel. Beams*, 11:090702, Sep 2008.
- [26] Z. Huang et al. Suppression of microbunching instability in the linac coherent light source. *Phys. Rev. ST Accel. Beams*, 7(074401), 2004.
- [27] M. Reiser. *Theory and Design of Charged Particle Beams*. Wiley Series in Beam Physics and Accelerator Technology, 1994.
- [28] S. Heifets and G. Stupakov. Beam instability and microbunching due to coherent synchrotron radiation. *Phys. Rev. ST-AB*, 5:054402, 2002.
- [29] A. Marinelli. Generation of coherent broadband photon pulses with a cascaded longitudinal space-charge amplifier. *Phys. Rev. Lett*, 110(264802), 2013.
- [30] D. Ratner, Z. Huang, and G. Stupakov. Analysis of shot noise suppression for electron beams. *Phys. Rev. ST Accel. Beams*, 14:060710, 2011.
- [31] <http://www.pulsar.nl>.
- [32] I. Reidler, Y. Aviad, M. Rosenbluh, and I. Kanter. Ultrahigh-speed random number generation based on a chaotic semiconductor laser. *Phys. Rev. Lett.*, 103:024102, Jul 2009.
- [33] David Goodman Roy D. Yates. *Probability and Stochastic Processes: A Friendly Introduction for Electrical and Computer Engineers*.
- [34] V.L. Ginzburg and I.M. Frank. Transition radiation. *Zh. Eksp. Teor. Fiz.*, 16(1):15–22, 1946.
- [35] N.A. Vinokurov. The generator of high-power short thz pulses. In *Proceedings of FEL2012, Nara, Japan*, 2012.
- [36] M. Ter Mikaelian. *High Energy Electromagnetic Processes in Condensed Media*. Wiley, 1975.
- [37] C. A. Brau. *Modern Problems in Classical Electrodynamics*. Oxford University Press, New York, 2004.
- [38] J. W. Goodman. *Introduction to Fourier Optics*. Roberts and Company Publishers, 2005.

- [39] H. Loos and et al. Observation of coherent optical transition radiation in the lcls linac. *Proceedings of the 2008 Free-Electron Laser Conference (Gyeongju, Korea)*, page p. 619, August 2008.
- [40] A. G. Shkvarunets and R. B. Fiorito. Vector electromagnetic theory of transition and diffraction radiation with application to the measurement of longitudinal bunch size. *Physical Review Special Topics*, 11(012801), 2008.
- [41] Gianluca Geloni, Evgeni Saldin, Evgeni Schneidmiller, and Mikhail Yurkov. Fourier treatment of near-field synchrotron radiation theory. *Optics Communications*, 276(1):167 – 179, 2007.
- [42] Robert E. Collin. *Field Theory of Guided Waves*. IEEE Press Series on Electromagnetic Wave Theory, 1990.
- [43] Gianluca Geloni, Petr Ilinski, Evgeni Saldin, Evgeni Schneidmiller, and Mikhail Yurkov. Method for the determination of the three-dimensional structure of ultrashort relativistic electron bunches. Deutsches Elektronen-Synchrotron DESY, Hamburg, May 2009.
- [44] E. Schneidmiller E. Saldin and M. Yurkov. A simple method for the determination of the structure of ultrashort relativistic electron bunches. *Nucl. Instrum. Meth. A*, 539:499, 2005.
- [45] V. L. Ginzburg. Transition radiation and transition scattering. *Physica Scripta Volume T*, 2:182–+, June 1982.
- [46] L. Wartski. *J. Appl. Phys.*, 48(3646), 1975.

**חציית מחסום ה"רעש ברד":  
הנחתת רעש ע"י אינטראקציות קולקטיביות בתחום  
האופטי בקרני חלקיקים טעונים יחסותיות**

חיבור לשם קבלת התואר "דוקטור לפילוסופיה"

על ידי

**אריאל נעוס**

הוגש לסנאט של אוניברסיטת תל אביב

**פרופ. אברהם גובר**

2014

## תקציר העבודה

# חציית מחסום ה"רעש ברד": הנחתת רעש ע"י אינטראקציות קולקטיביות בתחום האופטי בקרני חלקיקים טעונים יחסותיות

על ידי

## אריאל נעוס

הנושא העיקרי בעבודת מחקר זו הוא השליטה בתהליך הבסיסי של מיקרו-דינמיקה וקרינה מקרני חלקיקים טעונים, תחת השפעת כוחות "מטען מרחבי" אורכיים. נושאים אלו הינם בעלי עניין מדעי בסיסי כשלעצמם, אך גם מאוד רלוונטיים למחקר של "לייזרים מאלקטרוניים חופשיים". האפשרות לשלוט ברעש הזרם של קרן חלקיקים בתדר האופטי באמצעות אינטראקציות קולקטיביות אורכיות, ניתנת להבנה וניתוח באמצעות מודל חד-מימדי מורחב (מודל לנגמור רוחבי בודד). מודל זה מנבא אפשרות להפחתת רעש הזרם בקרן החלקיקים גם אל מתחת לגבול הקלאסי של "רעש ברד". על מנת לוודא כי אפקט זה מתרחש גם תחת תנאים מציאותיים של קרן חלקיקים במעבדה, ביצעתי סימולציות נומריות תלת-מימדיות בתוכנת GPT (General Particle Tracer). סימולציות אלו כוללות אינטראקציות קולומב בין-חלקיקיות, ולכן מתארות בצורה מלאה אפקטים קולקטיביים של המיקרו-דינמיקה התלת מימדית. התוצאות הנומריות מראות כי רעש הזרם המינימלי מתקבל לאחר סחיפה למרחק של רבע אורך-גל תדר הפלסמה, עם מקדם-הפחתה לקרן ברוחב סופי, כמתקבל מהמודל האנליטי.

בהתבסס על התחזיות התיאורטיות ביצעתי ניסויים במעבדות מאיצים בנסיון להדגים נסיונית, בפעם הראשונה אי פעם, הפחתת רעש זרם בתדר אופטי. אופן מדידת רעש הזרם בניסוי התבסס על מדידת קרינה אופטית מסוג OTR (Optical Transition Radiation) (קרינת מעבר בתדר אופטי) מקרן האלקטרוניים. על מנת לנתח ולהבין את תוצאות הקרינה הנמדדת, פיתחנו שיטה חדשה לחישוב השדות המרוכבים של קרינת המעבר מאלקטרוניים, המתבססת על פתרון משוואת גרין הדיאדית. מודל זה הינו מדויק בכל איזורי הדיפרקציה (קרוב ורחוק).

ביצעתי שני ניסויים בLCLS (אשר באוניברסיטת סטנפורד) ובATF (במעבדת המחקר BNL של ברוקהייבן, ניו-יורק) אשר מדגימים בפעם הראשונה הפחתת רעש זרם בתדר אופטי מתחת לגבול הקלאסי של "רעש ברד". אפקט זה עשוי להיות שימושי לשליטה בחוסר יציבות הנובע ממיקרו-התקבצויות, וכן להגברת הקוהרנטיות בלייזרים מאלקטרוניים חופשיים.

**עבודה זו נעשתה תחת הדרכתו של**

**פרופ. אברהם גובר**

**2014**